UNIVERSITY OF CALIFORNIA
RIVERSIDE

Using Solid-State Nuclear Magnetic Resonance to Relate Chemical Structure With the Function of Materials

A Dissertation submitted in partial satisfaction
of the requirements for the degree of

Doctor of Philosophy

in

Chemistry

by

Kevin R. Chalek

June 2021

Dissertation Committee:

Dr. Leonard J. Mueller, Chairperson
Dr. Ryan R. Julian
Dr. Wenwan Zhong

The Dissertation of Kevin R. Chalek is approved

_____

_____

_____

Committee Chairperson

University of California, Riverside

Acknowledgements

I would like to acknowledge my research advisor Leonard Mueller for his well of knowledge, his kindness, and his unbelievable patience. My graduate school experience would truly not have been nearly as rewarding without him guiding me over the past 5 years. Thank you.

To my former lab mates Robert Young, Bethany Caulkins, and Ryan Kudla for welcoming me and helping me get started, and my current lab mates Viktoriia Liu, Varun Sakhrani, Manpreet Kaler, Jacob Holmes, Rittik Ghosh, Dave Amarasinghe, and Christopher Williams for their friendship, intelligence, and hours of comedy.

To my collaborators Chris Bardeen, Fei Tong, Claire Dong, Francisco Zaera, Junghyun Hong, Jennifer Lu, Wenxin Fu, Richard Hooley, Adam Gill, and Bryce da Camara for their expertise in their respective fields and diligent e-mail responding.

To Jerry Hu and Jaya Nolt at the Materials Research Lab at UCSB and Frederic Mentink-Vigier and Faith Scott at the National High Magnetic Field Lab in Tallahassee for teaching me so much about DNP experiments and the future of NMR.

To my grandparents, parents, sister, and girlfriend: I cannot wait to share this achievement with you.

The work in this dissertation comes entirely or in part from the following publications:

Kevin R. Chalek, Xinning Dong, Fei Tong, Ryan A. Kudla, Lingyan Zhu, Adam D. Gill, Wenwen Xu, Chen Yang, Joshua D. Hartman, Avicler Magalhães, Rabih O. Al-Kaysi, Ryan C. Hayward, Richard J. Hooley, Gregory J. O. Beran, Christopher J. Bardeen and Leonard J. Mueller. Bridging photochemistry and photomechanics with NMR crystallography: the molecular basis for the macroscopic expansion of an anthracene ester nanorod. *Chem. Sci.*, 2021, 12, 453-463.

Bryce da Camara, Philip C. Dietz, **Kevin R. Chalek**, Leonard J. Mueller and Richard J. Hooley. Selective, cofactor-mediated catalytic oxidation of alkanethiols in a self-assembled cage host. *Chem. Commun.*, 2020, 56, 14263-14266.

ABSTRACT OF THE DISSERTATION

Using Solid-State Nuclear Magnetic Resonance to Relate Chemical Structure With the Function of Materials

by

Kevin R. Chalek

Doctor of Philosophy, Graduate Program in Chemistry
University of California, Riverside, June 2021
Dr. Leonard J. Mueller, Chairperson

Solid-state Nuclear Magnetic Resonance (ssNMR) combined with x-ray diffraction and first-principles computational chemistry, in a method called NMR-assisted crystallography, is used to determine the chemical structure of a variety of materials. 9-ter-butyl-anthracene ester (9TBAE) in molecular crystal nanorods can undergo a photodimerization that causes expansions of up to 15%. The expansion is a result of the formation of a metastable crystalline intermediate, the solid-state reacted dimer (SSRD). A molecular level understanding of 9TBAE using NMR-assisted crystallography is required to fully explain this expansion.

ssNMR experiments on aligned nanorods and powder samples of 9TBAE allows for the observation that the nanorod expansion is a result of a rotation of the unit cells from monomer to SSRD. Additionally, the magnitude of expansion or contraction during the reaction can be predicted if the initial orientation of the unit cell with respect to the nanorod axis is known. These results are confirmed by diffraction and computational methods.

ssNMR is used to reveal the structure of a few different materials in this work. Silica surface sites, where a lack of sensitivity in NMR makes observation of non-covalent bonding difficult, are observed using Dynamic Nuclear Polarization – Surface Enhanced NMR Spectroscopy (DNP-SENS). Thermally sensitive monomers can also be characterized and the negative thermal expansion they undergo can be described on a molecular level.

Finally, a statistical method is described that can be used to discriminate between UV-Vis data of 1:1 and 1:2 host-guest complexes. Statistical methods are also used to compare different non-uniform sampling (NUS) methods in NMR.

Table of Contents

List of Figures

List of Tables

Chapter 1 – Introduction and Background to Nuclear Magnetic Resonance

1.1 Overview

The principles of Nuclear Magnetic Resonance (NMR) have been studied and written about extensively in several essential texts.[1-3] Nuclei in a sample are shielded by different amounts based on their local structure, resulting in different NMR frequencies. These frequencies are then used to reveal the chemical structure of the sample.[4] Other basic concepts will be covered below in greater detail to introduce the concepts and theories that will be necessary for understanding the following work.

1.2 NMR Basics

The intrinsic angular momentum of a particle is its spin (I). The spin of a nucleus is determined by the number of protons and neutrons it contains and can have integer or half-integer values. A nucleus with a non-zero spin is considered NMR active and will result in (2I+1) spin states. Two of the most studied NMR active nuclei, ^{1}H and ^{13}C, are both spin-1/2 and form two spin states (α and β) of different energies when placed in an external magnetic field B_0 (figure 1.1). This Zeeman splitting results in an energy difference of ΔE (equation 1.1) which is determined by the gyromagnetic ratio (γ) of the

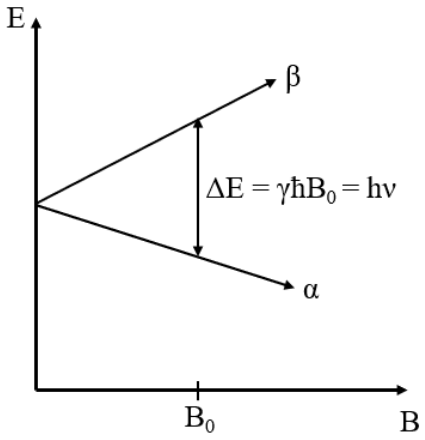

Figure 1.1: Zeeman splitting of a spin-1/2 nucleus in a magnetic field of strength B_0

individual nucleus, the reduced Plank's constant (ħ), and the strength of the external magnetic field (equation 1.1).

$$\Delta E = \gamma \hbar B_0 = h\nu \quad \text{(Equation 1.1)}$$

For a quantum mechanical treatment of this system, we refer to the Hamiltonian in equation 1.2 where $\hat{I}_Z$ is the angular momentum operator. The angular momentum operator operates on the eigenfunctions α and β in equations 1.3 and 1.4. The Hamiltonian operates on α and β in equations 1.5 and 1.6. Finally, the energy difference found in equation 1.7 is the same as equation 1.1.

$$\hat{H}_0 = -\gamma B_0 \hat{I}_Z \quad \text{(Equation 1.2)}$$

$$\hat{I}_Z \alpha = \frac{\hbar}{2}\alpha \qquad \hat{I}_Z \beta = -\frac{\hbar}{2}\beta \quad \text{(Equations 1.3 and 1.4)}$$

$$\hat{H}_0 \alpha = -\frac{1}{2}\gamma \hbar B_0 = E(\alpha) \quad \hat{H}_0 \beta = \frac{1}{2}\gamma \hbar B_0 = E(\beta) \quad \text{(Equations 1.5 and 1.6)}$$

$$\Delta E = E(\beta) - E(\alpha) = \gamma \hbar B_0 \quad \text{(Equation 1.7)}$$

This difference in energy between the two spin states effects the sensitivity of the experiment because the population difference between the two states depends on their difference in energy according to equation 1.8, where ΔP is the population difference, k_B is the Bolztmann constant, and T is the temperature of the sample.

$$\Delta P = \frac{-\Delta E}{exp^{K_\beta * T}} \quad \text{(Equation 1.8)}$$

All the magnetic moments of the specific nuclei being observed contribute to the bulk magnetization. Bulk magnetization of spins in the z-direction corresponds to the population difference between the two spin states. Spins have a preference to be aligned with the external magnetic field B_0 so the vector sum over all magnetic moments is aligned

along the z-axis in the magnet. The coil in the actual instrument used to measure this bulk magnetization, however, is in the xy-plane. Radiofrequency pulses of a broad frequency are applied to the nuclei, the magnetization that is resonant with those pulses are rotated into the xy-plane, and the bulk magnetization can be observed.

The strength of the magnetic field, identity of the nucleus, and temperature determine the sensitivity of the NMR experiment being conducted. Additionally, there is a lack of abundance of certain spin-1/2 nuclei of interest. ^{13}C is only 1.11% abundant, ^{15}N 0.36% abundant, and ^{29}Si 4.67% abundant. The lower the abundance, the less the nuclei can contribute to the bulk magnetization. However, it is worth mentioning that ^{1}H is 99.9% abundant and has the highest gyromagnetic ratio of any nuclei.[3] All of this leaves NMR as a relatively insensitive technique.

NMR signal is digitized as the Free Induction Decay (FID) in the time domain, oscillating according to the resonant frequencies of the nuclei of interest and decaying according to Transverse Relaxation (T_2) as the bulk magnetization leaves the xy-plane.[3,5-8] The Fourier Transform (equation 1.9) is applied to convert the signal into the frequency domain.[9] This process is shown visually in figure 1.2 for a single resonant frequency centered at 200 Hz.

$$F(\nu) = \int_{-\infty}^{\infty} f(t) e^{-i2\pi\nu t}\, dt \qquad \text{(Equation 1.9)}$$

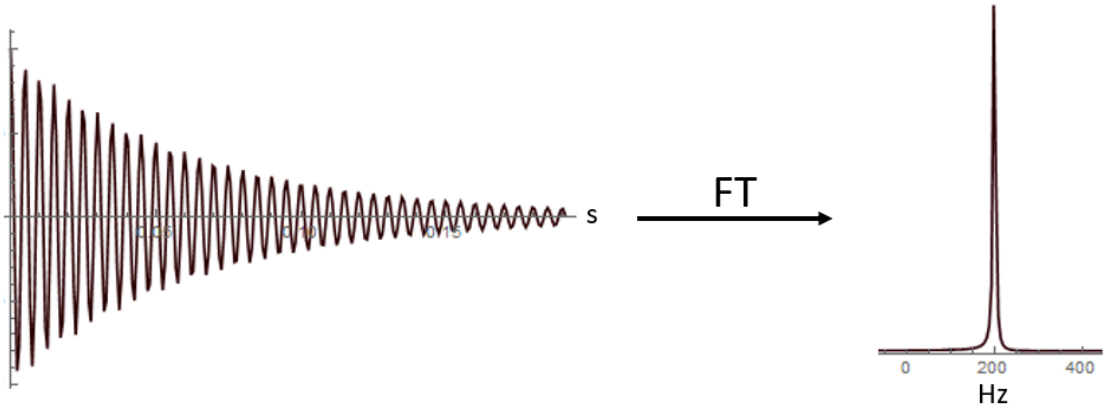

Figure 1.2: The Fourier Transform for one resonant frequency at 200 Hz.

Observable NMR signal is a measure of the electron shielding σ around individual nuclei and then reported as chemical shift (equation 1.10). Chemical shift δ is the shielding of the nuclei of interest in a sample compared against a reference compound and is reported in ppm (equation 1.11).

$$B_Z = (1 - \sigma)B_0 \qquad \text{(Equation 1.10)}$$

$$\delta = \left(\sigma_{ref} - \sigma_{interest}\right) * 10^6 \qquad \text{(Equation 1.11)}$$

A typical NMR spectrum in the frequency domain will have multiple peaks corresponding to the resonances generated by the shielding surrounding each individual atom of the same type of nucleus in a molecule. Chemical shifts contain useful information about local structure and are often the basis of more complicated NMR experiments.

1.3 Solid-State NMR (ssNMR)

In an NMR experiment where a solid powder is being observed, all the individual orientations of the crystallite will be different with respect to the magnetic field. This results in a powder pattern, where each resulting peak overlaps slightly to form a very broad

peak, making determination of the chemical shift difficult (figure 1.3, left). This line broadening is referred to as the Chemical Shift Anisotropy (CSA). If the solid powder were dissolved in a solution, the sample's motion increases dramatically, averaging out all the differences in the possible states of the bulk sample, resulting in sharp isotropic peaks (figure 1.3, right).

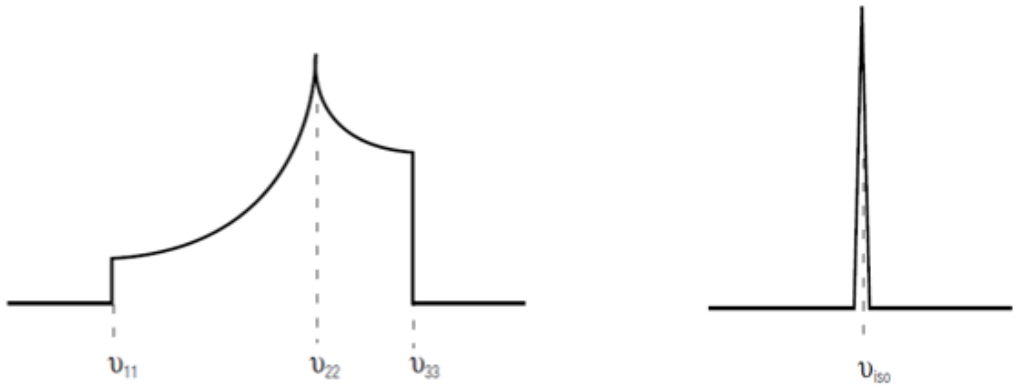

Figure 1.3: Comparison of CSA pattern characteristic of static solid-state NMR and the sharp isotropic signal characteristic of solution-state NMR. Adapted from Duer.[1]

The CSA powder pattern can be described in terms of the principal values of the CSA tensor. Tensors can be defined by a few different conventions, of which we will use the IUPAC convention with three principle components υ_{11}, υ_{22}, υ_{33}, where $\upsilon_{11} \geq \upsilon_{22} \geq \upsilon_{33}$ and the average of the principle components is the isotropic chemical shift.

However, if the solid powder sample is placed at an angle of 54.8° relative to the applied magnetic field and spun (figure 1.4), a process called Magic Angle Spinning (MAS), then the bulky anisotropies disappear, and the center isotropic peak corresponds to the chemical shift.[10,11] There are also spinning sidebands spaced at the spinning frequency from the center peak which get smaller and further away as the spinning speed increases (figure 1.5). The benefit of ssNMR over solution-state NMR is the information contained within these anisotropies beyond the chemical shift. While being able to determine the structure of a solid without the interference of a solvent, these anisotropic interactions include through-space dipolar interactions that can be used to ascertain structures more accurately.[4,12]

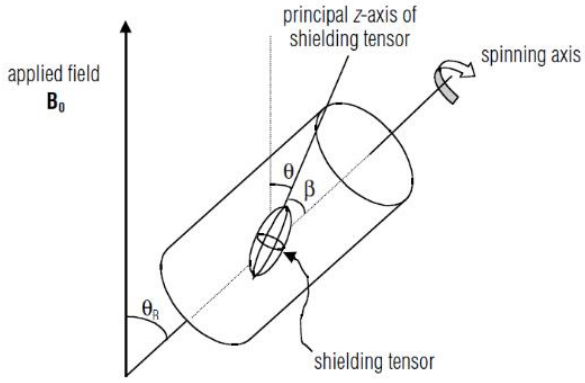

Figure 1.4: ssNMR sample in a rotor spinning at the magic angle. Reprinted from Duer.[1]

The dipolar interaction in the solid-state can also be utilized by performing cross

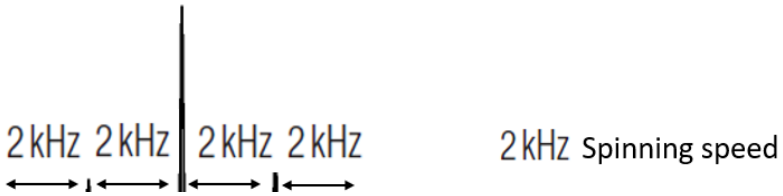

Figure 1.5: Spinning sidebands at 2 kHz away from the center peak. Adapted from Duer.[1]

polarization (CP).[13,14] CP and MAS are combined into CPMAS, a technique which is very common in ssNMR experiments, allowing for increased sensitivity.[11] The pulse sequence (figure 1.6) begins with a 90° pulse to bring ^{1}H magnetization into the xy- plane. This

magnetization is transferred to a different nucleus of interest by dipolar couplings and matching resonant frequency through a spin lock. Magnetization can only be transferred using CP through nuclei that have a dipolar coupling, meaning they are close together in space. Low abundance nuclei mentioned above, such as ^{13}C, ^{15}N, and ^{29}Si, can have their signal enhanced, in theory, by the ratio of gyromagnetic ratios between ^{1}H and the nuclei of interest.

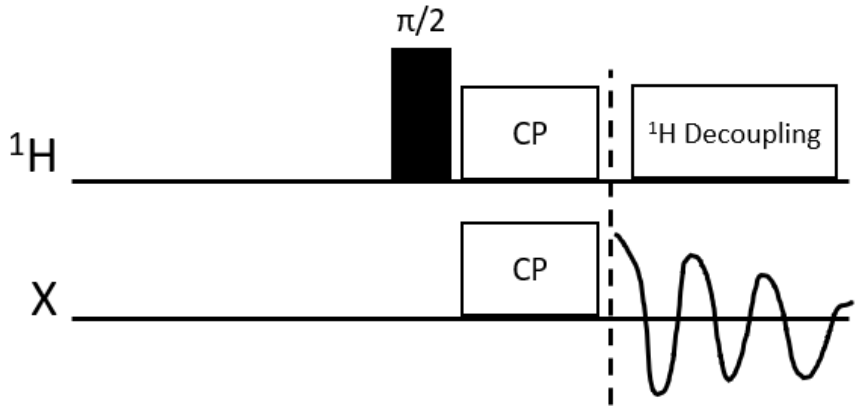

Figure 1.6: The pulse sequence of the cross polarization experiment.

1.4 Conclusion

This brief introduction to common NMR topcis presents a number of ideas that will be referenced in the following chapters, specifically the technique of CPMAS and the associated theory behind it. Subsequent chapters will show established ssNMR methods in determining chemical structure and relating it to function, with more powerful techniques being introduced.

1.5 References

(1) Duer, M. J.: *Solid-State NMR Spectroscopy: Principles and Applications*; Blackwell Science: Malden, MA, 2002.

(2) Keeler, J.: *Understanding NMR Spectroscopy*; 2nd ed.; John Wiley and Sons: Chichester, U.K., 2010.

(3) Levitt, M. H.: *Spin Dynamics: Basics of Nuclear Magnetic Resonance*; 2nd ed.; John Wiley & Sons: Chichester, England ; Hoboken, NJ, 2008.

(4) Facelli, J. C. Chemical shift tensors: Theory and application to molecular structural problems. *Progress in nuclear magnetic resonance spectroscopy* **2011**, *58*, 176.

(5) Bloembergen, N.; Purcell, E. M.; Pound, R. V. Relaxation Effects in Nuclear Magnetic Resonance Absorption. *Physical Review* **1948**, *73*, 679-712.

(6) Bloch, F. Nuclear Induction. *Physical Review* **1946**, *70*, 460-474.

(7) Meiboom, S.; Gill, D. Modified Spin-Echo Method for Measuring Nuclear Relaxation Times. *Review of Scientific Instruments* **1958**, *29*, 688-691.

(8) Hahn, E. L. Spin Echoes. *Physical Review* **1950**, *80*, 580-594.

(9) Ernst, R. R.; Anderson, W. A. Application of Fourier Transform Spectroscopy to Magnetic Resonance. *Review of Scientific Instruments* **1966**, *37*, 93-102.

(10) Andrew, E.; Bradbury, A. R. G. Eades. *Nature (London)* **1958**, *182*, 1659.

(11) Schaefer, J.; Stejskal, E. O. Carbon-13 nuclear magnetic resonance of polymers spinning at the magic angle. *Journal of the American Chemical Society* **1976**, *98*, 1031-1032.

(12) Herzfeld, J.; Berger, A. E. Sideband intensities in NMR spectra of samples spinning at the magic angle. *The Journal of Chemical Physics* **1980**, *73*, 6021-6030.

(13) Pines, A.; Gibby, M. G.; Waugh, J. S. Proton-Enhanced Nuclear Induction Spectroscopy. A Method for High Resolution NMR of Dilute Spins in Solids. *The Journal of Chemical Physics* **1972**, *56*, 1776-1777.

(14) Pines, A.; Gibby, M. G.; Waugh, J. S. Proton-enhanced NMR of dilute spins in solids. *The Journal of Chemical Physics* **1973**, *59*, 569-590.

(15) Rossini, A. J.; Zagdoun, A.; Lelli, M.; Lesage, A.; Copéret, C.; Emsley, L. Dynamic Nuclear Polarization Surface Enhanced NMR Spectroscopy. *Accounts of Chemical Research* **2013**, *46*, 1942-1951.

Chapter 2 – Photomechanical Expansion of 9TBAE Nanorods Using NMR-assisted Crystallography

2.1 Introduction

Molecular crystals have been found to have a variety of effects when exposed to light. Among these photomechanical effects are bending, twisting, and rotations[1-8], which are generally a result of an incomplete reaction of the bulk material: the shape change is a result of the difference in structure between reactant and product. Photomechanical effects can also be obtained by a single-crystal-to-single-crystal transformation[9-13], where molecules within the crystal lattice shift and create large-scale changes in the shape of the crystal. This transformation is worth studying because it can generate work via expansion of the crystal caused by exposure to light; essentially photons are being converted into mechanical work.

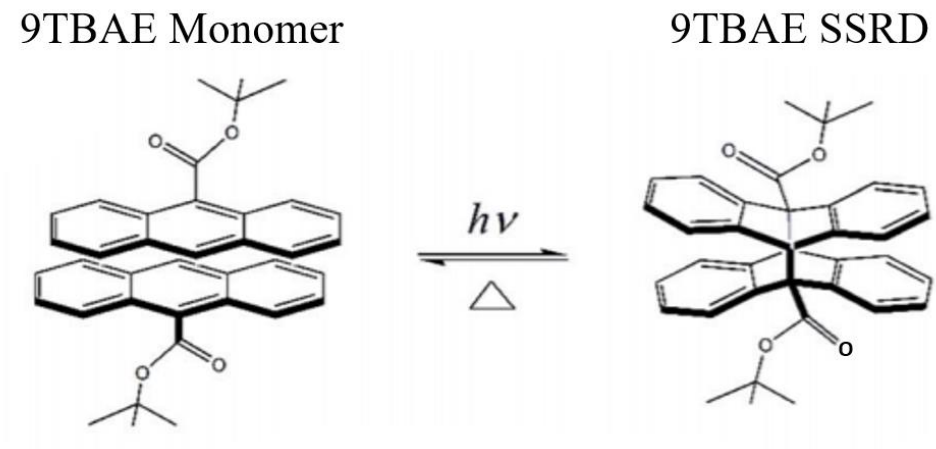

Figure 2.1: The photodimerization reaction of 9TBAE from the monomer to SSRD.

9-tert-butyl-anthracene ester (9TBAE) has been studied as an example of a crystal-to-crystal reaction resulting in expansion along its rod axis of about 8%. 9TBAE undergoes

a [4 + 4] photodimerization from a monomer to a metastable crystalline intermediate, the solid-state reacted dimer (SSRD), as depicted in figure 2.1. While the outcome of the reaction is known, the mechanism of the expansion requires further study. The unit cell volume and knowledge of the crystal structures produced predictions that 9TBAE nanorods should shrink by 1.2% when irradiated instead of expanding as observed previously.[14,15]

Single crystals of the bulk material of 9TBAE shatter when irradiated due to the internal strain of the expansion. Therefore, it is necessary to focus on smaller nanorod single crystals and powder samples to monitor the reaction. This justifies the use of ssNMR as ssNMR has been previously used to study photomechanical transformations and single-crystal-to-single-crystal reactions.[16,17] ssNMR is combined with two other structural determination methods, X-ray diffraction and first-principles computational chemistry, in a method called NMR-assisted crystallography.[18-21] These methods combined are used to develop a detailed model of the photomechanical reaction to accurately predict the size and mechanism of the expansion of the 9TBAE nanorod.

2.2 Experimental Methods

Since single crystals of bulk 9TBAE shatter when irradiated, many similarly oriented nanorods are required to perform the expansion. A single axis of alignment of many nanorods will also lead to higher resolution. Previous studies using powder X-ray diffraction, ssNMR, and SEM images confirm that the 9TBAE photodimerization can occur in anode aluminum oxide (AAO) templates so nearly all the nanorods expand in the same direction in the pores of the template. 9TBAE nanorods are grown in an AAO

template as previously described.[15] NMR studies can also be conducted on the single crystal monomer to use as a reference for the orientation of the nanorods in the magnetic field.

9TBAE nanorod experiments were conducted at 9.4 T (400.37 MHz ^{1}H and 100.68 MHz ^{13}C) on a Bruker AVANCE III spectrometer equipped with a homebuilt double resonance solid-state NMR probe fitted with a static flat coil. The bulk ensemble of uniformly oriented single crystals of 9TBAE grown on the AAO template were placed in the flat coil NMR probe with their rod axes aligned with the magnetic field and the template perpendicular to the field (figure 2.2). For single crystal experiments, the single crystal was placed inside the coil. The coil was wound 4 turns from 2 mm wide copper flat wire with dimensions of 14 mm x 14mm x 3mm. CP was implanted using a spin lock field of 25 kHz on ^{1}H and a ramped field of 21-29 kHz on ^{13}C with a 2 ms contact time. The probe was shimmed on a static sample of adamantane powder and referenced indirectly to neat TMS via adamantane with the downfield-shifted peak set to 38.48 ppm.[22]

In order to increase sensitivity, two selective ^{13}C labels of 9TBAE powder were prepared so the 1.11% natural abundance of ^{13}C could be increased to nearly 100%. The first was a ^{13}C labeled on the t-butyl groups (t-bu labeled) and the second on the carbonyl groups (carbonyl labeled). 10% ^{13}C labels were also prepared for the t-bu labeled 9TBAE.

Figure 2.2: Flat coil NMR probe and a close-up of the AAO template being inserted into the flat coil.

First-principles calculations can be used to generate structures and calculate the corresponding chemical shifts. These can then be compared to experimentally obtained isotropic chemical shifts and the useful chemical shift anisotropies uniquely found in ssNMR experiments. First-principles solid-state structures and chemical shifts were calculated first using the *Quantum Espresso* (QE) software package[23] and chemical shift calculations were done using Gaussian09 at the PBE0/6-311+G(2d,p) level[24-26]. Benchmarking studies have shown the agreement between experimental and computationally predicted chemical shifts to be within root-mean-square-errors of 1.4 ppm

for isotropic shifts, 3.2 ppm for aliphatic and aromatic shift tensor components, and 9.2 ppm for tensor components of sp^2 carbons directly bonded to oxygen and nitrogen atoms.[27]

The crystal structures of the monomer and SSRD have been determined previously and the experimentally measured isotropic chemical shifts in the monomer and SSRD and the chemical shift tensors in the SSRD showed good agreement with the computationally predicted shifts.[14] Select tensor components of the 9TBAE monomer must be measured and compared similarly to the first-principles calculated values.

Chemical shift tensors were measured experimentally using a combination of the TOSS-t_1-deTOSS experiment (figure 2.3) developed by Kolbert and Griffin[28] and the extended CSA amplification (xCSA) experiment (figure 2.4) developed by Hung and Gan.[29] Both experiments are 2-Dimensional where the sideband-free isotropic chemical shifts appear on one axis and the associated anisotropies appear on the other. The TOSS-t_1-deTOSS experiment is used when the anisotropies are 2-3 times greater than the MAS rate and the xCSA experiment is used for anisotropies comparable to or smaller than the MAS rate. Both sequences were modified as previously described.[14]

TOSS-t_1-deTOSS experiments were performed at 14.1 T (600.01 MHz ^{1}H and 150.87 MHz ^{13}C) on a Bruker Avance I spectrometer equipped with a 4 mm double resonance MAS probe with samples spinning at 2 kHz. CP was implemented using spin lock fields of 38 kHz on ^{13}C and a ramped field of 36-40 kHz on ^{1}H with a 2 ms contact time. Other RF powers were 83 kHz on ^{1}H for excitation and decoupling and 50 kHz on ^{13}C for π and $\pi/2$ pulses.

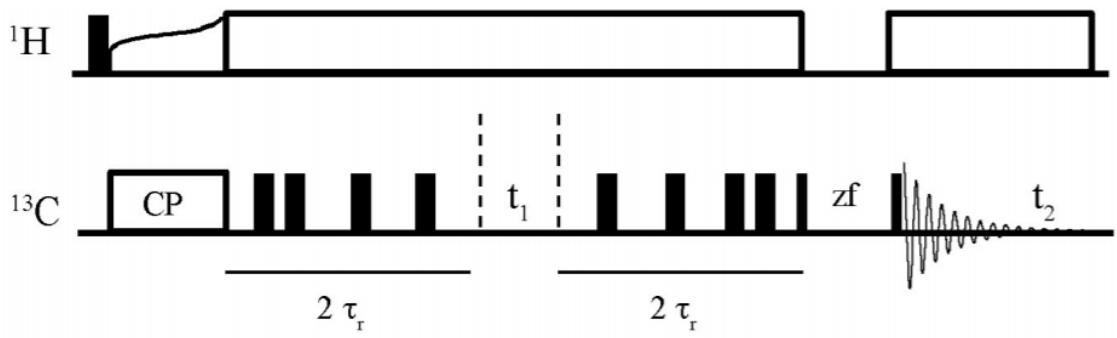

Figure 2.3: The modified TOSS-t_1-deTOSS pulse sequence.[14,28]

xCSA experiments were performed at 9.4 T (400.37 MHz ^{1}H and 100.68 MHz ^{13}C) on a Bruker AVANCE III spectrometer equipped with a 4 mm double resonance MAS probe with samples spinning at 3.125 kHz. CP spin lock fields were 41 kHz on ^{13}C and linearly ramped on ^{1}H from 36-42 kHz with a 2 ms contact time. Other RF powers were 83 kHz on ^{1}H for excitation and decoupling and 50 kHz on ^{13}C for π and $\pi/2$ pulses. ^{13}C chemical shifts were referenced indirectly to neat TMS via an external solid-state sample of adamantane with the downfield-shifted peak set to 38.48 ppm.[22] Tensor components were determined by a fit of the sideband instensities using Herzfeld-Berger analysis[30] within Bruker BioSpin's *Topspin 3.0* processing software, which relates the intensities of

the spinning sidebands to the CSA tensor components. The isotropic center band and sideband traces were summed before Herzfeld-Berger analysis for the xCSA experiments.

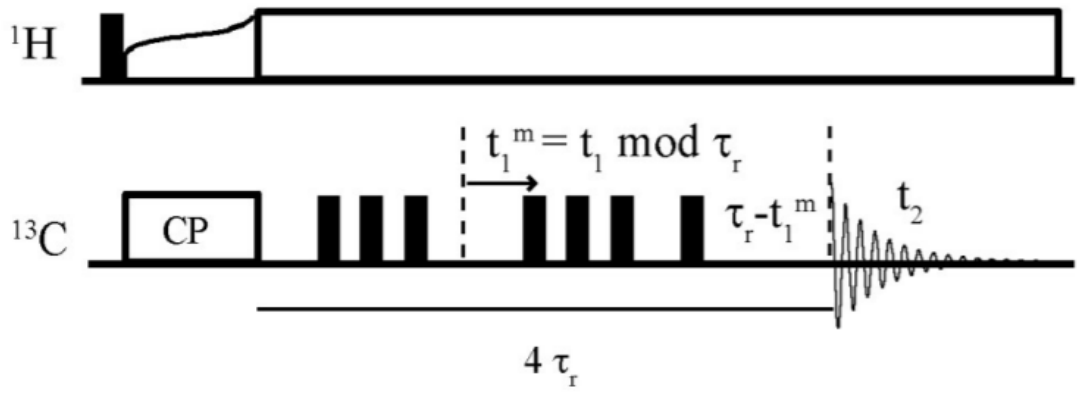

Figure 2.4: The xCSA pulse sequence[14,29]

The chemical shifts and dipolar tensors of 9TBAE can be used to obtain the absolute orientation of a 9TBAE crystal with respect to the magnetic field using TensorView in Mathematica.[31,32] Since the nanorods in the AAO template are aligned in one direction, we can also match the chemical shifts in that direction with computationally obtained chemical shifts. As the unit cell rotates, the chemical shifts change in some knowable way. The orientation in the template can then be confirmed by Grazing Incidence Small Angle X-ray Scanning (GIWAXS). Orientation of the unit cell is defined by Euler angles β and γ.[33]

2.3 *Results and Discussion*

The TOSS-t_1-deTOSS experimental spectrum presented in figure 2.6 was conducted as previously described on the monomer powder sample to extract CSA tensors of the carbonyl carbon (C15). The slice obtained (figure 2.7) corresponds to a pseudo one-dimensional ssNMR spectrum at slow spinning speeds. The fit of the sideband intensities was interpreted using Herzfeld-Berger analysis to give the three anisotropic chemical shifts presented in table 2.1, which are all in reasonable agreement with the theoretical chemical shifts.

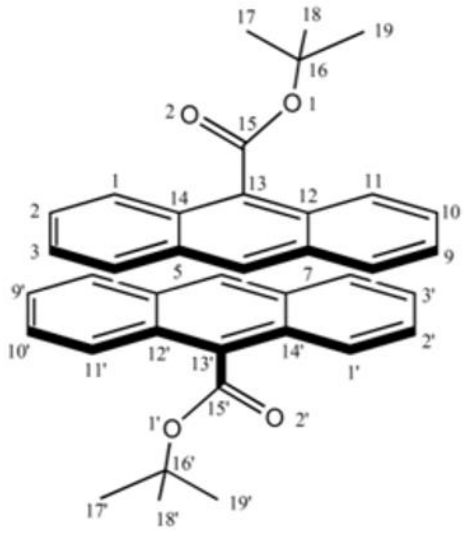

Figure 2.5: Numbering convention used for the 9TBAE monomer

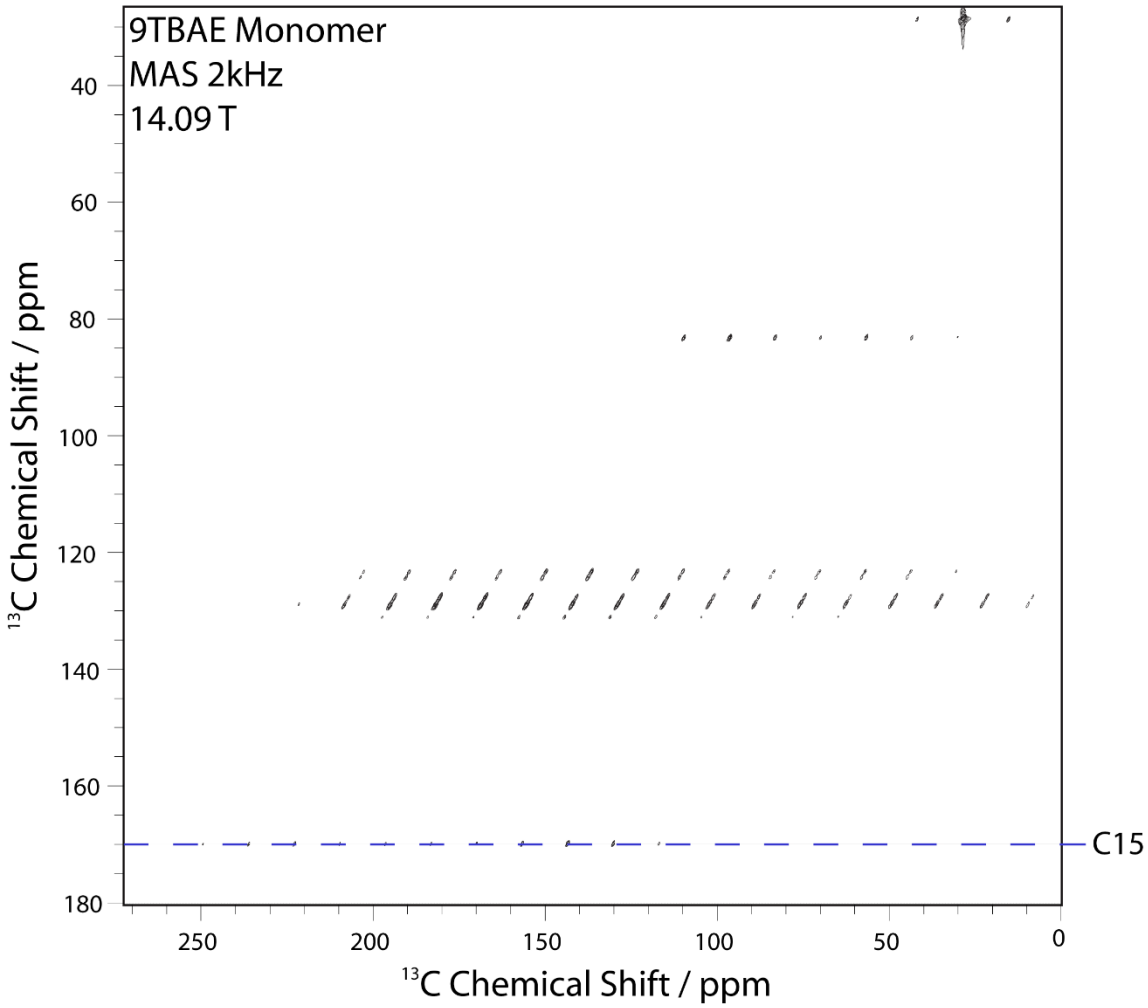

Figure 2.6: The TOSS-t_1-deTOSS spectrum of 9TBAE monomer powder with C15 labeled. The isotropic chemical shifts appear sideband free on the vertical axis, while the anisotropies appear on the horizontal axis.

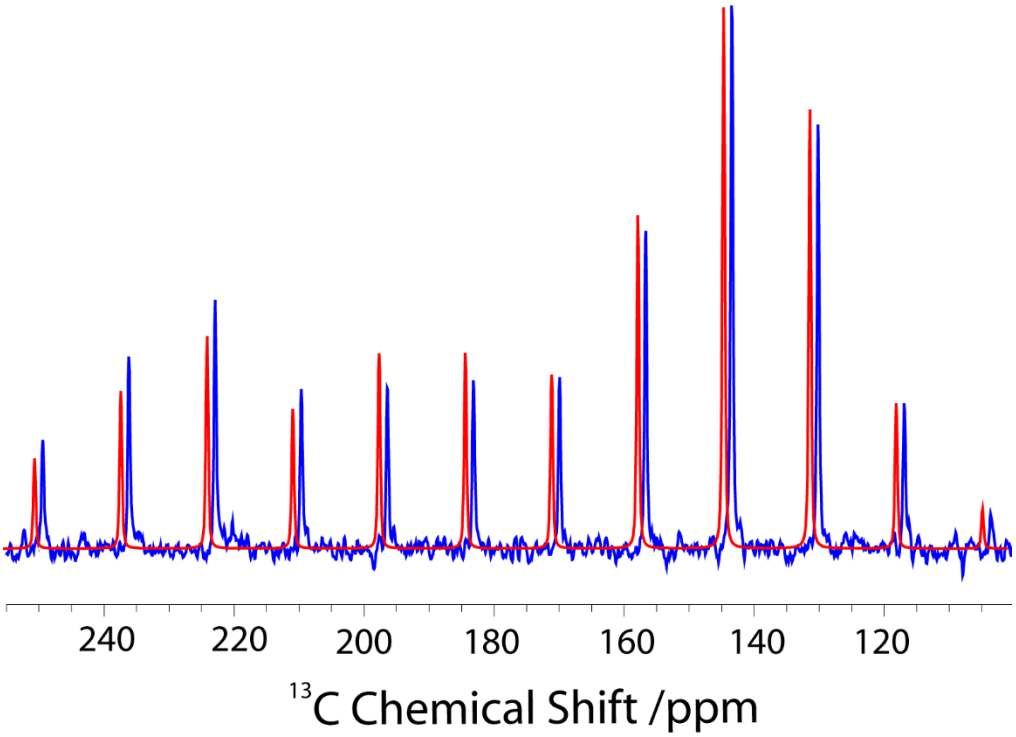

Figure 2.7: 1D horizontal trace of the TOSS-t_1-deTOSS spectrum corresponding to C15 (blue) used for the best fit of the intensities (red).

The xCSA experiment presented in figure 2.8 was conducted as previously described on the 9TBAE monomer powder sample. CSA tensors of the tert-butyl group made of the quaternary carbon (C16) and the methyl carbons (C17, C18, and C19) were extracted by summing the obtained one-dimensional slices and analyzing the fit of the sideband intensities using Herzfeld-Berger analysis (figure 2.9). The anisotropic chemical

shifts are presented in table 2.1, which are all in reasonable agreement with the theoretical chemical shifts.

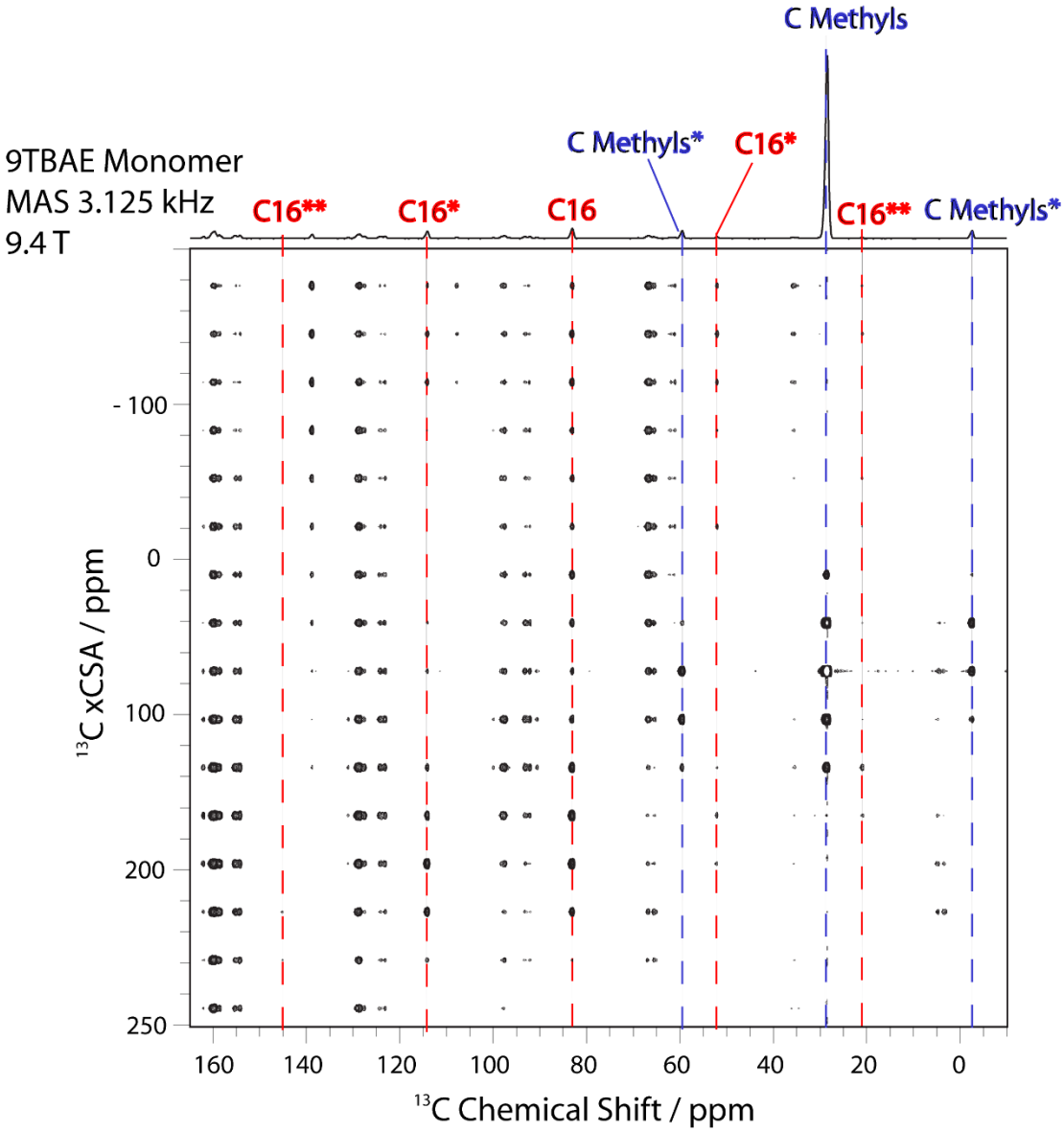

Figure 2.8: The xCSA spectrum of 9TBAE monomer powder with C16 and the methyl carbons (C17. C18, and C19) labeled. The isotropic chemical shift is on the horizontal axis while the anisotropies appear on the vertical axis.

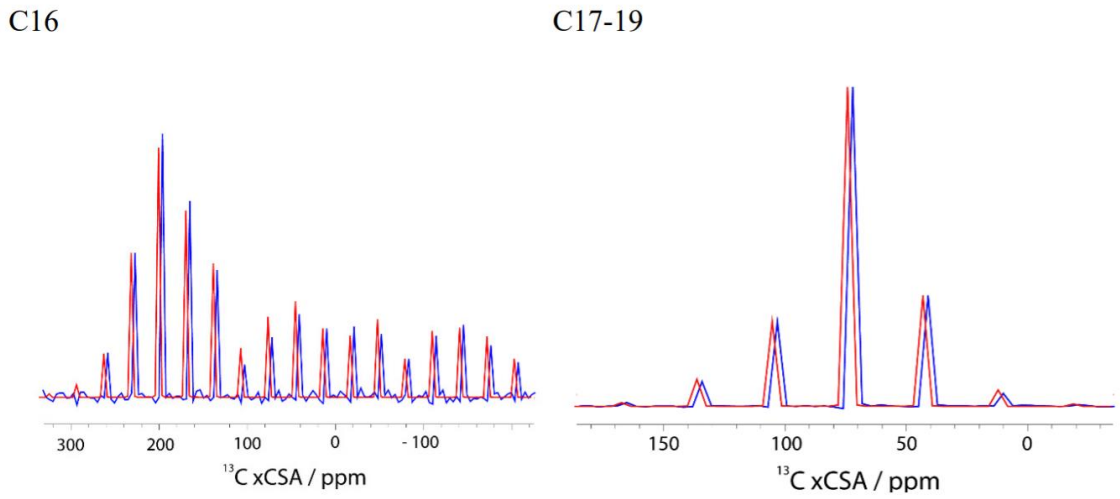

Figure 2.9: Sum of 1D vertical center and sideband traces of the xCSA spectrum corresponding (blue) used for the best fit of the intensities (red) for C15 and the methyl carbons.

	Experimental Shifts				Theoretical Shifts			
	Iso	σ_{11}	σ_{22}	σ_{33}	Iso	σ_{11}	σ_{22}	σ_{33}
C15	169.9	260.7	135.0	114.1	171.4	262.2	144.9	107.1
C16	83.2	112.8	106.7	30.2	83.3	115.4	105.5	28.9
C17-19	28.6	37.9	27.0	20.7	28.6	36.5	26.8	22.4

Table 2.1: Experimental isotropic and anisotropic chemical shifts of the 9TBAE monomer in ppm. C17-19 is reported as the average of the methyl carbon chemical shifts.

These additional chemical shift tensors being in good agreement with the first-principles calculated shifts confirm the accuracy of the previously obtained crystal structure of the 9TBAE monomer and SSRD.[14]

A large single crystal of t-bu labeled 9TBAE was prepared. The ^{13}C ssNMR spectrum is presented in figure 2.10. There are two magnetically inequivalent t-bu groups centered around 70 and 100 ppm that correspond with the asymmetric unit relative to the magnetic field. The three methyl carbons are magnetically equivalent owing to their fast rotation about the ester bond. A predicted spectrum was generated as a function of the unit cell orientation in the lab frame defined by Euler angles β and γ.[33] The orientation of the single crystal in the magnetic frame was determined to correspond with the crystal frame being rotated from the laboratory frame by Euler angles β = 19.2° and γ = 73.8°.

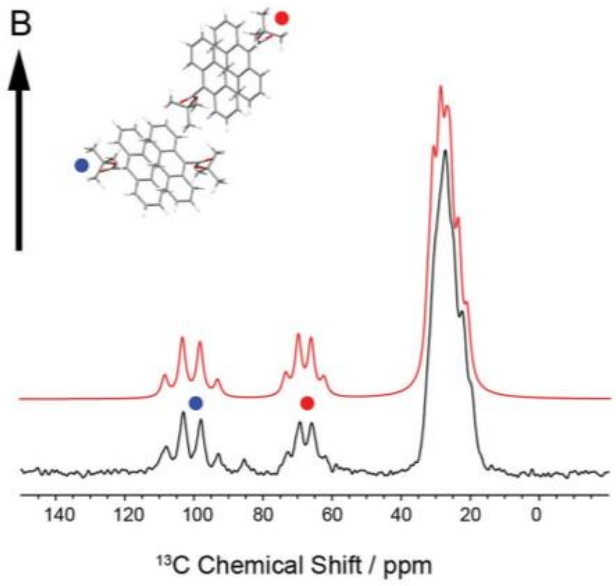

Figure 2.10: ^{13}C ssNMR spectrum of a bulk single crystal of t-bu labeled 9TBAE (black) and the best fit spectrum (red).

The ^{13}C ssNMR spectra of the 9TBAE monomer nanorods in an AAO template are presented in figure 2.11, with the 10% t-bu labeled sample on top and the 100% t-bu labeled sample on the bottom. The NMR resonances of the nanorod sample are broader than those of the single crystal. The 10% spectrum shows that this broadening is not a result of

intermolecular couplings since it shows the same amount of broadening compared to the single crystal. Rather, the broadening can be reproduced by assuming a Gaussian distribution of alignment angles with a standard deviation of ±3.6°. The best fit of the monomer corresponds to a rotation of the unit cell along the crystallographic *b* axis by Euler angles $\beta = 84.4°$ and $\gamma = 180°$.

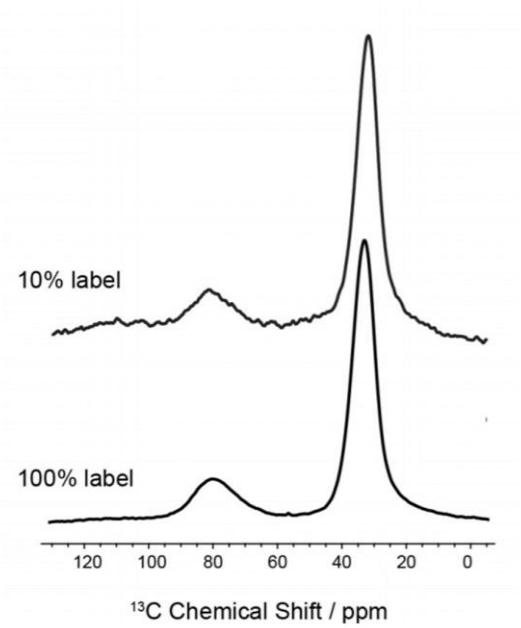

Figure 2.11: ^{13}C ssNMR spectrum of similarly oriented t-bu labeled 9TBAE monomer nanorods in an AAO template with 10% labeled on top and 100% labeled on bottom.

The evolution of the photodimerization reaction using ssNMR is shown in figure 2.12. The spectrum of the initial monomer containing template is taken, then the template is exposed to UV light in increments of 5 minutes and a spectrum is taken after each increment until the photodimerization is complete after 30 total minutes of exposure. The chemical shift corresponding with the quaternary carbon goes from

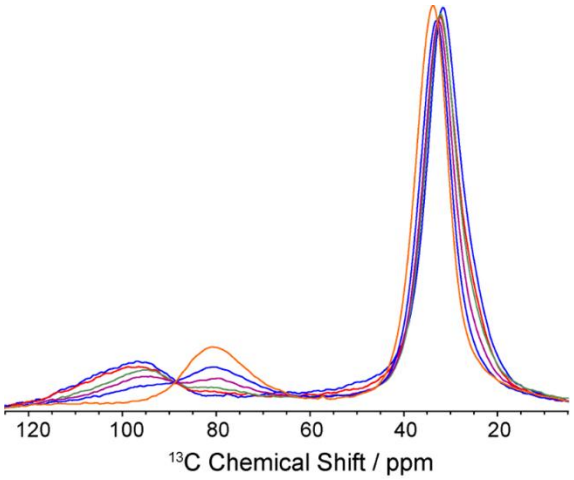

Figure 2.12: ^{13}C ssNMR spectra of similarly oriented t-bu labeled 9TBAE nanorods in an AAO template during progressive 5-minute increments of irradiation.

centered at around 80 ppm to centered at around 95 ppm. This transition from monomer to dimer is consistent with a two-state single-crystal-to-single-crystal reaction.

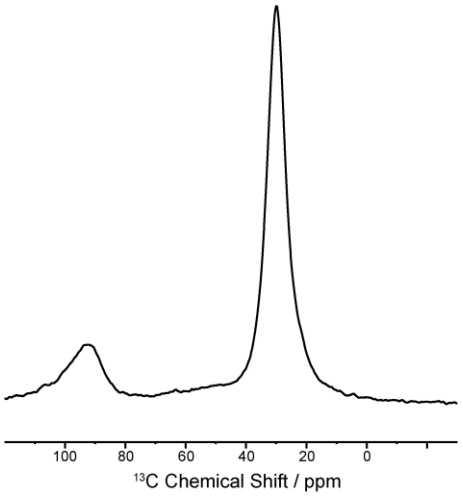

Figure 2.13: ^{13}C ssNMR spectrum of similarly oriented t-bu labeled 9TBAE SSRD nanorods.

The spectrum of the fully converted to SSRD nanorods is shown in figure 2.13. The best fit of the monomer corresponds to a rotation of the unit cell along the crystallographic *a* axis by Euler angles $\beta = 144.5°$ and $\gamma = 90.0°$. The GIWAXS data agreed with the ssNMR results, with alignments differing by only 5.6° for the monomer and by 2° for the dimer.

To further confirm the orientations determined from the t-bu label, a ^{13}C ssNMR spectra of 9TBAE monomer and SSRD with a carbonyl carbon (C15) label in an AAO template were also taken and are presented in figure 2.14. Both the carbonyl peaks of the monomer (left) and SSRD (right) are within the expected range given by the theoretical calculations and are in good agreement with the results obtained from the t-bu labeled AAO template experiments. Despite every synthetic step being confirmed by solution-state NMR showing clean carbonyl-labeled 9TBAE powder, a difficult to remove impurity emerged on the AAO template spectra. Given that the impurity peak continues to grow and the carbonyl peak begins to diminish upon further UV irradiation, the impurity could

correspond to a subsequent photoproduct of 9TBAE. The impurity could also correspond to a minor orientation that is favored upon irradiation.

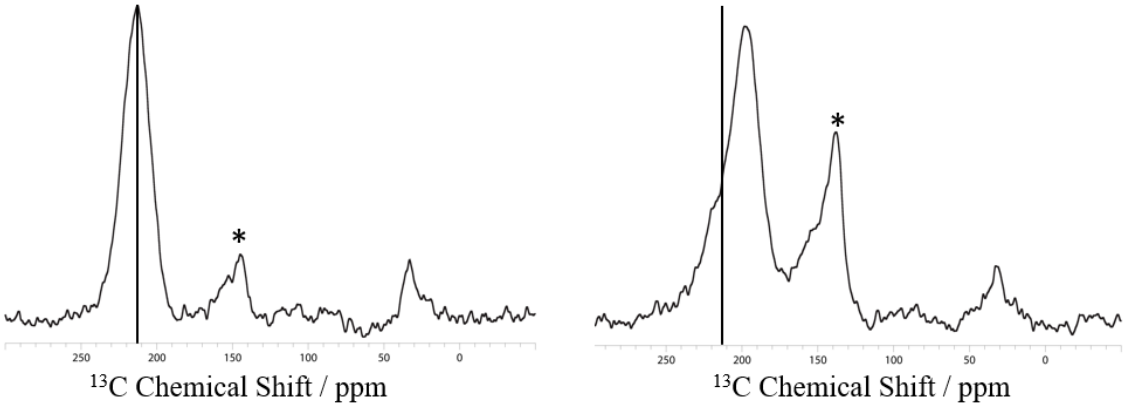

Figure 2.14: ^{13}C ssNMR spectrum of similarly oriented carbonyl labeled 9TBAE monomer (left) and SSRD (right) nanorods. The asterisk indicates an impurity in the sample

Given the crystal orientations for the monomer and SSRD of 9TBAE, the mechanism of the expansion can now be explained. First on a molecular level, figure 2.15 shows how the photodimerization reaction is consistent with the topochemical principle; dimerization occurs with minimal disruption to the crystal packing/ester side chain conformations.[34-36] It also shows how the motion of the reaction brings the anthracene rings into alignment, as seen on the left in the figure, but bends the planes out to accommodate the new sp^3 hybridization, as seen on the right, opening up space above and below the dimers that allows nearby pairs to

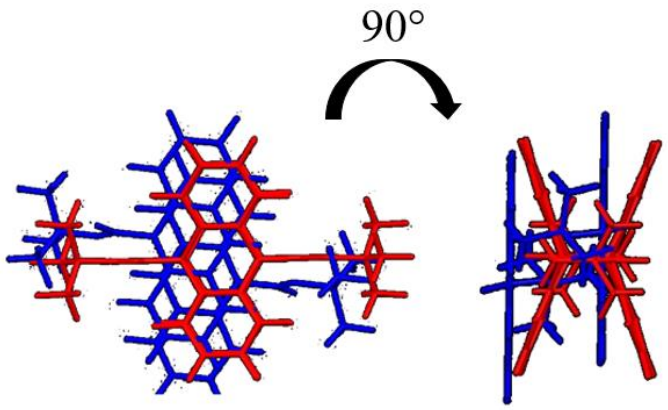

Figure 2.15: Two views of the 9TBAE monomer (blue) and dimer (red) overlapped.

stack more efficiently. The anthracene of the monomer becomes the protruding phenyl groups of the dimer which are responsible for the expansion.

On a macroscopic level, figure 2.16 shows the orientations of the 9TBAE monomer and SSRD relative to the nanorod axis along the *ac* and *ab* planes. It can be seen from the *ac* plane that the formation of the SSRD results in an expansion along the nanorod axis, while the *ab* plane shows a contraction perpindicular to the nanorod axis. To quantitatively measure the expansion of the nanorod, we tracked the *z*-displacement of a point on the nanorod *z*-axis on both the monomer and dimer. This model shows an expansion of 7.4% along the nanorod axis, which is in good agreement with the experimentally observed value of 8%. The model shows a contraction of 9.5% along the diameter of the rod.

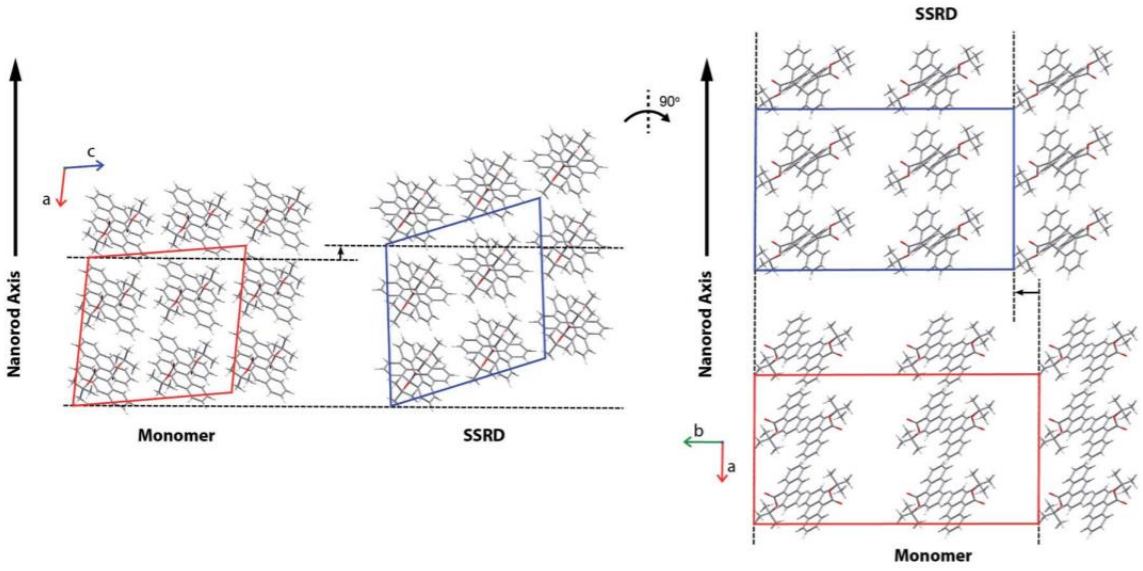

Figure 2.16: Orientations of the monomer and SSRD unit cells relative to the nanorod axis. Depending on the orientation, the photodimerization reaction can result in a net expansion along the nanorod axis (left) or a contraction perpendicular to the nanorod axis (right).

A maximum expansion of 9% could be obtained for 9TBAE monomer nanorods arranged at an optimal angle of the crystallographic *c* axis 15° off the nanorod axis. This

orientation aligns the expansion depicted in figure 2.16 along the rod axis. A maximum contraction of 9.5% is depicted on the right of figure 2.16, where the crystallographic *b* axis is aligned along the nanorod axis.

2.4 Conclusions and Future Work

For the first time, we have determined how a photochemical reaction has shifted molecular alignment and packing in a photoreactive crystal. We can predict an expansion of 7.4% for the 9TBAE crystal along the nanorod axis which is in good agreement with the experimentally observed value of 8%.

In terms of future work, for the 9TBAE nanorods specifically, uncertanties have generally been a result of small variations that are possible in the growth direction of the pores of the AAO template, which is responisble for the line broadening in the template spectra. This is also one possibility for the source of the impurity in the carbonyl labeled template samples. To get a more uniform sample growth would require more uniform channels that may be found in a different template. Attempts at nanorod growth on different templates has so far proven to be not as efficient as the currently used AAO templates.

The impurity in the carbonyl labeled template sample seems to grow after further irradiation, indicating the possibility of a possible subsequent photoproduct after the dimer is formed. While this possibility is not indicated by any of the other unlabeled and t-bu labeled spectra, it is worth exploring further as well.

Based on this work it is clear that the photochemical response of 9TBAE is not just dependent on the molecular shape, but also on the unit cell orientation. Additionally,

knowledge of the relative orientations of 9TBAE monomer and dimer unit cells have made it possible to predict the magnitude of expansion or contraction during the reaction. It is then theoretically possible that similar materials could be synthesized that will result in a specific desired motion upon photoreaction. Once the crystal structures of the monomer and dimer are known, a correlation can be established between crystal orientation and the movement of the crystal using this combined ssNMR, diffraction, and computation method.

2.5 References

(1) Koshima, H.; Ojima, N.; Uchimoto, H. Mechanical Motion of Azobenzene Crystals upon Photoirradiation. *Journal of the American Chemical Society* **2009**, *131*, 6890-6891.

(2) Kitagawa, D.; Kobatake, S. Crystal thickness dependence of the photoinduced crystal bending of 1-(5-methyl-2-(4-(p-vinylbenzoyloxymethyl)phenyl)-4-thiazolyl)-2-(5-methyl-2-phenyl-4-thiazolyl)perfluorocyclopentene. *Photochemical & Photobiological Sciences* **2014**, *13*, 764-769.

(3) Ohshima, S.; Morimoto, M.; Irie, M. Light-driven bending of diarylethene mixed crystals. *Chemical Science* **2015**, *6*, 5746-5752.

(4) Kitagawa, D.; Nishi, H.; Kobatake, S. Photoinduced Twisting of a Photochromic Diarylethene Crystal. *Angewandte Chemie International Edition* **2013**, *52*, 9320-9322.

(5) Zhu, L.; Al-Kaysi, R. O.; Bardeen, C. J. Reversible Photoinduced Twisting of Molecular Crystal Microribbons. *Journal of the American Chemical Society* **2011**, *133*, 12569-12575.

(6) Tong, F.; Al-Haidar, M.; Zhu, L.; Al-Kaysi, R. O.; Bardeen, C. J. Photoinduced peeling of molecular crystals. *Chemical Communications* **2019**, *55*, 3709-3712.

(7) Kim, T.; Zhu, L.; Mueller, L. J.; Bardeen, C. J. Mechanism of Photoinduced Bending and Twisting in Crystalline Microneedles and Microribbons Composed of 9-Methylanthracene. *Journal of the American Chemical Society* **2014**, *136*, 6617-6625.

(8) Warner, M.; Mahadevan, L. Photoinduced deformations of beams, plates, and films. *Physical Review Letters* **2004**, *92*, 134302.

(9) Liu, G.; Liu, J.; Liu, Y.; Tao, X. Oriented Single-Crystal-to-Single-Crystal Phase Transition with Dramatic Changes in the Dimensions of Crystals. *Journal of the American Chemical Society* **2014**, *136*, 590-593.

(10) Nakanish, H.; Jones, W.; Thomas, J. M.; Hursthouse, M. B.; Motevalli, M. Monitoring the crystallographic course of a single-crystal → single-crystal photodimerization by X-ray diffractometry. *Journal of the Chemical Society, Chemical Communications* **1980**, 611-612.

(11) Huang, S.-L.; Hor, T. S. A.; Jin, G.-X. Photodriven single-crystal-to-single-crystal transformation. *Coordination Chemistry Reviews* **2017**, *346*, 112-122.

(12) Chaudhary, A.; Mohammad, A.; Mobin, S. M. Recent Advances in Single-Crystal-to-Single-Crystal Transformation at the Discrete Molecular Level. *Crystal Growth & Design* **2017**, *17*, 2893-2910.

(13) Friščić, T.; MacGillivray, L. R. Single-crystal-to-single-crystal [2 + 2] photodimerizations: from discovery to design. *Zeitschrift für Kristallographie - Crystalline Materials* **2005**, *220*, 351-363.

(14) Yang, C.; Zhu, L.; Kudla, R. A.; Hartman, J. D.; Al-Kaysi, R. O.; Monaco, S.; Schatschneider, B.; Magalhaes, A.; Beran, G. J. O.; Bardeen, C. J.; Mueller, L. J. Crystal structure of the meta-stable intermediate in the photomechanical, crystal-to-crystal reaction of 9-tert-butyl anthracene ester. *CrystEngComm* **2016**, *18*, 7319-7329.

(15) Al-Kaysi, R. O.; Muller, A. M.; Bardeen, C. J. Photochemically driven shape changes of crystalline organic nanorods. *J. Am. Chem. Soc.* **2006**, *128*, 15938-15939.

(16) Nieuwendaal, R. C.; Bertmer, M.; Hayes, S. E. An Unexpected Phase Transition during the [2 + 2] Photocycloaddition Reaction of Cinnamic Acid to Truxillic Acid: Changes in Polymorphism Monitored by Solid-State NMR. *The Journal of Physical Chemistry B* **2008**, *112*, 12920-12926.

(17) Nieuwendaal, R. C.; Mattler, S. J.; Bertmer, M.; Hayes, S. E. Single Crystal to Single Crystal Topochemical Photoreactions: Measuring the Degree of Disorder in the [2+2] Photodimerization of trans-Cinnamic Acid Using Single-Crystal C-13 NMR Spectroscopy. *J Phys Chem B* **2011**, *115*, 5785-5793.

(18) Facelli, J. C.; Grant, D. M. Determination of molecular symmetry in crystalline naphthalene using solid-state NMR. *Nature* **1993**, *365*, 325-327.

(19) Olsen, R. A.; Struppe, J.; Elliott, D. W.; Thomas, R. J.; Mueller, L. J. Through-Bond 13C−13C Correlation at the Natural Abundance Level: Refining Dynamic Regions in the Crystal Structure of Vitamin-D3 with Solid-State NMR. *Journal of the American Chemical Society* **2003**, *125*, 11784-11785.

(20) Mueller, L. J.; Dunn, M. F. NMR Crystallography of Enzyme Active Sites: Probing Chemically Detailed, Three-Dimensional Structure in Tryptophan Synthase. *Accounts of Chemical Research* **2013**, *46*, 2008-2017.

(21) Al-Kaysi, R. O.; Dillon, R. J.; Kaiser, J. M.; Mueller, L. J.; Guirado, G.; Bardeen, C. J. Photopolymerization of Organic Molecular Crystal Nanorods. *Macromolecules* **2007**, *40*, 9040-9044.

(22) Morcombe, C. R.; Zilm, K. W. Chemical shift referencing in MAS solid state NMR. *Journal of Magnetic Resonance* **2003**, *162*, 479-486.

(23) Giannozzi, P.; Baroni, S.; Bonini, N.; Calandra, M.; Car, R.; Cavazzoni, C.; Ceresoli, D.; Chiarotti, G. L.; Cococcioni, M.; Dabo, I.; Dal Corso, A.; de Gironcoli, S.; Fabris, S.; Fratesi, G.; Gebauer, R.; Gerstmann, U.; Gougoussis, C.; Kokalj, A.; Lazzeri, M.; Martin-Samos, L.; Marzari, N.; Mauri, F.; Mazzarello, R.; Paolini, S.; Pasquarello, A.; Paulatto, L.; Sbraccia, C.; Scandolo, S.; Sclauzero, G.; Seitsonen, A. P.; Smogunov, A.; Umari, P.; Wentzcovitch, R. M. QUANTUM ESPRESSO: a modular and open-source software project for quantum simulations of materials. *Journal of physics. Condensed matter : an Institute of Physics journal* **2009**, *21*, 395502.

(24) Frisch, M. J.; Trucks, G. W.; Schlegel, H. B.; Scuseria, G. E.; Robb, M. A.; Cheeseman, J. R.; Scalmani, G.; Barone, V.; Petersson, G. A.; Nakatsuji, H.; Li, X.; Caricato, M.; Marenich, A. V.; Bloino, J.; Janesko, B. G.; Gomperts, R.; Mennucci, B.; Hratchian, H. P.; Ortiz, J. V.; Izmaylov, A. F.; Sonnenberg, J. L.; Williams; Ding, F.; Lipparini, F.; Egidi, F.; Goings, J.; Peng, B.; Petrone, A.; Henderson, T.; Ranasinghe, D.; Zakrzewski, V. G.; Gao, J.; Rega, N.; Zheng, G.; Liang, W.; Hada, M.; Ehara, M.; Toyota, K.; Fukuda, R.; Hasegawa, J.; Ishida, M.; Nakajima, T.; Honda, Y.; Kitao, O.; Nakai, H.; Vreven, T.; Throssell, K.; Montgomery Jr., J. A.; Peralta, J. E.; Ogliaro, F.; Bearpark, M. J.; Heyd, J. J.; Brothers, E. N.; Kudin, K. N.; Staroverov, V. N.; Keith, T. A.; Kobayashi, R.; Normand, J.; Raghavachari, K.; Rendell, A. P.; Burant, J. C.; Iyengar, S. S.; Tomasi, J.; Cossi, M.; Millam, J. M.; Klene, M.; Adamo, C.; Cammi, R.; Ochterski, J. W.; Martin, R. L.; Morokuma, K.; Farkas, O.; Foresman, J. B.; Fox, D. J.: Gaussian 16 Rev. C.01. Wallingford, CT, 2016.

(25) Hartman, J. D.; Monaco, S.; Schatschneider, B.; Beran, G. J. O. Fragment-based 13C nuclear magnetic resonance chemical shift predictions in molecular crystals: An alternative to planewave methods. *The Journal of Chemical Physics* **2015**, *143*, 102809.

(26) Beran, G. J. O. Approximating quantum many-body intermolecular interactions in molecular clusters using classical polarizable force fields. *The Journal of Chemical Physics* **2009**, *130*, 164115.

(27) Hartman, J. D.; Kudla, R. A.; Day, G. M.; Mueller, L. J.; Beran, G. J. O. Benchmark fragment-based 1H, 13C, 15N and 17O chemical shift predictions in molecular crystals. *Physical Chemistry Chemical Physics* **2016**, *18*, 21686-21709.

(28) Kolbert, A. C.; Griffin, R. G. Two-dimensional resolution of isotropic and anisotropic chemical shifts in magic angle spinning NMR. *Chemical Physics Letters* **1990**, *166*, 87-91.

(29) Hung, I.; Gan, Z. H. An efficient amplification pulse sequence for measuring chemical shift anisotropy under fast magic-angle spinning. *Journal of Magnetic Resonance* **2011**, *213*, 196-199.

(30) Herzfeld, J.; Berger, A. E. Sideband intensities in NMR spectra of samples spinning at the magic angle. *The Journal of Chemical Physics* **1980**, *73*, 6021-6030.

(31) Young, R. P.; Lewis, C. R.; Yang, C.; Wang, L.; Harper, J. K.; Mueller, L. J. TensorView: A software tool for displaying NMR tensors. *Magnetic Resonance in Chemistry* **2019**, *57*, 211-223.

(32) Mathematica, Version 12.2. https://www.wolfram.com/mathematica.

(33) Mueller, L. J. Tensors and rotations in NMR. *Concepts in Magnetic Resonance Part A* **2011**, *38A*, 221-235.

(34) Schmidt, G. M. J. Photodimerization in the solid state. *Pure and Applied Chemistry* **1971**, *27*, 647-678.

(35) Shang, W.; Hickey, M. B.; Enkelmann, V.; Snider, B. B.; Foxman, B. M. Chemo- and stereospecific solid-state dimerization of lithium trans-2-butenoate and lithium trans-2-butenoate formamide solvate. *CrystEngComm* **2011**, *13*, 4339-4350.

(36) Biradha, K.; Santra, R. Crystal engineering of topochemical solid state reactions. *Chemical Society Reviews* **2013**, *42*, 950-967.

Chapter 3 – DNP-SENS of Silica Surfaces to Probe Non-Covalent Recognition of Substrates

3.1 Introduction

Non-covalent recognition of substrates has been incorporated in the solution phase but is left unexplored on solid surfaces of porous materials. The design of these porous materials is limited by the lack of characterization of species tethered on their surfaces and their counterparts in solution. ssNMR has been well established as a method of providing detailed information on the structure and dynamics of these heterogeneous systems. As previously discussed, however, ssNMR is generally limited by its lack of sensitivity. Dynamic Nuclear Polarization – Surface Enhanced NMR Spectroscopy (DNP-SENS) has been recently developed and is shown to improve the sensitivity of ssNMR experiments.[1-3] This method has also been applied to the study of surface sites of porous materials.[4-9]

SBA-15 is a silica nanoparticle support commonly used in these types of studies. SBA-15 is a mesoporous silica matrix which allows for modification at the surface and with hexagonal pores of 6-8 nm. The pore size allows for interaction with solvent containing radical, the source of the polarization enhancement in DNP. The atomic level structure of SBA-15 is depicted in figure 3.1, where the siloxane groups are the bulk of the material and the hydroxyl groups can be modified on the surface[10-12]. Figure 3.2 represents the pores as white space and

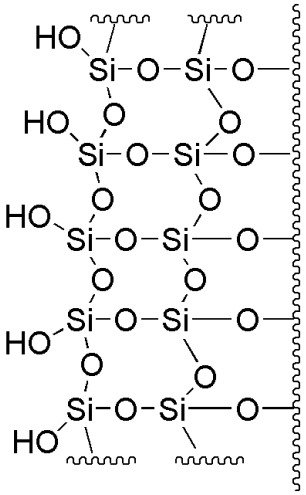

Figure 3.1: Atomic level depiction of SBA-15, where siloxane make up the bulk and hydroxyl groups on the surface.

the silica walls as the grey area. The added functionalized groups occupy the space in the pores.

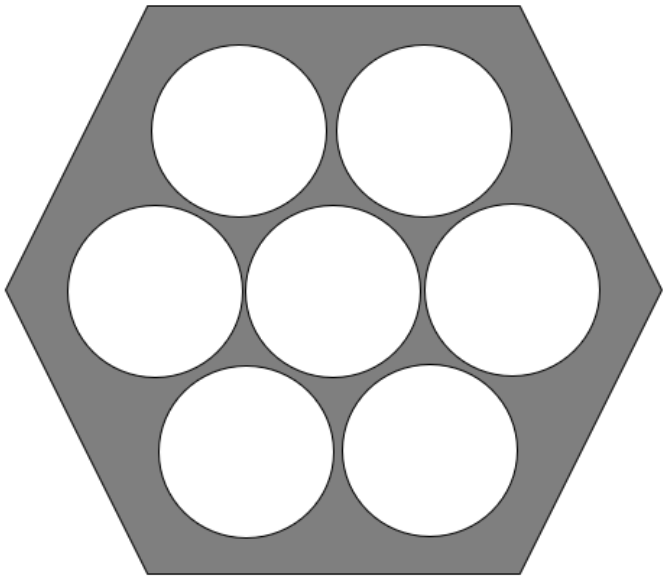

Figure 3.2: Straight on view of the pores in SBA-15.

Surfaces of materials play an important role in their performance as heterogeneous catalysts. Catalysts with an SBA-15 support have a variety of applications, such as drug delivery and biodiesel production.[13-16] Knowledge specifically at the surface, not of the bulk property, is necessary for development of functional materials including heterogeneous catalysts. Spectroscopic methods such as UV-VIS or Rama Spectroscopy give average structural properties dominated by the bulk structure without giving atomic level characterization of the surface[17]. ssNMR, however, is a method that probes local structures since NMR is a technique sensitive to the nearby environment of the observed nuclei. Many previous studies use DNP on solid surfaces in materials, but none have

explored non-covalent bonding on those surfaces[4-9]. The enhancement provided by DNP should provide for the sensitivity and selectivity necessary to observe these interactions.

3.2 Experimental Methods

General DNP experiments enhance NMR signal using a similar calculation as Cross Polarization but relies on different mechanisms of polarization transfer. Instead of using the increased gyromagnetic ratio of hydrogen, DNP uses the gyromagnetic ratio of the electron. The source of the electron is typically from a radical added to the solid sample through a solvent. This results in a theoretical enhancement of NMR signal of hydrogen of up to 660. Enhancement, however, is limited by several factors including the type of sample, the polarization agent used, and the magnetic field strength of the magnet. DNP experiments are also conducted around 100 K as a middle ground between the maximum possible polarization transfer and maximum hardware capabilities.[9] As such, DNP also requires a source of high power microwaves (MW), an MAS probe capable of operating at cryogenic temperatures, and a method of transporting microwaves to the sample in the probe, in addition to a DNP-NMR magnet. Nitrogen gas is used as the bearing and drive gases to spin the rotor, and a third gas line cools the sample.[18] The source of the MW is typically a gyrotron with frequencies of the wave dependent on the size of the magnetic field of the magnet. The gyrotron output beam is transferred to the probe via a corrugated waveguide, and an additional waveguide focuses MW irradiation onto the spinning rotor.[1,3,9,19]

DNP experiments are performed on a Bruker Biospin solid-state DNP-NMR spectrometer with a 9.4 T magnet (frequencies of 400 MHz for ^{1}H, 100.7 MHz for ^{13}C, 79.5 MHz for ^{29}Si, and 40.6 MHz for ^{15}N) equipped with an Avance III HD console and a 3.2 mm triple resonance MAS DNP-NMR probe. Samples are obtained at an MAS spinning frequency of 8 kHz and at 90 K. Microwaves are produced from 25 W gyrotron microwave source.

Figure 3.3: The gyrotron magnet used in these experiments at the Materials Research Lab at UCSB.

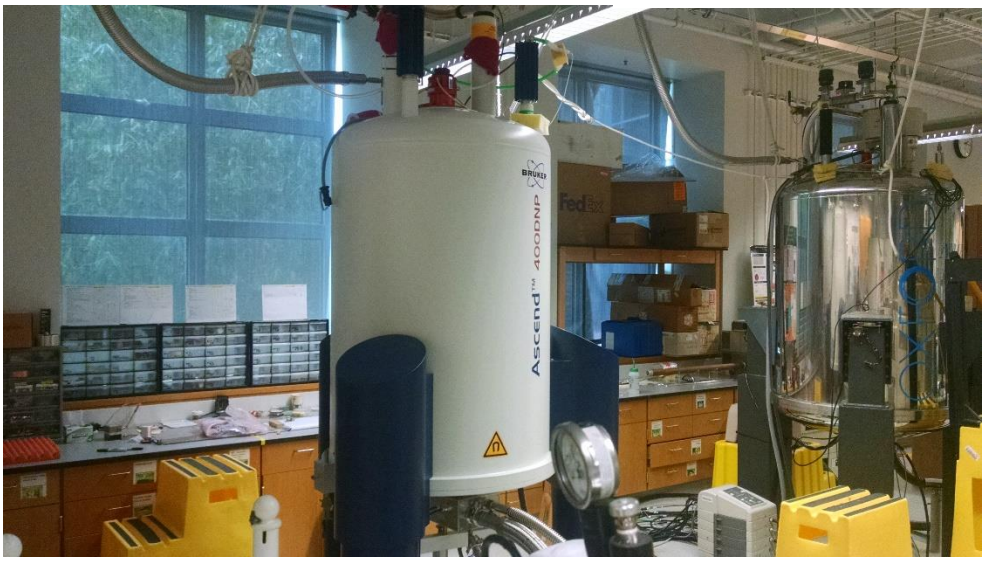

Figure 3.4: DNP-NMR magnet used in these experiments at the Materials Research Lab at UCSB.

Additional non-DNP experiments were performed on a Bruker AVIII spectrometer with a 9.4 T magnet and 4 mm MAS probe spinning at MAS rates of 8 kHz at room temperature. CP was implemented using a spin lock field of 45 kHz on ^{1}H, 54 kHz on ^{13}C, 37 kHz on ^{15}N, and 43 kHz on ^{29}Si. ^{13}C chemical shifts were referenced indirectly to neat TMS via adamantane with the downfield-shifted peak set to 38.48 ppm.[20]

Once radical in solvent is introduced to a sample, and the microwaves are turned on, electron spin polarization is spread to nearby coupled nuclei, then to the bulk nuclei via homonuclear spin diffusion.[21] This can be achieved by a variety of mechanisms. The polarization transfer mechanisms that must be considered in DNP are the Overhauser Effect (OE), the Solid Effect (SE), the Cross Effect (CE), and Thermal Mixing (TM). OE and SE are the dominant mechanisms when the nuclear Larmor frequency is larger than the EPR linewidth. This is typical of the thin linewidth found in monoradicals as the source of electrons. Thermal mixing is not significantly active at low temperatures. When the EPR linewidth is broader than the nuclear Larmor, as is the case with biradicals used in DNP studies of surface sites of porous materials, then spin polarization by the Cross Effect mechanism is initiated.[22,23] Microwave irradiation causes an electron spin transition at one electron on the biradical and the electron coupled to it, while also inducing a nuclear spin transition to a hydrogen atom. Polarization

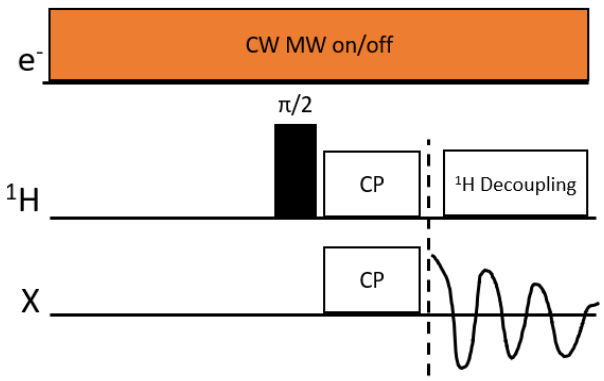

Figure 3.5: The DNP pulse sequence

from the hydrogen is spread by spin diffusion through the solvent and sample of interest. Standard Cross Polarization can then be used to transfer polarization from the hydrogen to other nuclei of interest (figure 3.7).[21-25]

The selection of radical and solvent used in a DNP experiment is critical. Incompatible radicals or solvents can result in low enhancement or destruction of the sample while correct selection can result in high enhancement and massive time savings. An important property of the selected solvent is its ability to spready the radical evenly throughout a sample, which is why commonly available solvents such as water, with glycerol to prevent aggregation of the radical, is frequently used. Aqueous solvents, however, were found to be incompatible with materials with hydrophobic surfaces or reactive centers, so non-aqueous solvents and corresponding radicals were also developed.[4] Both aqueous and non-aqueous solvents were used to determine which would be more compatible with our sample.

The water soluble biradical TOTAPOL was developed by Song et al. to have effective enhancement in low temperature MAS experiments.[26] However, to take full advantage of the mechanisms of polarization transfer, more rigid biradicals were developed. Sauvée et al. developed AMUPOL (figure 3.6, left) with greater DNP efficiency in aqueous solvents and maximum enhancements at lower temperatures.[27] AMUPOL is now a readily available biradical for use in DNP experiments. A heavily deuterated aqueous solvent is also common in DNP to optimize the ^{1}H-^{1}H spin diffusion that spreads polarization throughout the solvent and sample of interest. Without a deuterated solvent,

polarization could build up in the solvent only.[28] Based on this, the biradical AMUPOL in 90/10 D_2O/H_2O as a solvent was selected for these experiments.

For non-aqueous solvents, Zagdoun et al. produced a study with the biradical bTbK in which they determined that good solvents should be inert towards both the radical and material of interest, should have low vapor pressure, and must be frozen at DNP temperatures. They found that halogenated solvents generally give better DNP enhancement than protonated ones due to the lack of protons leading to direct polarization transfer to the molecule of interest. Of the organic solvents in the study, TCE produced the greatest enhancement.[29]

The bTbK biradical was found to give higher enhancement than TOTAPOL under similar conditions and is more soluble in organic solvents.[30] Zagdoun et al. looked at a variety of bTbK derivatives and established the link between DNP efficiency and electronic relaxation times. This resulted in the synthesis of a new radical, TEKPOL (figure 3.6, right), which is one of the most efficient DNP radicals due to its electron relaxation properties, high molecular weight, and a lack of methyl groups close to the nitroxyl groups.[31,32] Based on this, TEKPOL in TCE was used as our radical in solvent.

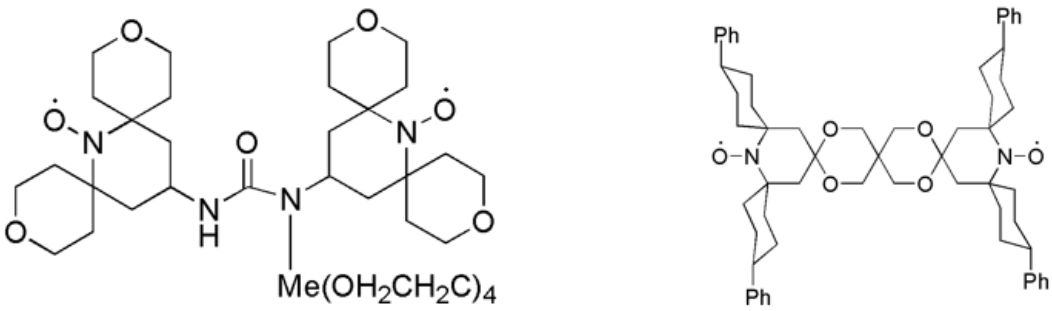

Figure 3.6: The biradicals AMUPOL (left) and TEKPOL (right) frequently used in DNP experiments

The radical in solvent is introduced to the powder sample by incipient wetness impregnation. 22μL of 16 mM radical in solvent is added to 20 mg of sample to form a translucent slush.[33] The sample is packed into a 3.2 mm sapphire rotor. To degass the sample, the rotor was inserted and spun inside the probe for 2 minutes, then ejected and allowed to sit in the insert/eject chamber under the eject gas flow. This insert/eject cycle was done 3 times. This has been shown as an efficient method of increasing enhancement by removing adsorbed oxygen which contributes to relaxation.[34,35]

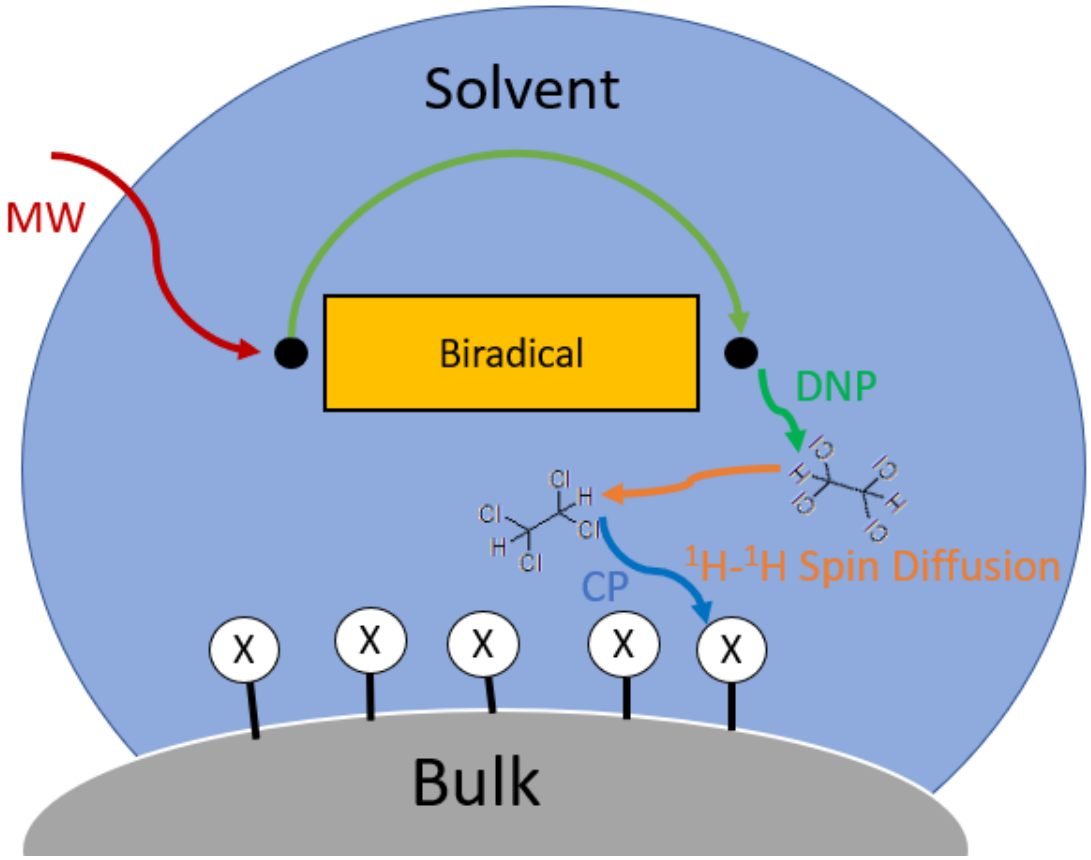

Figure 3.7: Polarization transfer by Cross Effect DNP-SENS. This example uses TCE as the solvent. Microwave irradiation hits one electron on the biradical in solvent and the CE mechanism causes an electron spin transition at the other electron while also inducing a nuclear spin transition on a hydrogen atom on the solvent. The polarization is spread by spin diffusion to other ^{1}H and brought to the nuclei of interest on the surface of the sample by standard CP.

To probe interactions at the surface of the nanoparticle, the SBA-15 surface is modified to host a tether containing an N-[(butylamino)carbonyl]-6-methylisoctysine group (Propyl Urea). This is done by reacting TES Propyl Urea (figure 3.8) with SBA-15.[36] In order to make the surface more compatible with the non-polar solvent TCE, which should correspond with greater enhancement over the H_2O/D_2O solvent, the SBA-15 surface will be passivated with TMS-d9. This converts most of the polar hydroxyl groups at the surface to non-polar deuterated TMS groups (figure 3.9). This has the additional benefit of limiting the protons on the surface which could act as a polarization sink.[37] Once the passivation and tether are confirmed and can be observed using the enhancement of DNP, an attempt will be made to pair the propyl urea tether by non-covalent bonding. The paired molecule chosen is a propyl urea derivative (iso-octyl upy) (figure 3.10) because it will have distinctive ^{13}C chemical shifts that can be distinguished from the propyl urea SBA-15. This non-covalent interaction is known to exist (as [(butylamino)carbonyl]-6-methylisoctysine dimerizes in supramolecular polymers), but is not well characterized.

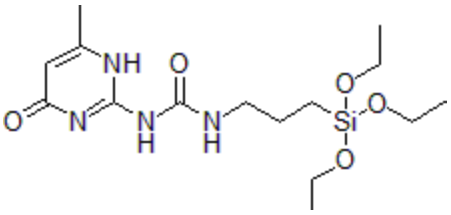

Figure 3.8: TES Propyl Urea

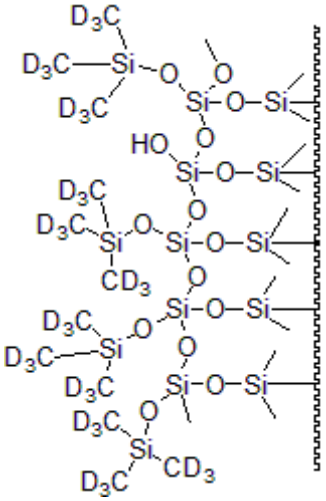

Figure 3.9: Passivated SBA-15 at the surface. Most hydroxyl groups are replaced with deuterated TMS

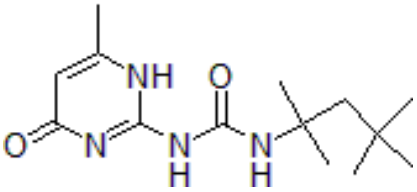

Figure 3.10: Iso-octyl upy

DNP experiments are often reported along with their enhancement, which will also be shown with some of our results. Enhancement (ε) is the ratio of integrated intensities of the biggest peaks between microwave on and microwave off spectra. Both are taken at low temperatures with the impregnated sample. Time savings correspond to the enhancement squared, and enhancements can be between 10 and 200, meaning significant time savings in the experiments. Absolute enhancement (Σ), which is the comparison of a microwave on DNP experiment to a conventional NMR experiment, may also be reported.[4,22,38]

3.3 Results and Discussion

^{13}C DNP experiments were conducted on the propyl urea tethered SBA-15 (figure 3.11) with 16 mM of TEKPOL in TCE. The spectra of MW on and off spectra (figure 3.12) show there is an enhancement of 30, which corresponds to what we would expect for carbon.[6] There is a large solvent peak, which is typical for DNP experiments with an undeuterated solvent, allowing some polarization to stay in the solvent. The signal allows us to confirm ethoxy sites on the sample, which are leftover leaving groups from the precursor TES propyl urea. These correspond with a distribution of bonding sites at the

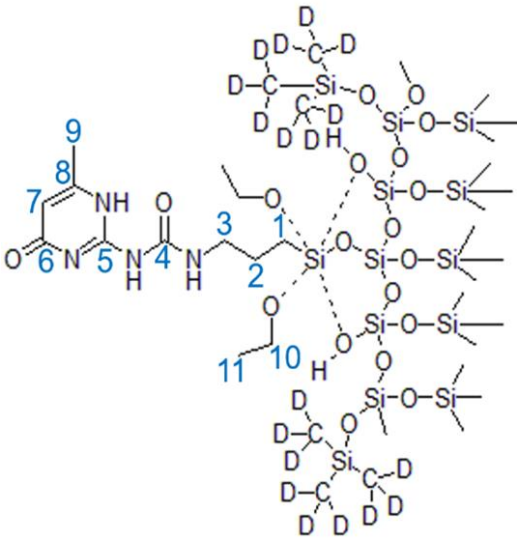

Figure 3.11: Propyl urea tethered SBA-15 with labels on the carbons

interface between the surface and the silica matrix. This distribution will be explored further with the presentation of the ^{29}Si spectrum.

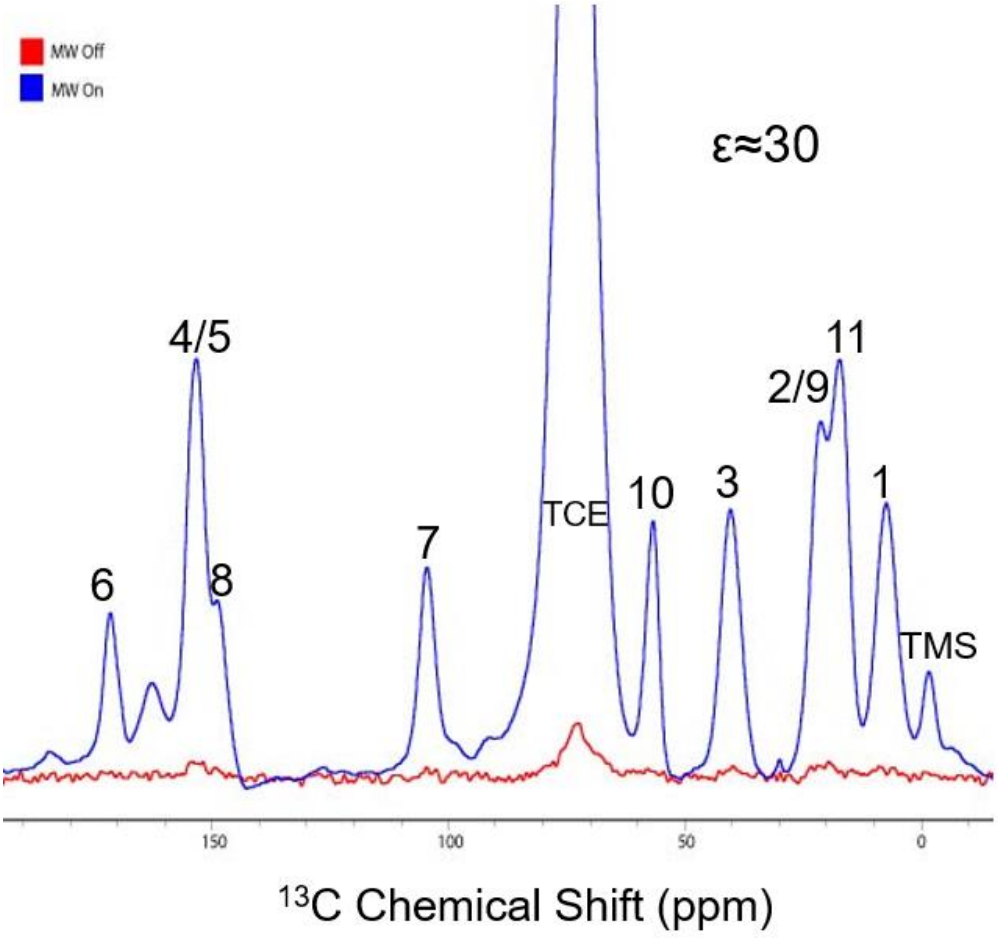

Figure 3.12: ^{13}C DNP spectrum of propyl urea tethered SBA-15

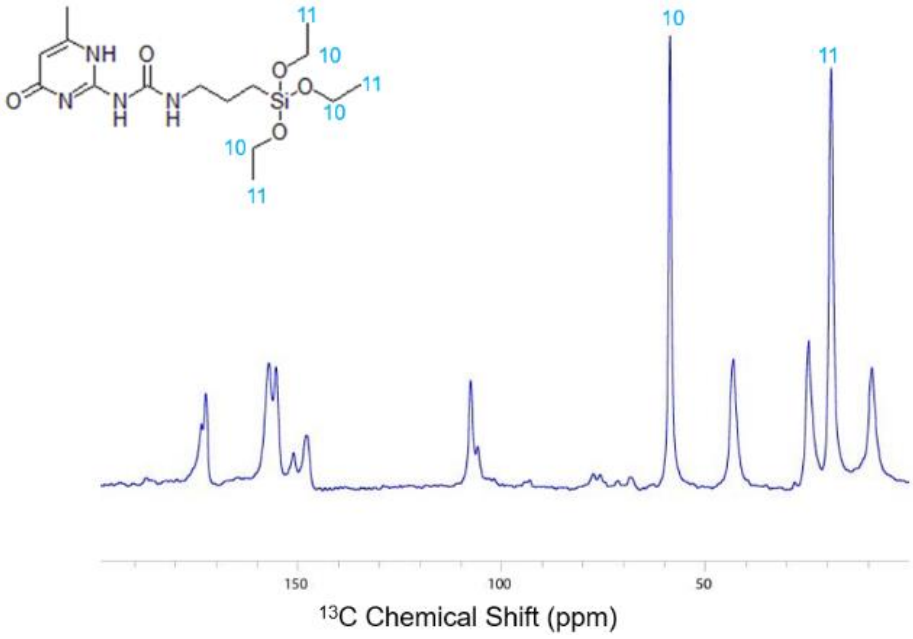

Figure 3.13: ^{13}C CP ssNMR spectrum of TES propyl urea.

The chemical shifts of the ethoxy leaving groups were confirmed by a non-DNP ^{13}C spectrum of TES propyl urea (figure 3.13).

Structure	Site Name	Approximate Chemical Shift (ppm)
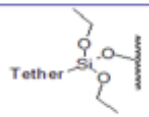	T^1	-50
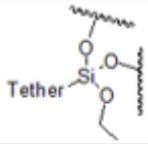	T^2	-59
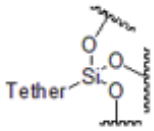	T^3	-68
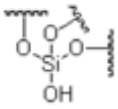	Q^3	-100
	Q^4	-110
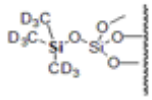	TMS-d9	-13
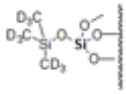	$Q^{4'}$	-110

Table 3.1: Useful ^{29}Si chemical shifts for tethered SBA-15

^{29}Si assignments corresponding to certain sites on tethered SBA-15 have been compiled into table 3.1.[5,39,40] T sites are sites at the interface between the bulk and the surface. T^1 sites are bonded to two remaining ethoxy leaving groups, T^2 sites bonded to one remaining ethoxy leaving group, and T^3 sites are not bonded to any ethoxy leaving groups. Q sites are bonded to four oxygens, with Q^3 sites at the surface bonded to one unreacted hydroxyl grounp. Q^4 corresponds to the siloxane sites in the bulk material. $Q^{4'}$ and TMS-d9 are the two silicon sites in the TMS-d9 on the surface.

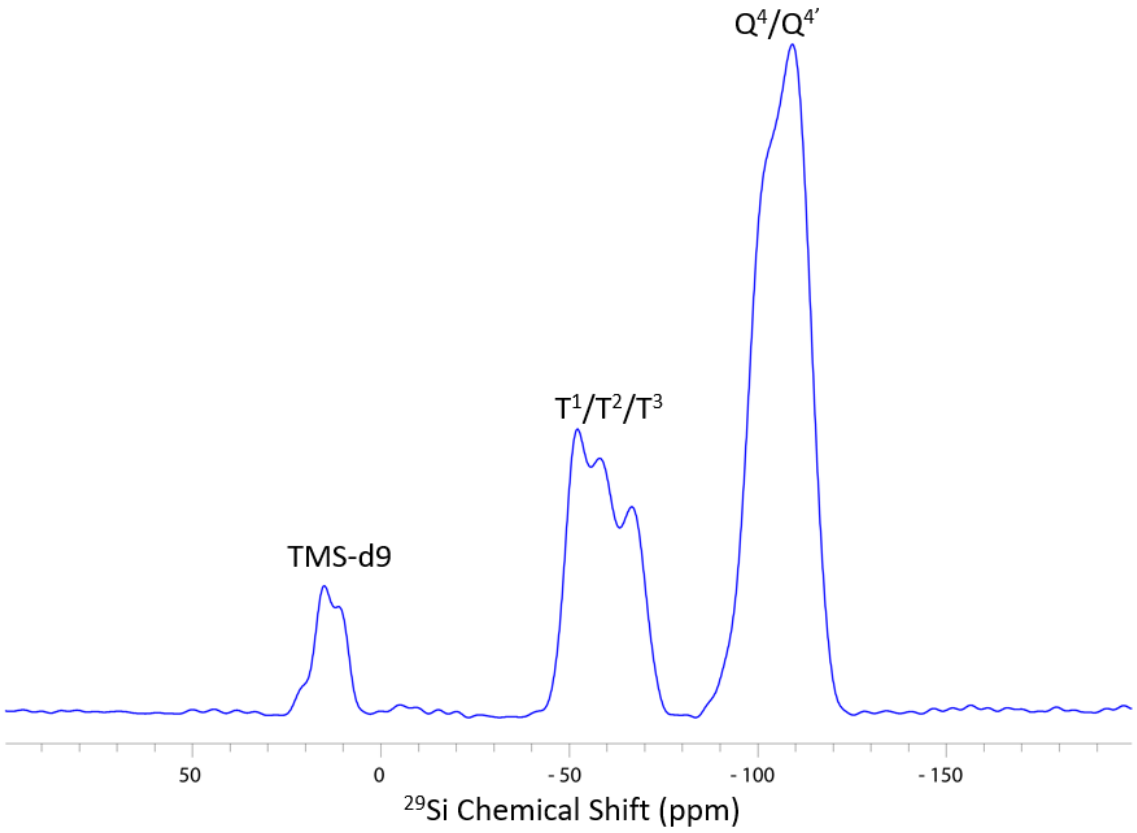

Figure 3.14: ^{29}Si DNP spectrum of propyl urea tethered SBA-15

The ^{29}Si DNP spectrum (figure 3.14) confirms the distribution of T sites at the surface corresponding to the ethoxy leaving groups from the TES propyl urea. The spectrum also confirms the appearance of TMS-d9 groups in the TMS-d9 and $Q^{4'}$ sites. However, a quantitative treatment for the sites converted at the surface and the T sites are unreliable based on CP and DNP spectra since they select for sites which are closer in space to protons and are the source of the increased polarization transfer.

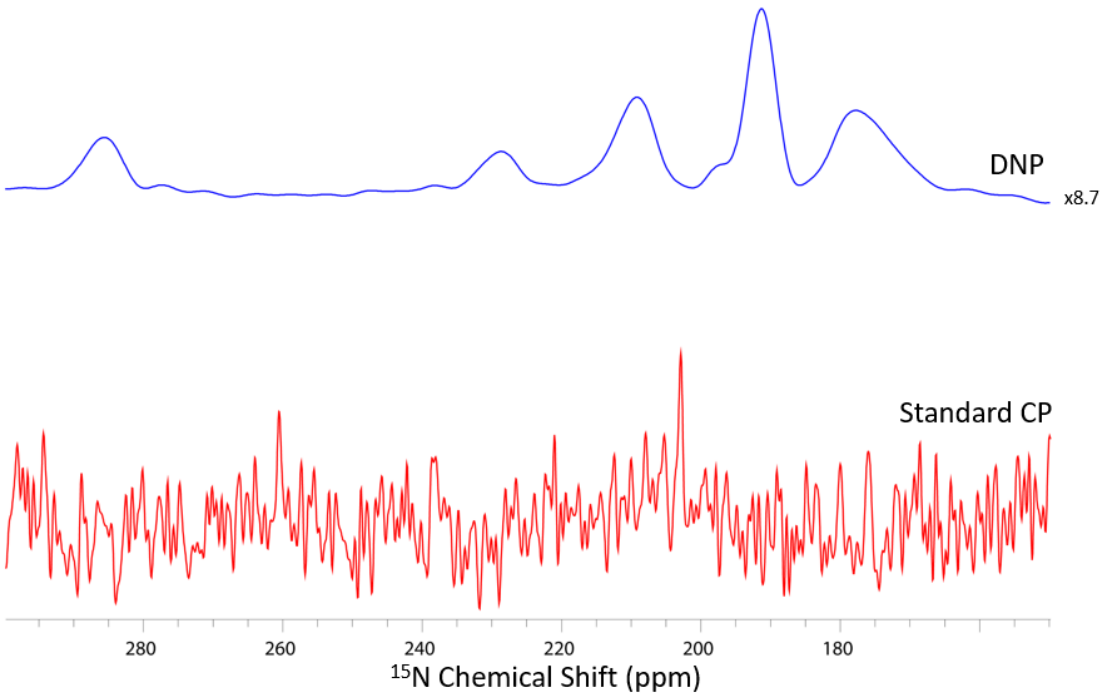

Figure 3.15: Comparison of DNP and standard CP ^{15}N spectra of propyl urea tethered SBA-15.

Figure 3.15 shows the absolute enhancement of the ^{15}N spectrum. With standard CP, there is no usable signal after 5 days of signal averaging. With DNP, there are clear distinct signals after 12 hours of signal averaging. This enhanement of the low abundance ^{15}N nuclei highlights how DNP is a necessary technique for this study.

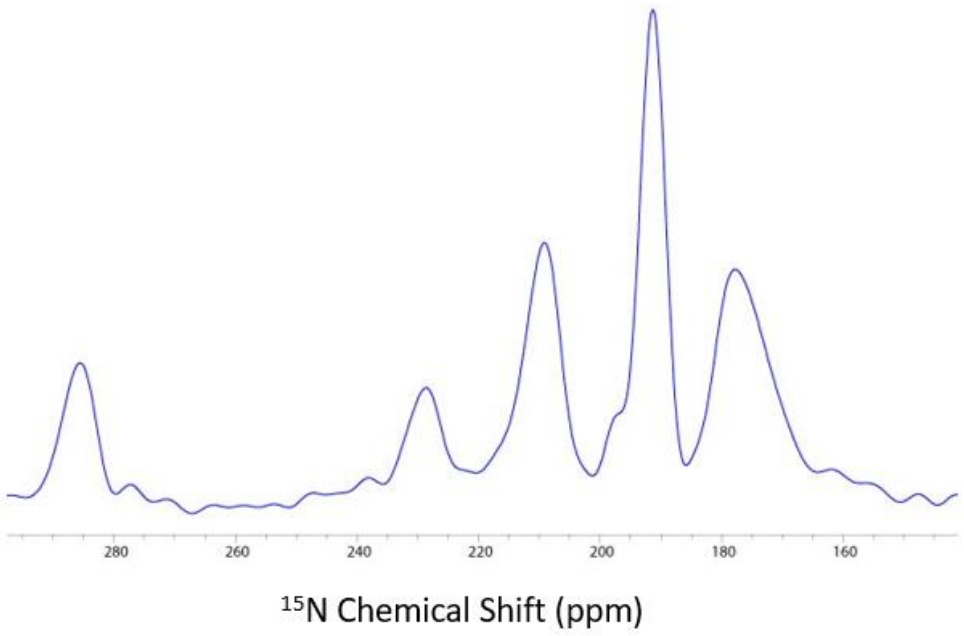

Figure 3.16: ^{15}N DNP spectrum of propyl urea tethered SBA-15.

Zooming in on the ^{15}N DNP spectrum of SBA-15 (figure 3.16), there are 5 signals corresponding to 4 nitrogen sites. This indicates a distribution of sites owing to possible hydrogen exhange. The signal at 285 ppm corresponds to the deprotonated Nitrogen in the pyrimidine ring next to the carbonyl. The signal at 230 ppm could correspond to a protonated Nitrogen in the pyrimidine ring, either at the other position or the same one as next to the carbonyl. The signal at 210 could correspond to the protonated Nitrogen in the pyrimidine, while the other two signals correspond to the urea Nitrogen. More work must be conducted to determine the correct nature of the potential exchange taking place.

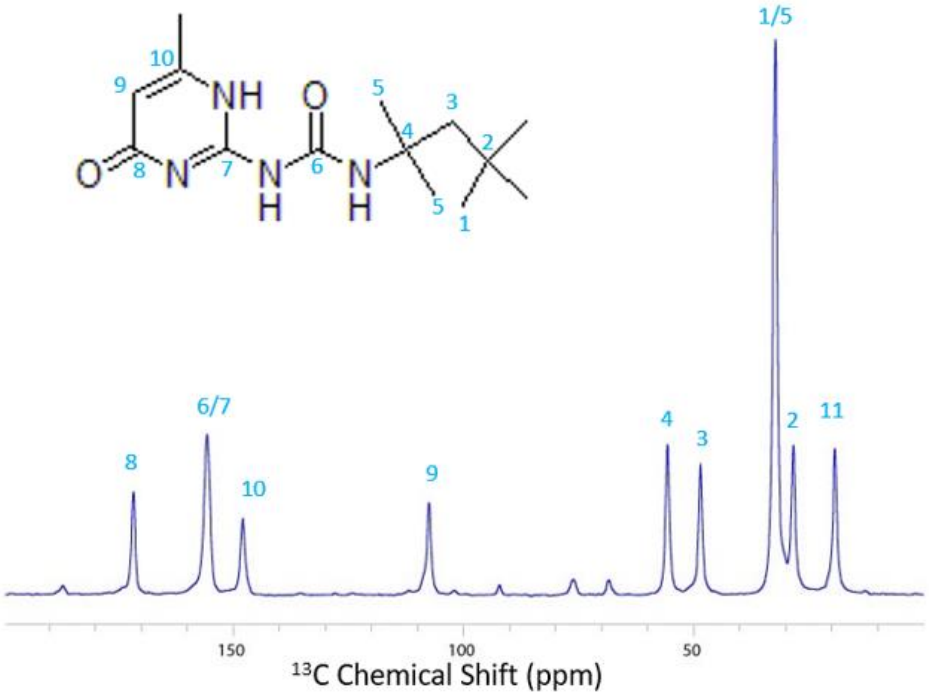

Figure 3.17: ^{13}C CP spectrum of iso-octyl upy

Figure 3.17 shows the ^{13}C CP spectrum of iso-octyl upy along with its structure and labels of the chemical shifts. There are distinct signals that will help distinguish it from the propyl urea tether. In particular, the methyl signals at 33 ppm should be distinct in a spectrum of the paired sample. In Figure 3.18, after the pair is added, the ^{13}C CP spectrum shows additional signals compared to the unpaired sample at 173 ppm, 100 ppm, 50 ppm, 45 ppm, 30 ppm, and 20 ppm. These additional signals indicates the appearance of the iso-octyl upy into the sample. However, its position cannot be confirmed without further experiments.

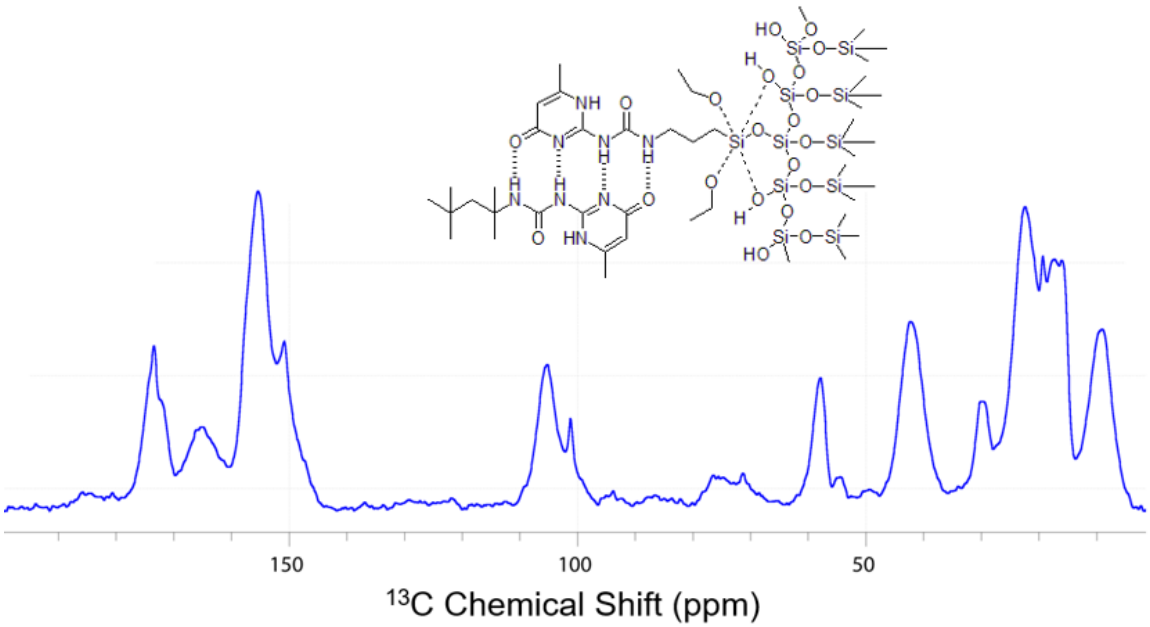

Figure 3.18: ^{13}C CP spectrum of propyl urea SBA-15 paired with iso-octyl upy.

3.4 Conclusions and Future Work

The enhancement provided by DNP, particularly in ^{15}N, has been shown to be essential for probing the surface sites of SBA-15. These enhancements will eventually allow us to probe non-covalent connectivities. The distribution of Q and T sites shows that not all surface sites are occupied by the propyl urea tether and that there is a variety of bonding from the tether to the surface, owing to the distribution of ethoxy leaving groups remaining on the tethered sample. This is confirmed by both ^{13}C and ^{29}Si DNP spectra.

The additional signal present in figure 3.18 indicates the presence of the paired molecule in the sample, but not necessarily at the surface or H-bonded in the way we would expect. In order to conduct 2-dimensional experiments that would reveal the location of the pair, we would need as much signal as possible so we need the increase its concentration. A successful pair should have dramatic effects on the nitrogen chemical shifts, but we need DNP experiments to see those shifts, so the precesnce of the pair must be confirmed first.

A variety of 2-dimensional experiments can be conducted on our sample to confirm the nitrogen chemical shifts, determine the distribution of tethering sites, and determine the distance between the surface and the tether. A ^{1}H-^{15}N HSQC experiment would measure correlation over a single bond and give signal where there is hydrogen bonded directly to nitrogen.[41,42] This typically insensitive experiment would become possible with DNP. This would allow us to assign the nitrogen signals in figure 3.16 and compare paired and unpaired sample.

The distribution of tethering sites according to the ^{29}Si and ^{13}C spectra is something worth exploring further since it was an unexpected development. It would allow us to better understand the interface between the tethered material and the surface. A ^{29}Si-^{29}Si refocused INADEQUATE experiment for homonuclear through bond correlations can produce signal seperating the different ^{29}Si sites by their correlation to other ^{29}Si sites.[5,39] The signal in this experiment only corresponds to through-bond connectivities.

To get an idea of the distance between the tether and the surface, structural constraints can be obtained from ^{13}C-^{15}N and ^{29}Si-^{15}N REDOR experiments.[5,43-45] Signal intensity as a function of ^{15}N recoupling time is characteristic of the distance between two spin pairs. These constraints can be used to calculate the distance between the propyl urea tether and the SBA-15 surface.

It is worth mentioning that ^{13}C spectra were also obtained using 16 mM AMUPOL in 90/10 D_2O/H_2O as the radical/solvent combination (figure 3.19). It gave enhancement of around 16, smaller than the enhancement achieved with TEKPOL in TCE. However, since water has no carbons, there is no solvent peak to interfere with other signals. Additionally, this spectra was obtained on tethered SBA-15 that was not passivated with TMS-d9. This radical/solvent combination may be useful in future experiments.

Constraints and chemical shifts are valuable contributions to future density functional theory (DFT) geometry optimizations. Optimizations can be used to produce three-dimensional structures and chemical shift calculations that can be checked against experimental chemical shifts to confirm the correct structure.[5,46]

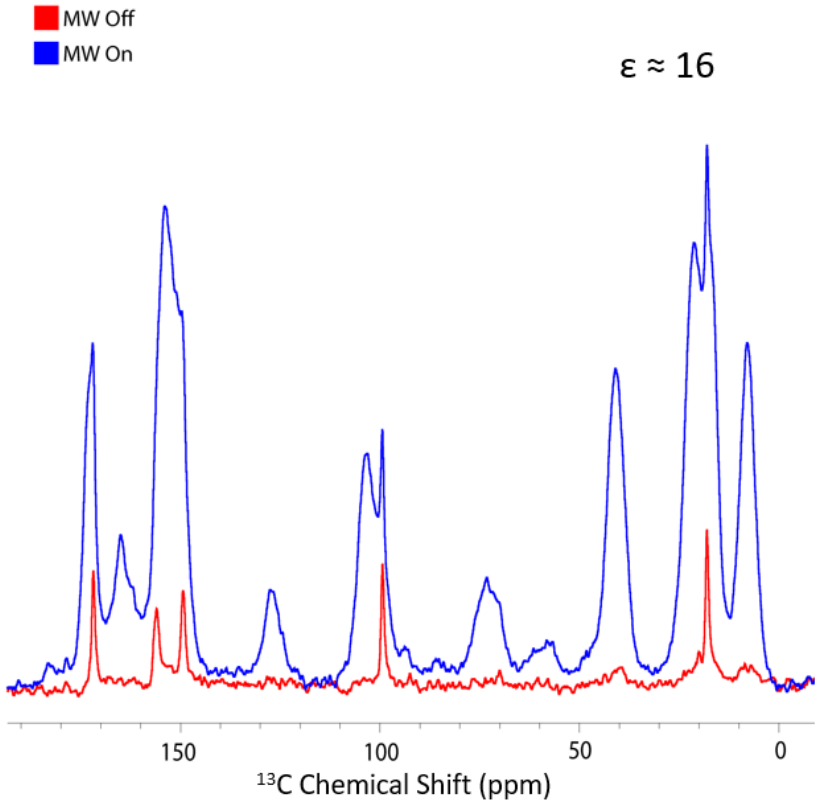

Figure 3.19: ^{13}C DNP spectrum of propyl urea tethered SBA-15 using 16 mM of AMUPOL in 90/10 D_2O/H_2O

3.5 References

(1) Becerra, L. R.; Gerfen, G. J.; Temkin, R. J.; Singel, D. J.; Griffin, R. G. Dynamic nuclear polarization with a cyclotron resonance maser at 5 T. *Physical Review Letters* **1993**, *71*, 3561-3564.

(2) Hall, D. A.; Maus, D. C.; Gerfen, G. J.; Inati, S. J.; Becerra, L. R.; Dahlquist, F. W.; Griffin, R. G. Polarization-enhanced NMR spectroscopy of biomolecules in frozen solution. *Science (New York, N.Y.)* **1997**, *276*, 930-932.

(3) Rosay, M.; Tometich, L.; Pawsey, S.; Bader, R.; Schauwecker, R.; Blank, M.; Borchard, P. M.; Cauffman, S. R.; Felch, K. L.; Weber, R. T.; Temkin, R. J.; Griffin, R. G.; Maas, W. E. Solid-state dynamic nuclear polarization at 263 GHz: spectrometer design and experimental results. *Physical Chemistry Chemical Physics* **2010**, *12*, 5850-5860.

(4) Rossini, A. J.; Zagdoun, A.; Lelli, M.; Lesage, A.; Copéret, C.; Emsley, L. Dynamic Nuclear Polarization Surface Enhanced NMR Spectroscopy. *Accounts of Chemical Research* **2013**, *46*, 1942-1951.

(5) Berruyer, P.; Lelli, M.; Conley, M. P.; Silverio, D. L.; Widdifield, C. M.; Siddiqi, G.; Gajan, D.; Lesage, A.; Copéret, C.; Emsley, L. Three-Dimensional Structure Determination of Surface Sites. *Journal of the American Chemical Society* **2017**, *139*, 849-855.

(6) Lesage, A.; Lelli, M.; Gajan, D.; Caporini, M. A.; Vitzthum, V.; Miéville, P.; Alauzun, J.; Roussey, A.; Thieuleux, C.; Mehdi, A.; Bodenhausen, G.; Coperet, C.; Emsley, L. Surface Enhanced NMR Spectroscopy by Dynamic Nuclear Polarization. *Journal of the American Chemical Society* **2010**, *132*, 15459-15461.

(7) Pump, E.; Bendjeriou-Sedjerari, A.; Viger-Gravel, J.; Gajan, D.; Scotto, B.; Samantaray, M. K.; Abou-Hamad, E.; Gurinov, A.; Almaksoud, W.; Cao, Z.; Lesage, A.; Cavallo, L.; Emsley, L.; Basset, J.-M. Predicting the DNP-SENS efficiency in reactive heterogeneous catalysts from hydrophilicity. *Chemical Science* **2018**, *9*, 4866-4872.

(8) Pump, E.; Viger-Gravel, J.; Abou-Hamad, E.; Samantaray, M. K.; Hamzaoui, B.; Gurinov, A.; Anjum, D. H.; Gajan, D.; Lesage, A.; Bendjeriou-Sedjerari, A.; Emsley, L.; Basset, J.-M. Reactive surface organometallic complexes observed using dynamic nuclear polarization surface enhanced NMR spectroscopy. *Chemical Science* **2017**, *8*, 284-290.

(9) Smith, A. N.; Long, J. R. Dynamic Nuclear Polarization as an Enabling Technology for Solid State Nuclear Magnetic Resonance Spectroscopy. *Analytical Chemistry* **2016**, *88*, 122-132.

(10) Zhao, D.; Huo, Q.; Feng, J.; Chmelka, B. F.; Stucky, G. D. Nonionic Triblock and Star Diblock Copolymer and Oligomeric Surfactant Syntheses of Highly Ordered, Hydrothermally Stable, Mesoporous Silica Structures. *Journal of the American Chemical Society* **1998**, *120*, 6024-6036.

(11) Kruk, M.; Jaroniec, M.; Ko, C. H.; Ryoo, R. Characterization of the Porous Structure of SBA-15. *Chemistry of Materials* **2000**, *12*, 1961-1968.

(12) Westcott, S. L.; Oldenburg, S. J.; Lee, T. R.; Halas, N. J. Formation and Adsorption of Clusters of Gold Nanoparticles onto Functionalized Silica Nanoparticle Surfaces. *Langmuir* **1998**, *14*, 5396-5401.

(13) Fathi Vavsari, V.; Mohammadi Ziarani, G.; Badiei, A. The role of SBA-15 in drug delivery. *RSC Advances* **2015**, *5*, 91686-91707.

(14) Lee, A. F.; Bennett, J. A.; Manayil, J. C.; Wilson, K. Heterogeneous catalysis for sustainable biodiesel production via esterification and transesterification. *Chemical Society Reviews* **2014**, *43*, 7887-7916.

(15) Norhasyimi, R.; Ahmad Zuhairi, A.; Abdullah Rahman, M. A Review: Mesoporous Santa Barbara Amorphous-15, Types, Synthesis and Its Applications towards Biorefinery Production. *American Journal of Applied Sciences* **2010**, *7*.

(16) Verma, P.; Kuwahara, Y.; Mori, K.; Raja, R.; Yamashita, H. Functionalized mesoporous SBA-15 silica: recent trends and catalytic applications. *Nanoscale* **2020**, *12*, 11333-11363.

(17) Alessi, A.; Agnello, S.; Buscarino, G.; Gelardi, F. M. Structural properties of core and surface of silica nanoparticles investigated by Raman spectroscopy. *Journal of Raman Spectroscopy* **2013**, *44*, 810-816.

(18) Barnes, A. B.; Mak-Jurkauskas, M. L.; Matsuki, Y.; Bajaj, V. S.; van der Wel, P. C. A.; DeRocher, R.; Bryant, J.; Sirigiri, J. R.; Temkin, R. J.; Lugtenburg, J.; Herzfeld, J.; Griffin, R. G. Cryogenic sample exchange NMR probe for magic angle spinning dynamic nuclear polarization. *Journal of Magnetic Resonance* **2009**, *198*, 261-270.

(19) Rosay, M.; Blank, M.; Engelke, F. Instrumentation for solid-state dynamic nuclear polarization with magic angle spinning NMR. *Journal of Magnetic Resonance* **2016**, *264*, 88-98.

(20) Morcombe, C. R.; Zilm, K. W. Chemical shift referencing in MAS solid state NMR. *Journal of Magnetic Resonance* **2003**, *162*, 479-486.

(21) Hu, K.-N.; Debelouchina, G. T.; Smith, A. A.; Griffin, R. G. Quantum mechanical theory of dynamic nuclear polarization in solid dielectrics. *The Journal of Chemical Physics* **2011**, *134*, 125105.

(22) Maly, T.; Debelouchina, G. T.; Bajaj, V. S.; Hu, K.-N.; Joo, C.-G.; Mak–Jurkauskas, M. L.; Sirigiri, J. R.; Wel, P. C. A. v. d.; Herzfeld, J.; Temkin, R. J.; Griffin, R. G. Dynamic nuclear polarization at high magnetic fields. *The Journal of Chemical Physics* **2008**, *128*, 052211.

(23) Can, T. V.; Ni, Q. Z.; Griffin, R. G. Mechanisms of dynamic nuclear polarization in insulating solids. *Journal of Magnetic Resonance* **2015**, *253*, 23-35.

(24) Corzilius, B.; Andreas, L. B.; Smith, A. A.; Ni, Q. Z.; Griffin, R. G. Paramagnet induced signal quenching in MAS-DNP experiments in frozen homogeneous solutions. *J Magn Reson* **2014**, *240*, 113-123.

(25) Thurber, K. R.; Tycko, R. Theory for cross effect dynamic nuclear polarization under magic-angle spinning in solid state nuclear magnetic resonance: The importance of level crossings. *The Journal of Chemical Physics* **2012**, *137*, 084508.

(26) Song, C.; Hu, K.-N.; Joo, C.-G.; Swager, T. M.; Griffin, R. G. TOTAPOL: A Biradical Polarizing Agent for Dynamic Nuclear Polarization Experiments in Aqueous Media. *Journal of the American Chemical Society* **2006**, *128*, 11385-11390.

(27) Sauvée, C.; Rosay, M.; Casano, G.; Aussenac, F.; Weber, R. T.; Ouari, O.; Tordo, P. Highly Efficient, Water-Soluble Polarizing Agents for Dynamic Nuclear Polarization at High Frequency. *Angewandte Chemie International Edition* **2013**, *52*, 10858-10861.

(28) Michaelis, V. K.; Ong, T.-C.; Kiesewetter, M. K.; Frantz, D. K.; Walish, J. J.; Ravera, E.; Luchinat, C.; Swager, T. M.; Griffin, R. G. Topical Developments in High-Field Dynamic Nuclear Polarization. *Israel Journal of Chemistry* **2014**, *54*, 207-221.

(29) Zagdoun, A.; Rossini, A. J.; Gajan, D.; Bourdolle, A.; Ouari, O.; Rosay, M.; Maas, W. E.; Tordo, P.; Lelli, M.; Emsley, L.; Lesage, A.; Copéret, C. Non-aqueous solvents for DNP surface enhanced NMR spectroscopy. *Chemical Communications* **2012**, *48*, 654-656.

(30) Matsuki, Y.; Maly, T.; Ouari, O.; Karoui, H.; Le Moigne, F.; Rizzato, E.; Lyubenova, S.; Herzfeld, J.; Prisner, T.; Tordo, P.; Griffin, R. G. Dynamic Nuclear Polarization with a Rigid Biradical. *Angewandte Chemie International Edition* **2009**, *48*, 4996-5000.

(31) Zagdoun, A.; Casano, G.; Ouari, O.; Lapadula, G.; Rossini, A. J.; Lelli, M.; Baffert, M.; Gajan, D.; Veyre, L.; Maas, W. E.; Rosay, M.; Weber, R. T.; Thieuleux, C.; Coperet, C.; Lesage, A.; Tordo, P.; Emsley, L. A Slowly Relaxing Rigid Biradical for Efficient Dynamic Nuclear Polarization Surface-Enhanced NMR Spectroscopy: Expeditious Characterization of Functional Group Manipulation in Hybrid Materials. *Journal of the American Chemical Society* **2012**, *134*, 2284-2291.

(32) Zagdoun, A.; Casano, G.; Ouari, O.; Schwarzwälder, M.; Rossini, A. J.; Aussenac, F.; Yulikov, M.; Jeschke, G.; Copéret, C.; Lesage, A.; Tordo, P.; Emsley, L. Large Molecular Weight Nitroxide Biradicals Providing Efficient Dynamic Nuclear Polarization at Temperatures up to 200 K. *Journal of the American Chemical Society* **2013**, *135*, 12790-12797.

(33) Haukka, S.; Lakomaa, E. L.; Suntola, T.: Adsorption controlled preparation of heterogeneous catalysts. In *Studies in Surface Science and Catalysis*; Dąbrowski, A., Ed.; Elsevier, 1999; Vol. 120; pp 715-750.

(34) Le, D.; Ziarelli, F.; Phan, T. N. T.; Mollica, G.; Thureau, P.; Aussenac, F.; Ouari, O.; Gigmes, D.; Tordo, P.; Viel, S. Up to 100% Improvement in Dynamic Nuclear Polarization Solid-State NMR Sensitivity Enhancement of Polymers by Removing Oxygen. *Macromolecular Rapid Communications* **2015**, *36*, 1416-1421.

(35) Kubicki, D. J.; Rossini, A. J.; Purea, A.; Zagdoun, A.; Ouari, O.; Tordo, P.; Engelke, F.; Lesage, A.; Emsley, L. Amplifying Dynamic Nuclear Polarization of Frozen Solutions by Incorporating Dielectric Particles. *Journal of the American Chemical Society* **2014**, *136*, 15711-15718.

(36) Lim, M. H.; Stein, A. Comparative Studies of Grafting and Direct Syntheses of Inorganic−Organic Hybrid Mesoporous Materials. *Chemistry of Materials* **1999**, *11*, 3285-3295.

(37) Zagdoun, A.; Rossini, A. J.; Conley, M. P.; Grüning, W. R.; Schwarzwälder, M.; Lelli, M.; Franks, W. T.; Oschkinat, H.; Copéret, C.; Emsley, L.; Lesage, A. Improved Dynamic Nuclear Polarization Surface-Enhanced NMR Spectroscopy through Controlled Incorporation of Deuterated Functional Groups. *Angewandte Chemie International Edition* **2013**, *52*, 1222-1225.

(38) Thurber, K. R.; Yau, W.-M.; Tycko, R. Low-temperature dynamic nuclear polarization at 9.4T with a 30mW microwave source. *Journal of Magnetic Resonance* **2010**, *204*, 303-313.

(39) Lesage, A.; Bardet, M.; Emsley, L. Through-Bond Carbon−Carbon Connectivities in Disordered Solids by NMR. *Journal of the American Chemical Society* **1999**, *121*, 10987-10993.

(40) Engelhardt, G.; Michel, D.: *High-resolution solid-state NMR of silicates and zeolites*; John Wiley and Sons,New York, NY: United States, 1987.

(41) Bodenhausen, G.; Ruben, D. J. Natural abundance nitrogen-15 NMR by enhanced heteronuclear spectroscopy. *Chemical Physics Letters* **1980**, *69*, 185-189.

(42) Lesage, A.; Emsley, L. Through-bond heteronuclear single-quantum correlation spectroscopy in solid-state NMR, and comparison to other through-bond and through-space experiments. *J Magn Reson* **2001**, *148*, 449-454.

(43) Gullion, T.; Schaefer, J. Rotational-echo double-resonance NMR. *Journal of Magnetic Resonance (1969)* **1989**, *81*, 196-200.

(44) Gullion, T.; Schaefer, J.: Detection of Weak Heteronuclear Dipolar Coupling by Rotational-Echo Double-Resonance Nuclear Magnetic Resonance. In *Advances in Magnetic and Optical Resonance*; Warren, W. S., Ed.; Academic Press, 1989; Vol. 13; pp 57-83.

(45) Gullion, T. Introduction to rotational-echo, double-resonance NMR. *Concepts in Magnetic Resonance* **1998**, *10*, 277-289.

(46) Ugliengo, P.; Sodupe, M.; Musso, F.; Bush, I. J.; Orlando, R.; Dovesi, R. Realistic Models of Hydroxylated Amorphous Silica Surfaces and MCM-41 Mesoporous Material

Simulated by Large-scale Periodic B3LYP Calculations. *Advanced Materials* **2008**, *20*, 4579-4583.

Chapter 4 – Temperature Dependent Conformational Changes of Polymers Observed using solid-state NMR and Computational Methods

4.1 Introduction

It is well established that most materials expand upon heating. Typically, when molecules are heated, their motion increases, resulting in the molecules occupying more space and causing thermal expansion. However, existing materials that exhibit negative thermal expansion (NTE) may be desirable for certain applications including fiber optics, electronics, and fuel cells. Currently, many materials that shrink upon heating do not have suitable properties at appropriate temperatures or are chemically and thermally unstable.[1-7] There is a need for systems that undergo a large and knowable NTE at usable temperatures that can also be integrated into devices. Understanding and controlling this thermal expansion could add reliability and prolong the lifetimes of these materials.

Dibenzocycloocta-1,5-diene (DBCOD) is one such thermally sensitive material that undergoes NTE. A monomer of DBCOD can also be covalently linked into polymers for several specific applications that require strong but flexible polymers. To explore this property further, several DBCODs have been developed containing a variety of substituents.[8-11] There are two temperature dependent conformations, twist boat and chair (figure 4.1), that causes this thermal contraction in DBCODs upon heating. Of particular interest are two 2,3,8,9-Tetramethyl-Substituted DBCOD (TM-DBCOD) derivatives: diphenylamine substituted TM-DBCOD (1,10-di-Ph-amide) and diethylamide substituted TM-DBCOD (1,10-di-Et-amide) (figure 4.2).

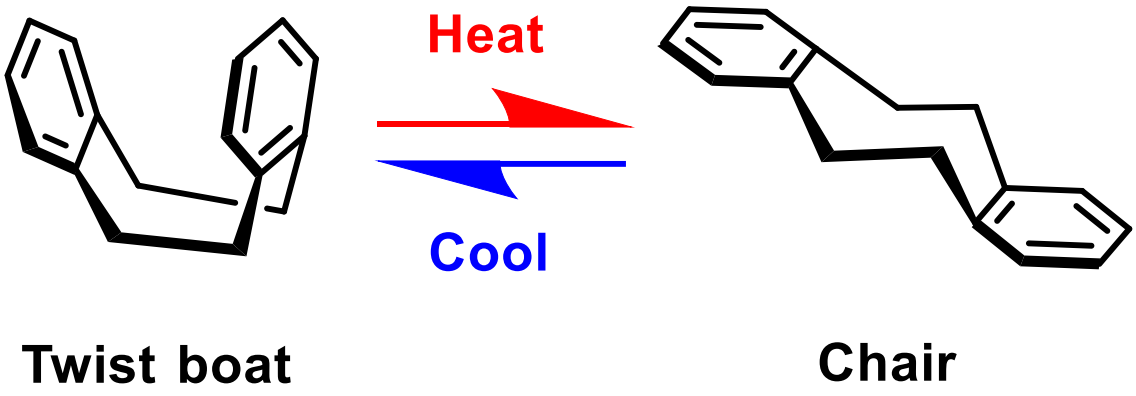

Figure 4.1: The temperature dependent conversion of DBCOD between twist boat and chair conformations

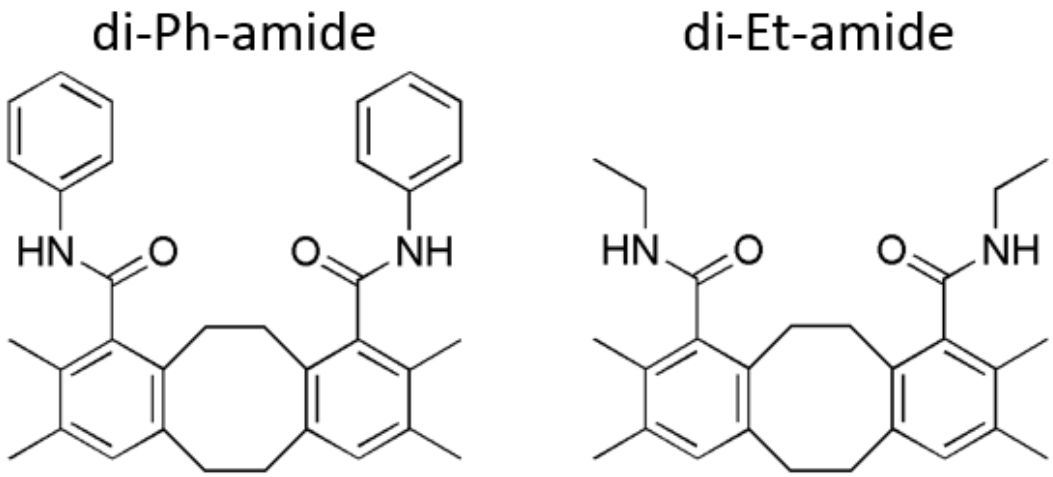

Figure 4.2: Structures of di-Ph-amide and di-Et-amide

Previous variable temperature solution state NMR experiments (Figures 4.3 and 4.4) have shown that at low temperatures, there are distinct chemical shifts for each conformation which averages out to a single chemical shift as the temperature increases. This is due to the fast exchange between the two conformations at high temperatures. The population difference between the two states can be observed as a function of the

temperature, allowing us to find the equilibrium rate constant between the two conformations which can then be used to find the free energy of activation for each conformer.[12-15] This knowledge combined with density functional theory (DFT) chemical shift predictions, thermodynamic information, and structural optimizations can be used to determine the molecular structure of the monomeric DBCOD derivatives which can eventually be applied to knowledge of DBCOD based polymers.[16,17]

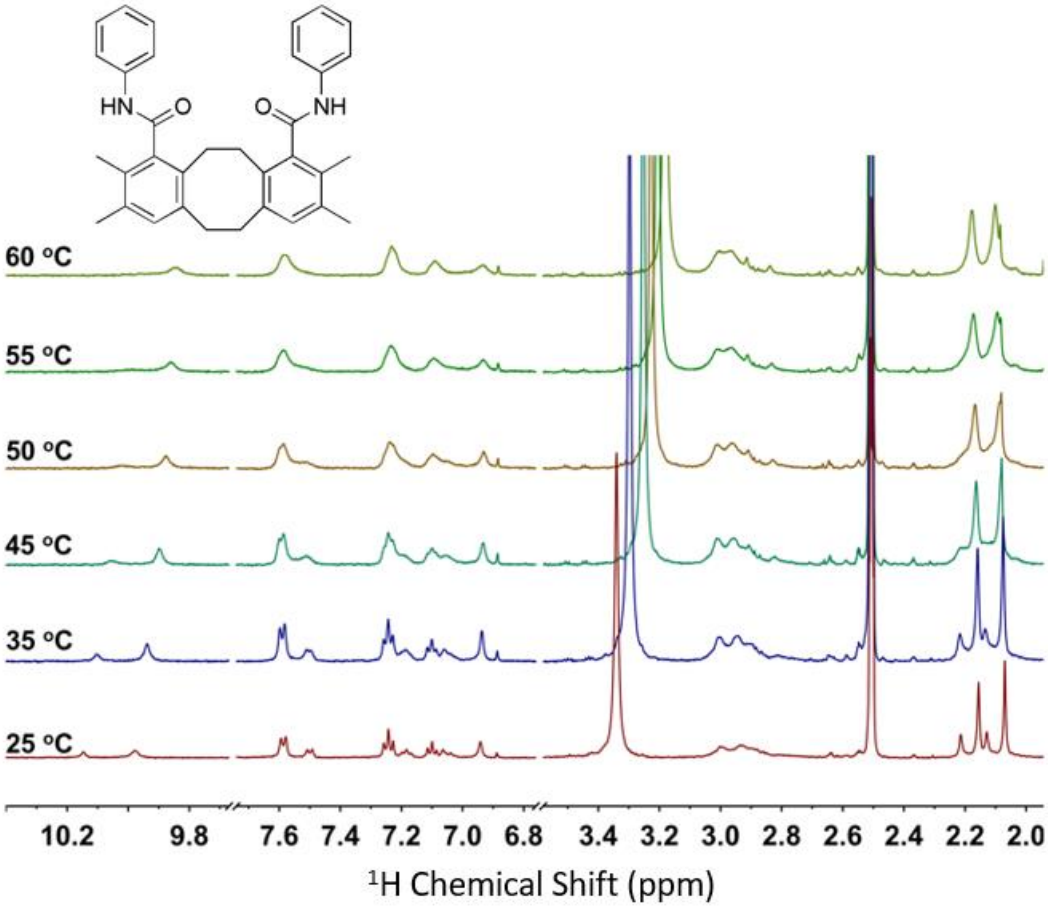

Figure 4.3: Variable-temperature solution-state NMR experiments of di-Ph-amide in DMSO

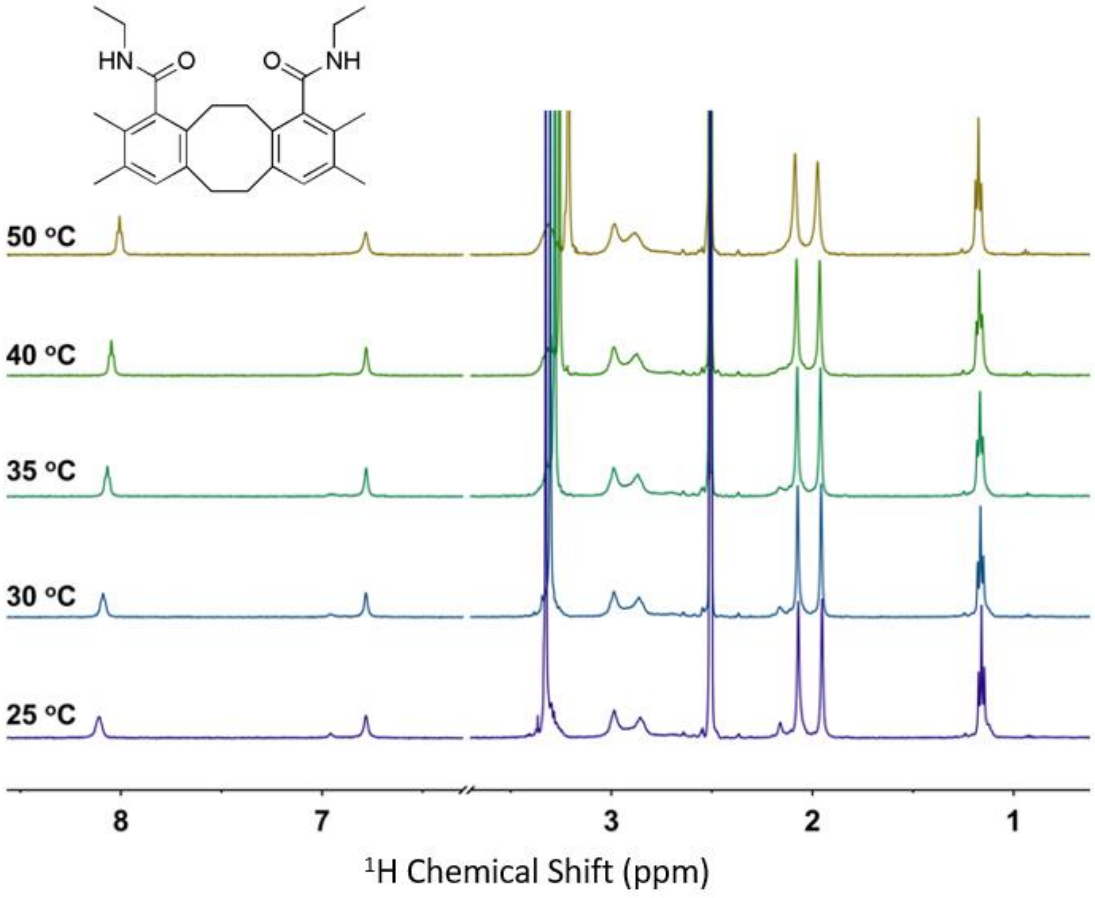

Figure 4.4: Variable-temperature solution-state NMR experiments of di-Et-amide in DMSO

4.2 Experimental Methods

Geometry optimizations were done at the DFT B3LYP level using the 6-31 + g(d,p) basis set with dispersion corrections using Gaussian 09.[18] The structures were obtained both in the gas phase and with the solvent. NMR chemical shifts (δ) were calculated from the isotropic chemical shielding (σ) calculation in Gaussian by performing the following calculations using the 6-311 ++ g(d,p) basis set[19]:

^{13}C: $\delta = \frac{\sigma - 182.73}{-1.0492}$ (Equation 4.1)

^{1}H: $\delta = \frac{\sigma - 31.879}{-1.0338}$ (Equation 4.2)

^{1}H and ^{13}C variable-temperature solution-state, including HSQC and HMBC experiments, were conducted on a Bruker AVII spectrometer with a 11.7 T magnet. Experiments in the solid-state were conducted on a Bruker AVIII spectrometer with a 9.4 T magnet and a 4 mm MAS probe spinning at MAS rates at 8 kHz at temperatures ranging from -15°C to 50°C.

The spin-lattice or longitudinal relaxation, or T_1 relaxation time, of ^{1}H nuclei describes the return to equilibrium in the direction of the magnetic field (the z-direction, in our case). As described in Chapter 1, the direction of the bulk magnetization can be manipulated by applying RF pulses. An inversion-recovery experiment (figure 4.5) can be used to measure this T_1 relaxation time, which is more sensitive to temperature change than the chemical shift, so structural transition can be observed by measuring the T_1 relaxation time at variable-temperatures in addition to observing the chemical shift. In terms of the rotating frame, a 180° x pulse brings the z-magnetization to -z. An immediate 90° x pulse allows us to detect all that signal in the xy-plane and results in a large negative signal after the Fourier transform. The longer the delay τ between the initial 180° x pulse and the subsequent 90° x, the more positive the signal will become after the sequence as more signal can return from -z to z. The delay τ at which this experiment results in maximum

signal corresponds to how long the T_1 relaxation is. The two conformations twist boat and chair are expected to have different T_1 relaxation times.[20,21]

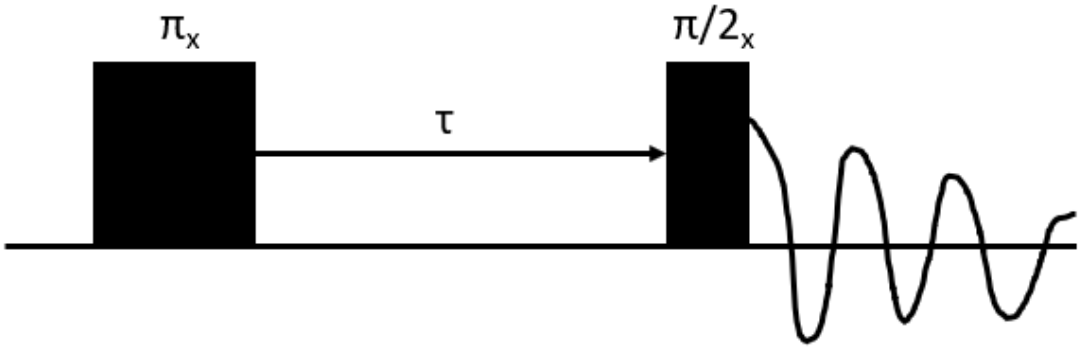

Figure 4.5: The inversion-recovery pulse sequence for measuring T_1 with a variable delay of τ

In addition to standard ^{13}C CP MAS experiments at variable temperature, T_1 relaxation time measurements were conducted with variable delays of 0.001, 0.05, 0.1, 0.2, 0.3, 0.5, 0.8, 1, 1.5, 2, 2.5, 3, 3.5, 4, 4.5, and 5 seconds at temperatures of -15°, -10°, -5°, 0°, 5°, 9.8°, 21°, 30°, 40°, and 50°C.

The progression of the reaction from one state to the other is described by figure 4.6. $\Delta G^{\ddagger}$ is the activation energy of the reaction, or the amount of energy that is required for the reaction to proceed. ΔG is the difference in free energy between the initial and final state of a reaction. ΔG can be determined by:

$$\Delta G = -RT\, ln\, K_{eq} \qquad \text{(Equation 4.3)}$$

where

$$K_{eq} = \frac{[Chair]}{[Twist\ Boat]} \qquad \text{(Equation 4.4)}$$

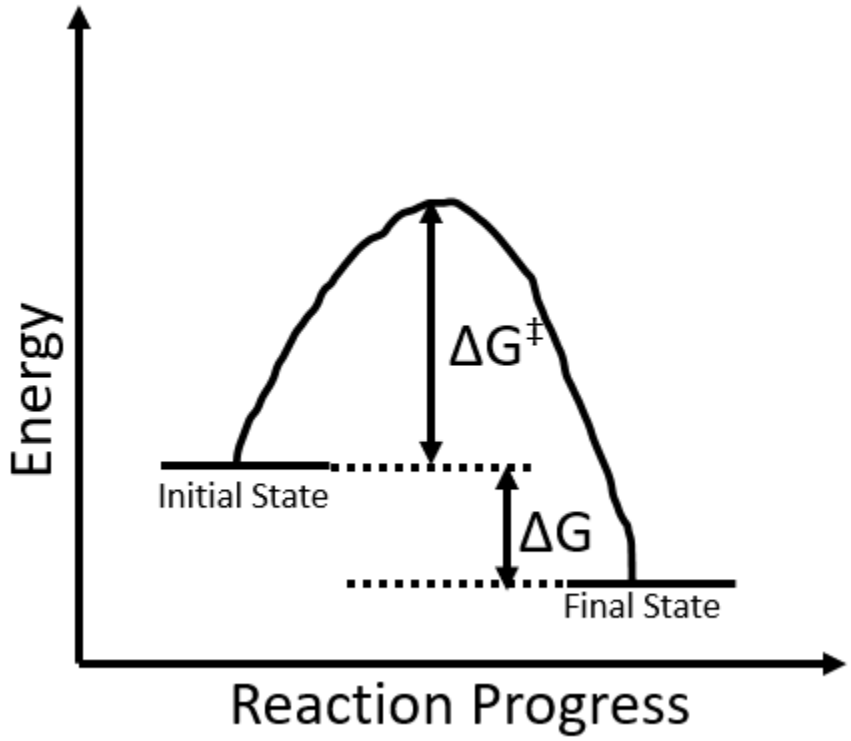

Figure 4.6: The plot of Energy vs Reaction Progress from the initial state of a reaction to its final state

In the VT solution-state spectra, a chemical shift range is picked which shows clear exchange (for example, the 6-7 ppm range was used for di-Et-amide). That range is then fit to a Lorentzian lineshape at each temperature in Mathematica.[22] The fit values of the rate constants K_{ab} and K_{ba} are plotted as rate vs temperature, then fitted curves are produced which are used to calculate the Gibbs energy of each state.

4.3 Results and Discussion

Assignments for the structure of di-Ph-amide were made using an HSQC experiment where signals arise over a single hydrogen-carbon bond (figure 4.7). Separate assignments were made to the chemical shifts on the 8-member ring and the methyl groups. With the assignments made in solution, we can confidently make assignments in the solid-state where we want to observe the behavior of the monomers and polymers (Figure 4.8).

Figure 4.7: HSQC of di-Ph-amide in DMSO with assignments

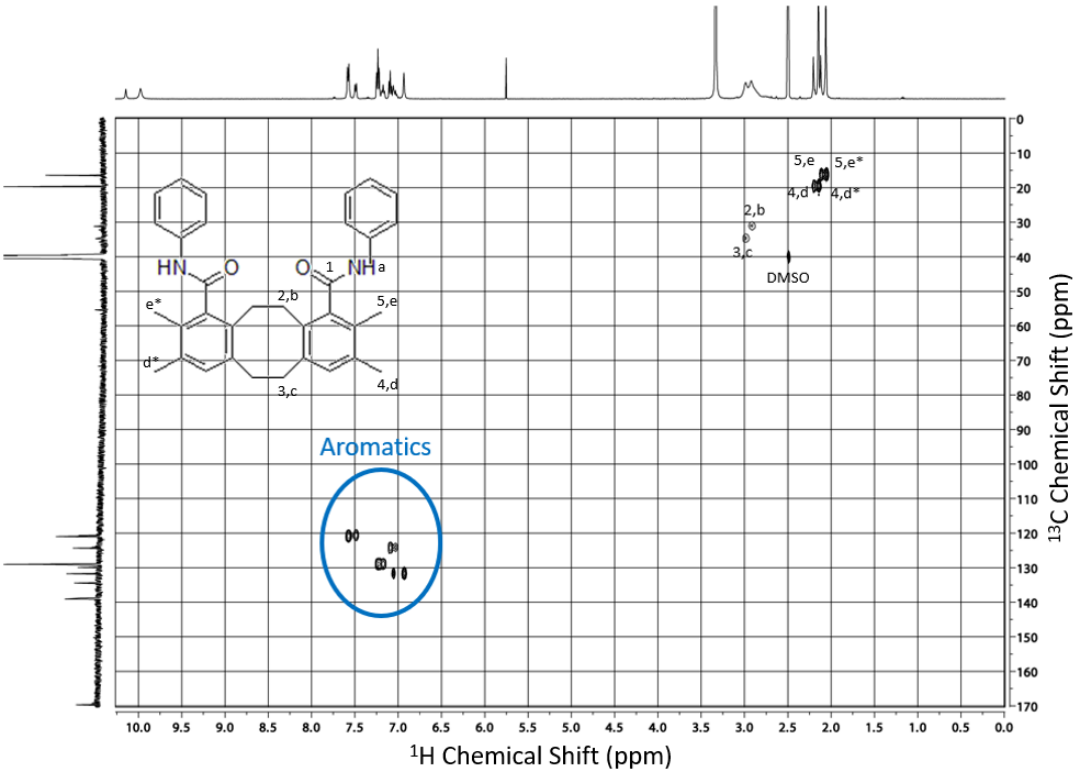

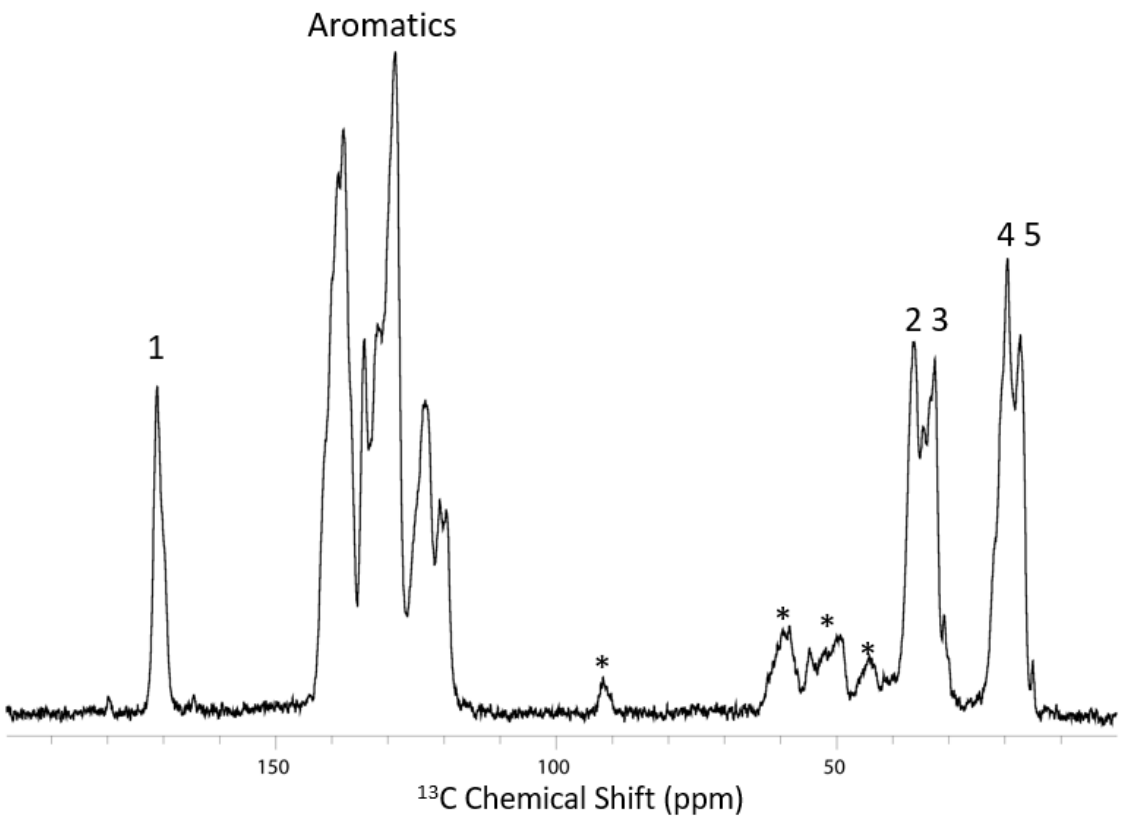

Figure 4.8: ^{13}C CP ssNMR spectrum of di-Ph-amide.

Chemical shift assignments alone are not enough to confirm which conformation is preferred in the solid-state. Gaussian chemical shift predictions were used to generate predicted spectra that were compared to the experimental spectra.

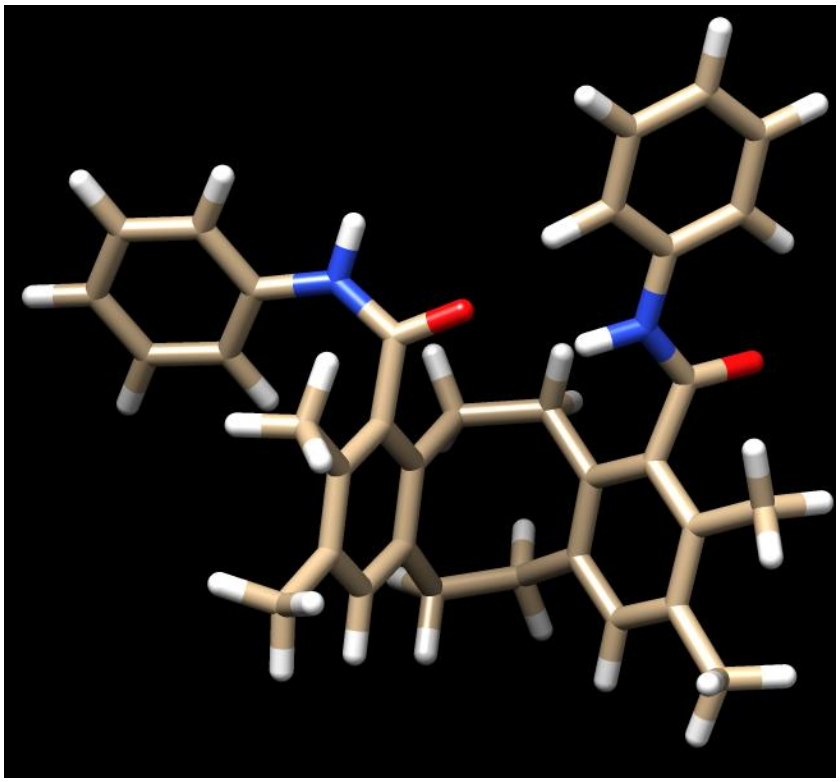

Figure 4.9: The optimized twist boat structure of di-Ph-amide

Starting at a variety of positions, the optimized lowest energy twist boat conformation (figure 4.9) has the two carbonyl groups pointed in opposite directions. The hydrogen of the amide and the oxygen of the carbonyl on the opposite side are notably close to each other in the structure and the distance between them is only 2 Å, indicating that there is intramolecular hydrogen-bonding contributing to the favorability of this structure.[23] When the ^{13}C chemical shifts generated in Gaussian from this structure are fit to a Lorentzian lineshape and overlayed with the actual spectrum (Figure 4.10) in Mathematica, we can compare the predicted shifts (in blue) and the experimentally obtained chemical shifts (in black). The twist boat conformation gives rise to two distinct chemical shifts at the carbonyl position (~170 ppm), while the real spectrum shows only

one. However, the signals from the 8-member ring (~30-40 ppm) and the methyls (~20 ppm) overlap almost exactly.

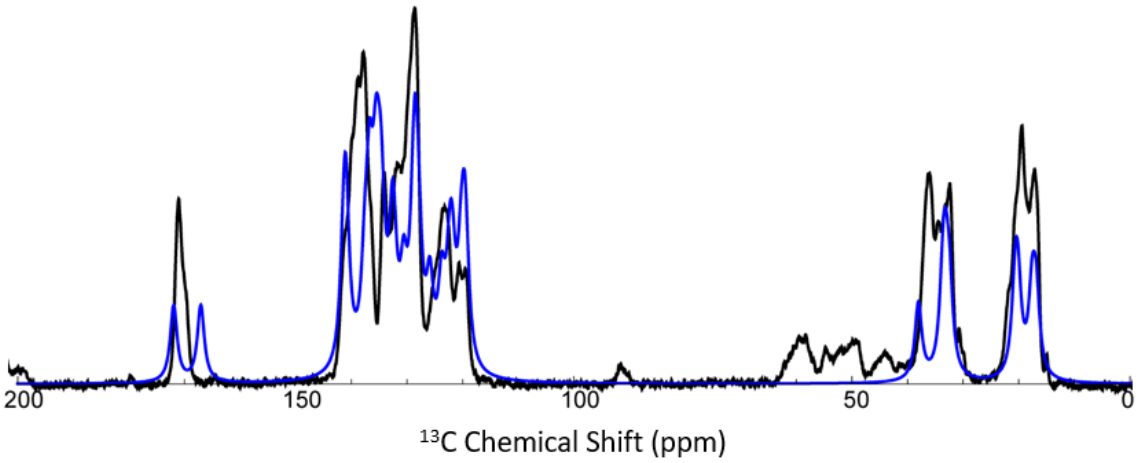

Figure 4.10: Predicted ^{13}C spectrum of the optimized twist boat structure of di-Ph-amide obtained in Gaussian (blue) overlayed with the experimental ^{13}C CP ssNMR (black)

A similar comparison can be made by generating the Gaussian structure of the chair conformation and comparing the chemical shifts of that structure to the experimentally obtained chemical shifts.

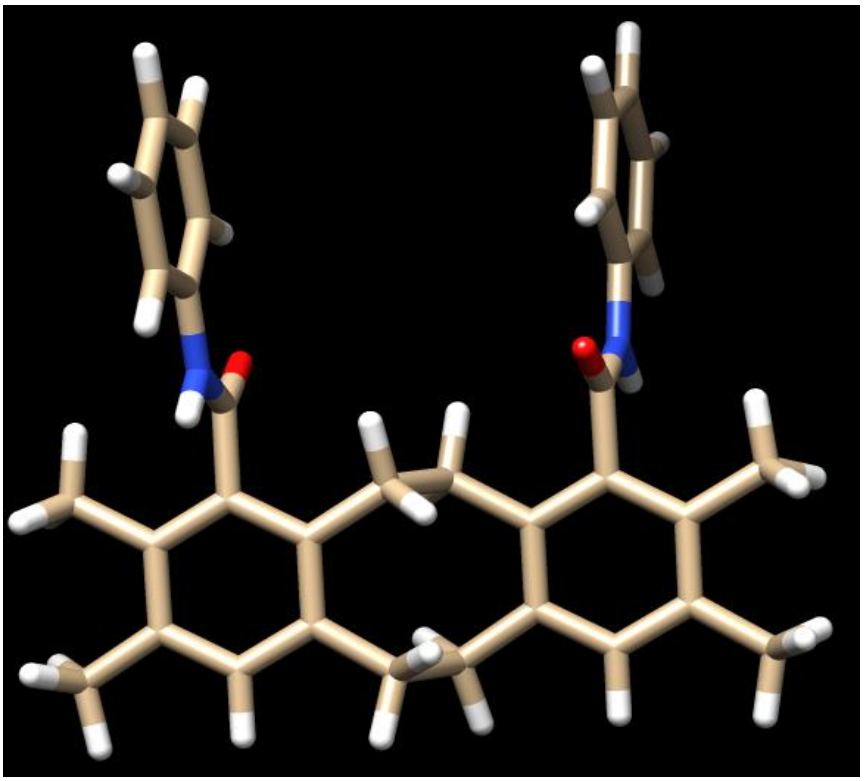

Figure 4.11: The optimized chair structure of di-Ph-amide

Like the twist boat structure, the chair structure (figure 4.11) features the two carbonyl groups pointing in opposite directions. However, the distance from the hydrogen of the amide to the oxygen of the carbonyl on the opposite side is over 6 Å, ruling out the possibility of hydrogen-bonding. The computationally predicted spectrum (in red) overlayed with the experimentally obtained spectrum (in black) (figure 4.12) shows a single carbonyl chemical shift for the computationally obtained spectrum, but further upfield. The signals from the 8-member ring are further downfield than in the experimentally obtained spectrum while the methyl signals overlap exactly.

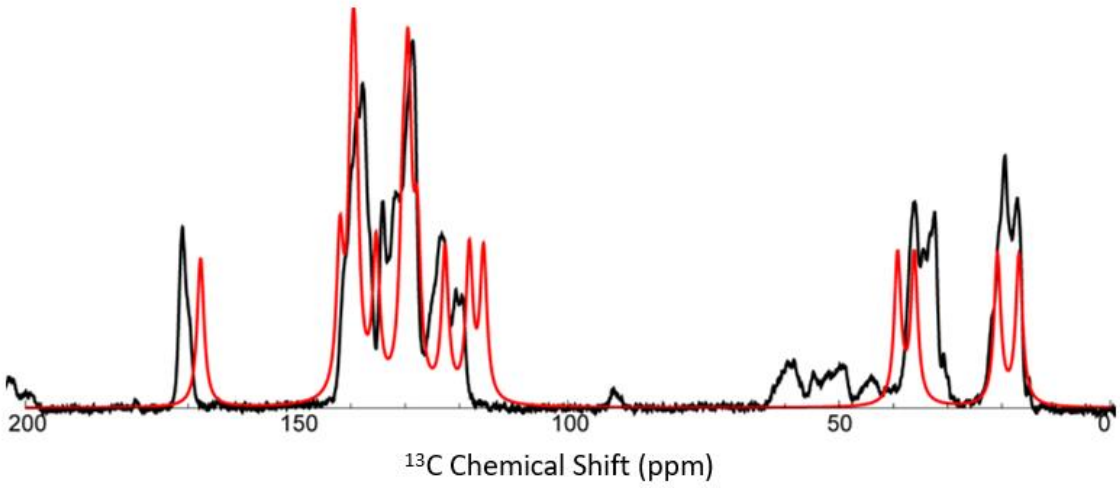

Figure 4.12: Predicted ^{13}C spectrum of the optimized chair structure of di-Ph-amide obtained in Gaussian (red) overlayed with the experimental ^{13}C CP ssNMR (black)

The most noticeable difference in the two spectra generated by the Gaussian structures is for the carbonyl carbon. The twist boat structure results in two carbonyl signals, while the chair results in one. While this seems to favor the chair structure, if both twist boat and chair conformations exist in the solid-state at room temperature, the single carbonyl signal could also be a result of signal averaging between all the possible carbonyl positions. The intramolecular hydrogen bond formed in the twist boat seems to favor it as the preferred structure at room temperature.

The range of 7.4-7.7 ppm in the ^{1}H VT solution-state experiment was selected for the thermodynamic calculations. After fitting the parameters and plotting rate in one direction vs temperature, the Gibbs energy of one state was found to be 16.7 kcal/mol while the other was found to be 16.1 kcal/mol. This gives a ΔG of -0.6 or 0.6 kcal/mol depending on which conformation is more stable.

The simpler di-Et-amide monomer was evaluated using the same methods in the hope the simpler monomer could reveal insight into the more complex di-Ph-amide.

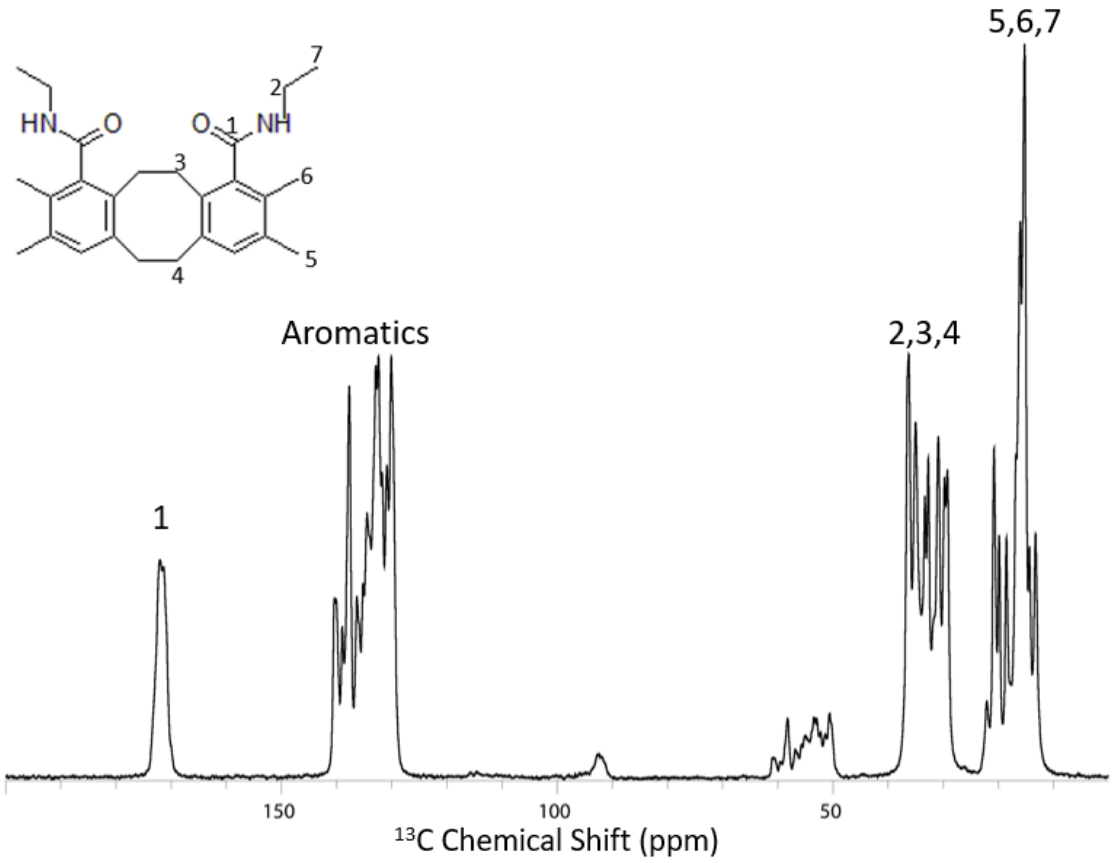

Figure 4.13: ^{13}C CP ssNMR spectrum of di-Et-amide with assignments

The many different signals corresponding to each site indicates there are many more potential orientations in the solid-state existing at once than in the di-Ph-amide monomer. This is due to the flexibility of the ethyl group, which is likely unrelated to the twist boat and chair conformations. Variable-temperature experiments were conducted on di-Et-amide in the solid-state to observe the spectral changes as previously done in the solution-state. However, the lack of temperature dependence on ^{13}C chemical shifts in the

solid state is likely due to the rigidity of the structure as a solid. Carbon chemical shifts are also less sensitive to conformational changes than proton chemical shifts.

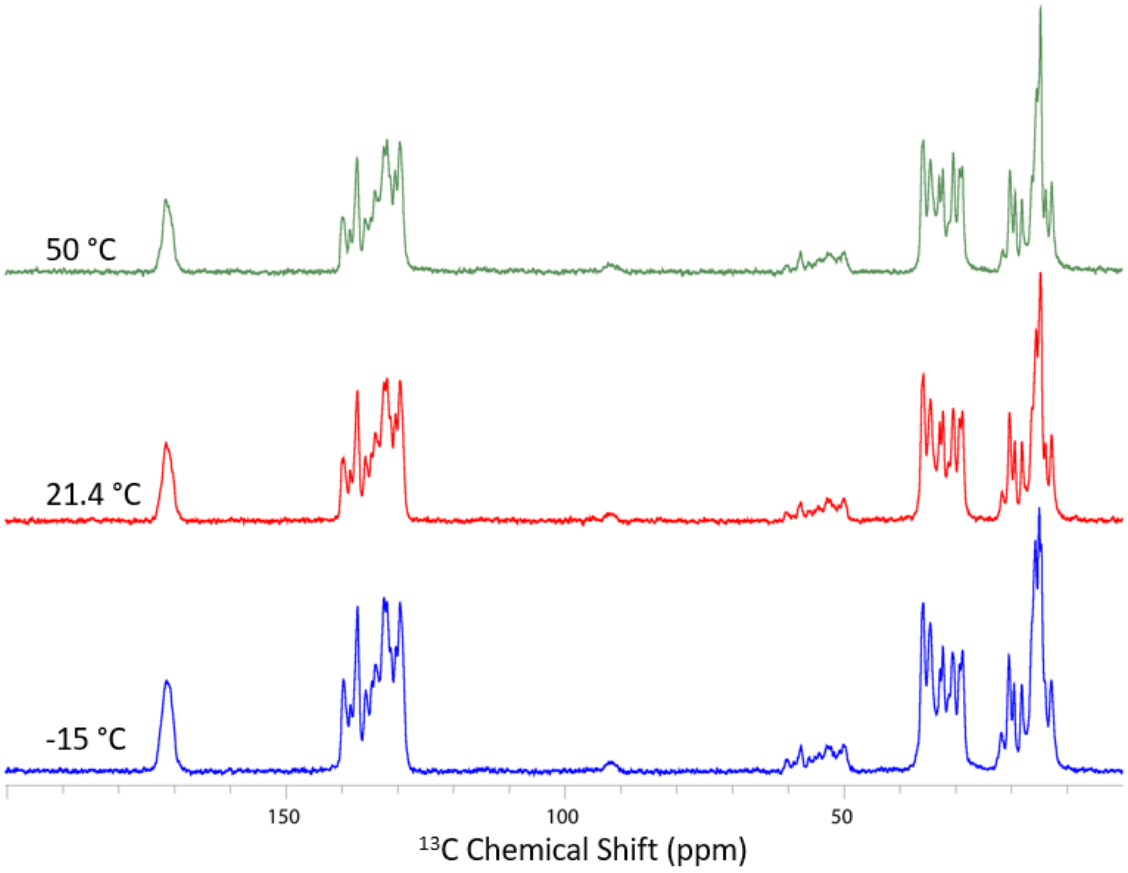

Figure 4.14: ^{13}C ssNMR spectra of di-Et-amide at variable-temperatures

Proton relaxation rates are similarly more sensitive to conformational change than Carbon chemical shifts. A discontinuity in the slope of the graph of T_1 vs the inverse of the temperature would indicate a structural transition and would help identify the temperatures at which the conformation change takes place.[21]

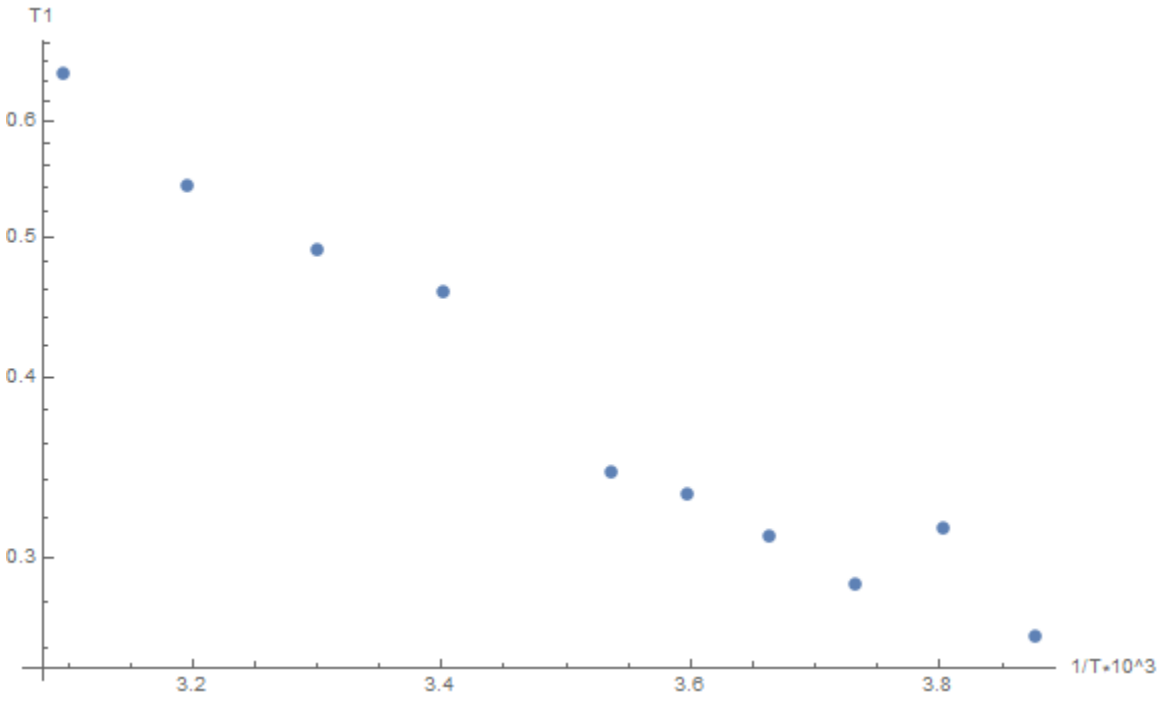

Figure 4.15: T_1 relaxation time vs the inverse of the temperature of di-Et-amide in the solid state

There was no substantial change in dynamics across the temperature range in di-Et-amide. Unfortunately, this experiment is limited by the temperature range available to the probe, which has a lower limit of -15 °C. The transition in the solid-state may happen at a lower temperature than is accessible to us, so we are unable to identify the transition ranges based on this experiment. However, di-Et-amide and di-Ph-amide may be particularly rigid monomers as solids and these experiments may be useful on less rigid monomers and polymers. This relaxation time experiment shows the limitations of looking at rigid polymers in the solid-state. Instead, we can look at optimized structures in solution to compare to experimental ^{1}H chemical shifts.

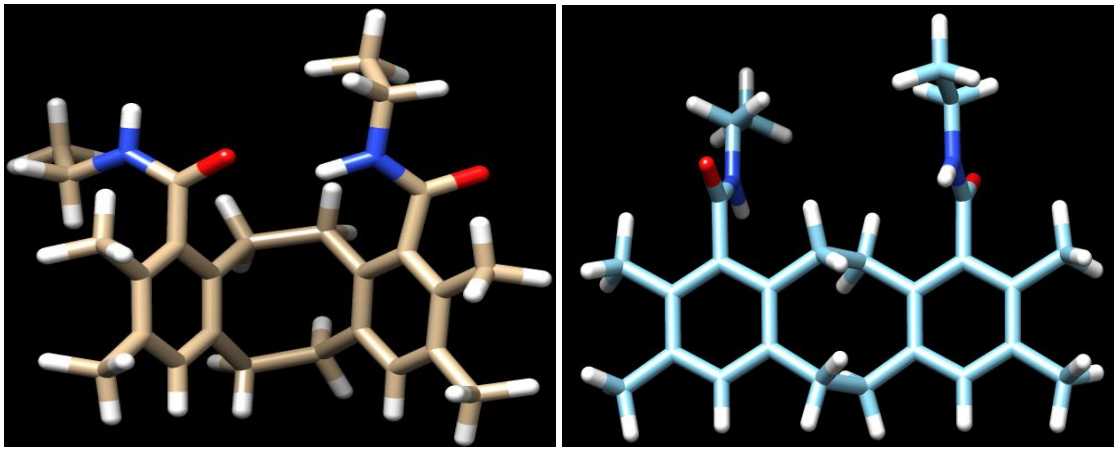

Figure 4.16: Optimized structures for twist boat (left) and chair (right) of di-Et-amide in DMSO

Like the optimized structures of di-Ph-amide, the carbonyl groups of the twist boat indicate hydrogen bonding between the hydrogen of the amide and the oxygen of the carbonyl, which are separated by only 2 Å. The same spots on the chair are too far apart, ruling out hydrogen bonding. The computationally generated ^{1}H spectra can be compared to the di-Et-amide experimental spectra at variable-temperatures.

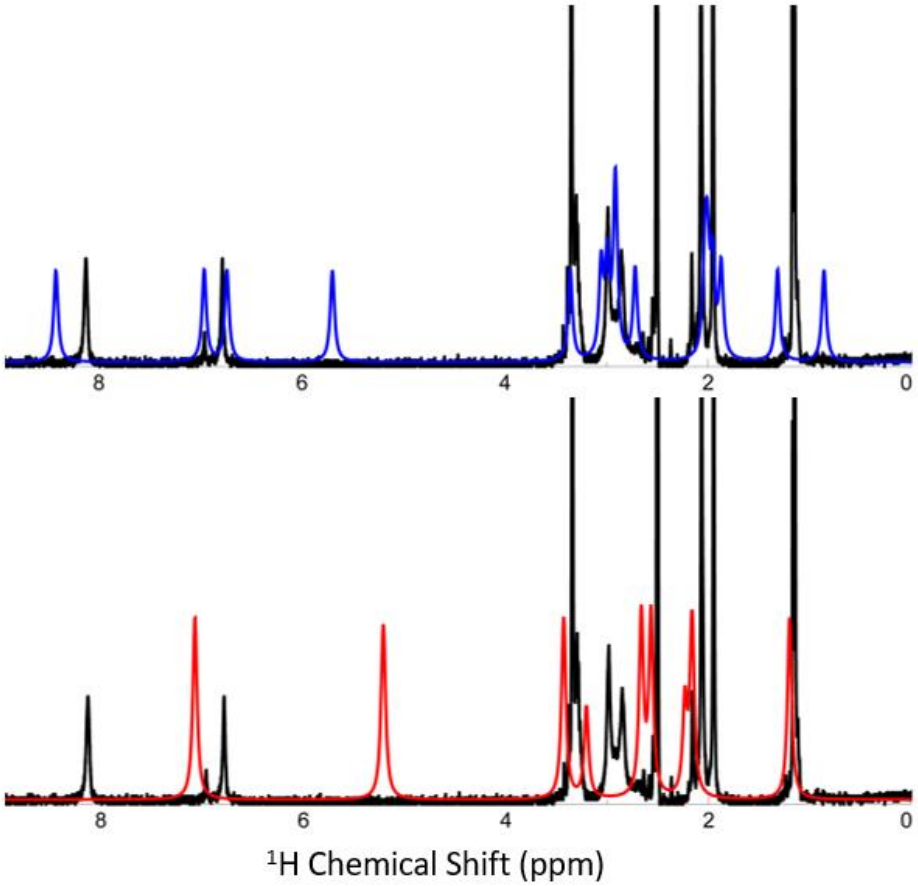

Figure 4.17:[1]H spectral comparisons between the experimental spectrum at 25°C (black) and the predicted spectra of twist boat (blue, top) and chair (red, bottom) of di-Et-amide

Proton chemical shifts generated in Gaussian from chemically equivalent protons according to the HSQC were averaged for this comparison. Looking at room temperature experiments conducted at 25°C against the predicted spectra generated in Gaussian of the twist boat conformation (blue, top) and the chair conformation (red, bottom) of di-Et-amide. The amine proton signal on the real spectrum is around 8 ppm, while it is around 5.2 ppm on the chair. The twist boat amine proton results in two signals at 5.7 ppm and 8.4 ppm. The real signal is likely a result of signal averaging between these states. The aromatic signal around 7 ppm contains two signals for the real spectrum and the twist boat, but only

one for the chair. There is a lot of overlap in the further upfield signals corresponding to the ethyl group and the 8-member ring and they are more difficult to convolute. A more quantitative analysis must be attempted.

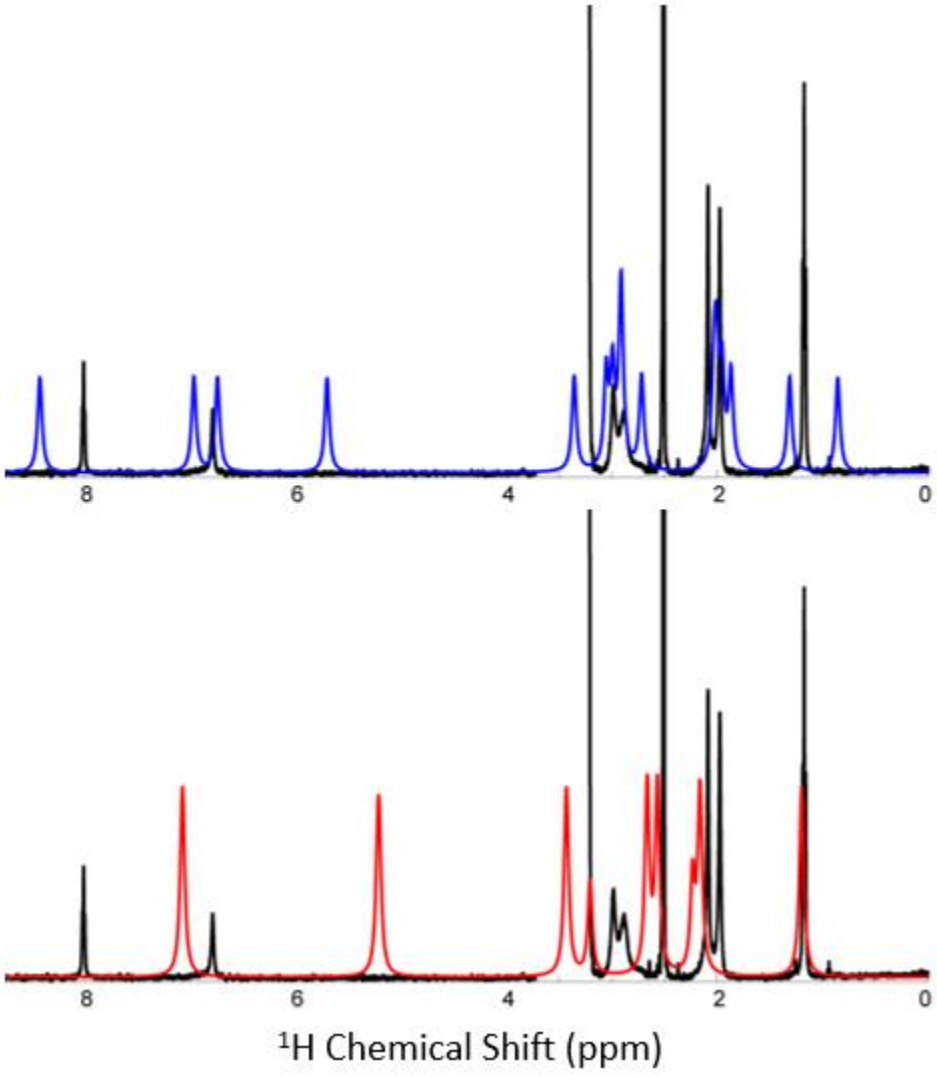

Figure 4.18: ^{1}H Spectral comparisons between the experimental spectrum at 50°C (black) and the predicted spectra of twist boat (blue, top) and chair (red, bottom) of di-Et-amide

In the high temperature experiment conducted at 50°C, the amine proton moves slightly upfield and the aromatic proton signal now only results in one peak around 7 ppm. The results of these comparisons indicate that both structures exist at lower temperatures, then transition to only chair at high temperatures. As with the room temperature comparison, a more quantitative analysis must be attempted.

The range of 6-7 ppm in the ^{1}H VT solution-state experiment was selected for the thermodynamic calculations of di-Et-amide. After fitting the parameters and plotting rate in one direction vs temperature, the Gibbs energy of one state was found to be 16.5 kcal/mol while the other was found to be 15.5 kcal/mol. This gives a ΔG of -1.0 or 1.0 kcal/mol depending on which conformation is more stable.

4.4 Conclusions and Future Work

The results based on the spectra and computational structures point to the boat conformation being preferred at lower temperatures of both the di-Ph-amide and the di-Et-amide monomers. This can be seen by the greater agreement in the chemical shifts and is backed up by the presence of the H-bond in the structures. At moderate temperatures, both conformations exist at some ratio dependent on the temperature. At high temperatures, the structures convert completely to the chair conformation.

To identify the temperature range of the transition in the solid state, a T_1 relaxation time experiment was attempted on the di-Et-amide. However, the experiment was limited by the temperature range of the probe involved in the experiment. A broader range of temperatures is required to identify the transition temperatures. Additionally, proton

spectra can be obtained in the solid state and compared at variable temperatures, like what has been shown in the solution-state experiments. Proton experiments in the solid state require spinning at fast MAS to identify the isotropic chemical shift.[24] Fast MAS VT experiments should be attempted.

Proton chemical shifts in the solid-state combined with chemical shifts in solution can be compared with the predicted chemical shifts based on the optimized Gaussian structures in the gas phase and in solution. Instead of comparing them visually, as we have done, we can quantitatively determine which structure exists at high or low temperatures by an f-test. The f-test on the experimental chemical shifts can identify which model (experimental chemical shifts for each conformation) is more likely at high and low temperatures.

Once the identities of the initial and final states are known, the sign of ΔG can be determined since it is dependent on the natural log of the ratios of the two conformations (equations 4.3 and 4.4). $\Delta G^{\ddagger}$ for the transition and the predicted value ΔG can also be obtained using the optimized Gaussian structures once they agree with the experimental chemical shifts. The experimental value of $\Delta G^{\ddagger}$ can be found using the Eyring equation, in a process similar how we obtained the experimental values of ΔG. Other thermodynamic properties, S, H, $S^{\ddagger}$, and $H^{\ddagger}$ can also be determined.

DBCOD derivatives with different constituents can be observed using the same NMR and computational methods. This can be studied to determine to what extent the conformational change is dependent on intramolecular H-bonding, intermolecular interactions, or the steric hindrance of one of the conformations. In addition to the DBCOD

derivatives, polymers can also be studied that are made up of different, or the same repeating, monomer.

4.5 References

(1) Hua, Y.; Ni, Q.-Q.; Yamanaka, A.; Teramoto, Y.; Natsuki, T. The Development of Composites with Negative Thermal Expansion Properties Using High Performance Fibers. *Advanced Composite Materials* **2011**, *20*, 463-475.

(2) Lind, C. Two Decades of Negative Thermal Expansion Research: Where Do We Stand? *Materials* **2012**, *5*, 1125-1154.

(3) Sleight, A. W. Negative thermal expansion materials. *Current Opinion in Solid State and Materials Science* **1998**, *3*, 128-131.

(4) Chen, J.; Hu, L.; Deng, J.; Xing, X. Negative thermal expansion in functional materials: controllable thermal expansion by chemical modifications. *Chemical Society Reviews* **2015**, *44*, 3522-3567.

(5) Evans, J. O. Negative thermal expansion materials. *Journal of the Chemical Society, Dalton Transactions* **1999**, 3317-3326.

(6) Liu, Z.-K.; Wang, Y.; Shang, S.-L. Origin of negative thermal expansion phenomenon in solids. *Scripta Materialia* **2011**, *65*, 664-667.

(7) Miller, W.; Smith, C. W.; Mackenzie, D. S.; Evans, K. E. Negative thermal expansion: a review. *Journal of Materials Science* **2009**, *44*, 5441-5451.

(8) Uğur, G.; Chang, J.; Xiang, S.; Lin, L.; Lu, J. A Near-Infrared Mechano Responsive Polymer System. *Advanced Materials* **2012**, *24*, 2685-2690.

(9) Shen, X.; Viney, C.; Johnson, E. R.; Wang, C.; Lu, J. Q. Large negative thermal expansion of a polymer driven by a submolecular conformational change. *Nature Chemistry* **2013**, *5*, 1035-1041.

(10) Shen, X.; Connolly, T.; Huang, Y.; Colvin, M.; Wang, C.; Lu, J. Adjusting Local Molecular Environment for Giant Ambient Thermal Contraction. *Macromolecular Rapid Communications* **2016**, *37*, 1904-1911.

(11) Wang, Z.; Huang, Y.; Guo, J.; Li, Z.; Xu, J.; Lu, J. Q.; Wang, C. Design and Synthesis of Thermal Contracting Polymer with Unique Eight-Membered Carbocycle Unit. *Macromolecules* **2018**, *51*, 1377-1385.

(12) Gao, Z.; Molnar, A.; Morin, F. G.; Eisenberg, A. Blends of polyamide-6 and sulfonated polystyrene. A solid-state NMR study. *Macromolecules* **1992**, *25*, 6460-6465.

(13) Campbell, G. C.; VanderHart, D. L. Optimization of chemical-shift-based polarization gradients in 1H NMR spin-diffusion experiments on polymer blends with chemically similar constituents. *Journal of Magnetic Resonance (1969)* **1992**, *96*, 69-93.

(14) Kitayama, T.; Hatada, K.: *NMR spectroscopy of polymers*; Springer Science & Business Media, 2013.

(15) Mathias, L. J.: *Solid state NMR of polymers*; Springer Science & Business Media, 2013.

(16) Mitchell, R. H. Conformational Changes of 2,11-Dithia[3.3]metacyclophane. A New Look Using VT NMR and Calculation. *Journal of the American Chemical Society* **2002**, *124*, 2352-2357.

(17) Witosińska, A.; Musielak, B.; Serda, P.; Owińska, M.; Rys, B. Conformation of Eight-Membered Benzoannulated Lactams by Combined NMR and DFT Studies. *The Journal of Organic Chemistry* **2012**, *77*, 9784-9794.

(18) Frisch, M. J.; Trucks, G. W.; Schlegel, H. B.; Scuseria, G. E.; Robb, M. A.; Cheeseman, J. R.; Scalmani, G.; Barone, V.; Petersson, G. A.; Nakatsuji, H.; Li, X.; Caricato, M.; Marenich, A. V.; Bloino, J.; Janesko, B. G.; Gomperts, R.; Mennucci, B.; Hratchian, H. P.; Ortiz, J. V.; Izmaylov, A. F.; Sonnenberg, J. L.; Williams; Ding, F.; Lipparini, F.; Egidi, F.; Goings, J.; Peng, B.; Petrone, A.; Henderson, T.; Ranasinghe, D.; Zakrzewski, V. G.; Gao, J.; Rega, N.; Zheng, G.; Liang, W.; Hada, M.; Ehara, M.; Toyota, K.; Fukuda, R.; Hasegawa, J.; Ishida, M.; Nakajima, T.; Honda, Y.; Kitao, O.; Nakai, H.; Vreven, T.; Throssell, K.; Montgomery Jr., J. A.; Peralta, J. E.; Ogliaro, F.; Bearpark, M. J.; Heyd, J. J.; Brothers, E. N.; Kudin, K. N.; Staroverov, V. N.; Keith, T. A.; Kobayashi, R.; Normand, J.; Raghavachari, K.; Rendell, A. P.; Burant, J. C.; Iyengar, S. S.; Tomasi, J.; Cossi, M.; Millam, J. M.; Klene, M.; Adamo, C.; Cammi, R.; Ochterski, J. W.; Martin, R. L.; Morokuma, K.; Farkas, O.; Foresman, J. B.; Fox, D. J.: Gaussian 16 Rev. C.01. Wallingford, CT, 2016.

(19) Pierens, G. K. 1H and 13C NMR scaling factors for the calculation of chemical shifts in commonly used solvents using density functional theory. *Journal of computational chemistry* **2014**, *35*, 1388-1394.

(20) Levitt, M. H.: *Spin Dynamics: Basics of Nuclear Magnetic Resonance*; 2nd ed.; John Wiley & Sons: Chichester, England ; Hoboken, NJ, 2008.

(21) Fyfe, C. A.: *Solid State NMR for Chemists*; C.F.C. Press, 1983.

(22) Mathematica, Version 12.2. https://www.wolfram.com/mathematica.

(23) Jeffrey, G. A.: *An Introduction to Hydrogen Bonding*; Oxford University Press, 1997.

(24) Ernst, M.; Meier, M.; Tuherm, T.; Samoson, A.; Meier, B. Low-Power High-Resolution Solid-State NMR of Peptides and Proteins. *Journal of the American Chemical Society* **2004**, *126*, 4764-4765.

Chapter 5 – Using Statistics to Determine Binding Constants from UV Data and Burstiness in Non-Uniformly Sampled NMR Data

5.1 Fitting of UV Data of a Self-Assembled Cage Host

5.1.1 Introduction

A large (Fe-Fe distance of 20.3 Å) self-assembled Fe_4L_6 iminopyridine cage has been demonstrated as a host for neutral molecules in organic solution and as a catalyst for polar reactions on the host interior. Oxidative dimerization of alkanethiol nucleophiles was also shown to be a side reaction not seen in smaller cages, requiring further study.[1,2] To investigate this side reaction, different *n*-alkanethiols can be reacted with the cage and their binding properties can be analyzed by UV-Vis absorbance spectroscopy.

5.1.2 Experimental Methods

Each alkanethiol was titrated into a 3 μM solution of the large Fe_4L_6 cage in CH_3CN. The changes in absorbance at 330 nm and 370 nm were recorded. Binding constants for 1:1 and 1:2 host-guest complex models were extracted by the method highlighted by Thordarson and explained below.[3,4] The UV-Vis absorbances at 330 nm and 370 nm were plotted against the concentration of the alkanethiol and the resulting curves were fit using a non-linear least-squares method in Mathematica.[5] This enabled us to find the binding constant (K_a) and molar absorptivities for the host (H) and host-guest (HG) complex for the 1:1 equilibrium model.

Since 1:1 host-guest binding can be written as

$$H + G \quad \overset{K_a}{\rightleftharpoons} \quad HG \qquad \text{(Equation 5.1)}$$

where the binding constant is

$$K_a = \frac{[HG]}{[H][G]} \qquad \text{(Equation 5.2)}$$

the concentrations of host, guest and host-guest complex can be related back to initial concentrations by

$$[H] = \frac{1}{2}\left(H_0 - G_0 - \frac{1}{K_a} \right) + \frac{1}{2}\sqrt{\left(G_0 - H_0 - \frac{1}{K_a} \right)^2 + 4\frac{G_0}{K_a}} \qquad \text{(Equation 5.3)}$$

$$[G] = \frac{1}{2}\left(G_0 - H_0 - \frac{1}{K_a} \right) + \frac{1}{2}\sqrt{\left(G_0 - H_0 - \frac{1}{K_a} \right)^2 + 4\frac{G_0}{K_a}} \qquad \text{(Equation 5.4)}$$

$$[HG] = \frac{1}{2}\left(G_0 + H_0 + \frac{1}{K_a} \right) - \frac{1}{2}\sqrt{\left(G_0 - H_0 - \frac{1}{K_a} \right)^2 + 4\frac{G_0}{K_a}} \qquad \text{(Equation 5.5)}$$

and the absorbance at a wavelength of λ can be described as

$$A^{\lambda} = \varepsilon_H^{\lambda}[H] + \varepsilon_{HG}^{\lambda}[HG] \qquad \text{(Equation 5.6)}$$

allowing us to fit the experimental absorption data at 330 nm and 370 nm as a function of the concentration of guest, G_o, in order to determine K_a, $\varepsilon_H^{330}, \varepsilon_{HG}^{330}, \varepsilon_H^{370}$, and ε_{HG}^{370}.

For the 1:2 equilibrium model, we determined the first (K_1) and second (K_2) binding constants and molar absorptivities for the host (H), host-guest (HG), and host-dual-guest (HG_2) complexes. Error for each of the fit parameters were recorded as ± standard error.

1:2 host-guest binding can be written as a two-step process

$$H + G \underset{}{\overset{K_1}{\rightleftharpoons}} HG \qquad \text{(Equation 5.7)}$$

$$HG + G \underset{}{\overset{K_2}{\rightleftharpoons}} HG_2 \qquad \text{(Equation 5.8)}$$

with the two binding constants

$$K_1 = \frac{[HG]}{[H][G]} \qquad \text{(Equation 5.9)}$$

$$K_2 = \frac{[HG_2]}{[HG][G]} \qquad \text{(Equation 5.10)}$$

Assuming $[G] \approx G_0$,

$$[H] = \frac{H_0}{1 + K_1 G_0 + K_1 K_2 G_0^2} \qquad \text{(Equation 5.11)}$$

$$[HG] = \frac{K_1 H_0 G_0}{1 + K_1 G_0 + K_1 K_2 G_0^2} \qquad \text{(Equation 5.12)}$$

$$[HG_2] = \frac{K_1 K_2 H_0 G_0^2}{1 + K_1 G_0 + K_1 K_2 G_0^2} \qquad \text{(Equation 5.13)}$$

Then the absorbance at a wavelength λ can be described as

$$A^{\lambda} = \varepsilon_{H}^{\lambda}\left[H\right] + \varepsilon_{HG}^{\lambda}\left[HG\right] + \varepsilon_{HG_2}^{\lambda}\left[HG_2\right] \qquad \text{(Equation 5.14)}$$

allowing us to fit the experimental absorption data at 330 nm and 370 nm as a function of the concentration of guest, G_o, in order to determine K_1,K_2, ε_{H}^{330}, ε_{HG}^{330}, $\varepsilon_{HG_2}^{330}$, ε_{H}^{370}, ε_{HG}^{370}, and $\varepsilon_{HG_2}^{370}$.

Residuals of each absorbance vs. concentation curve at both absorbances were generated from a 1:1 and a 1:2 model. The significance of the 1:2 model was based on the inverse ratio of the square of the residuals compared to the 1:1 model. If the error were normally distributed, this ratio would follow the F-distribution.[6] The 1:2 model must improve the residuals beyond the normal statistical fluctuations expected to be considered better. This is measured by the p-value, where a small value indicates that the residuals of the 1:2 model are actually smaller and not considered luck. p-values below 0.001 are considered significant. If the p-value produced by this statistical method is below 0.001, then the 1:2 model is considered the favored model.

5.1.3 Results and Discussion

A few examples will be provided and explained. The remaining data can be found in table 5.1. The first example is the smallest alkanethiol studied, pentane thiol (figures 5.1 and 5.2).

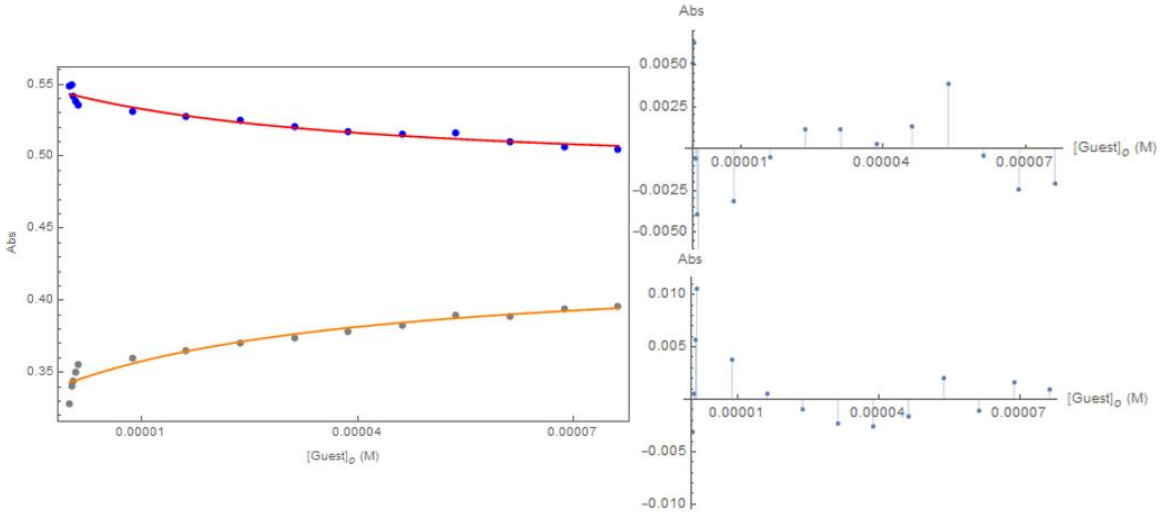

Figure 5.1: Fitting curves and plots of residuals when the UV binding data for pentane thiol with the large Fe_4L_6 cage is fit to the 1:1 binding model

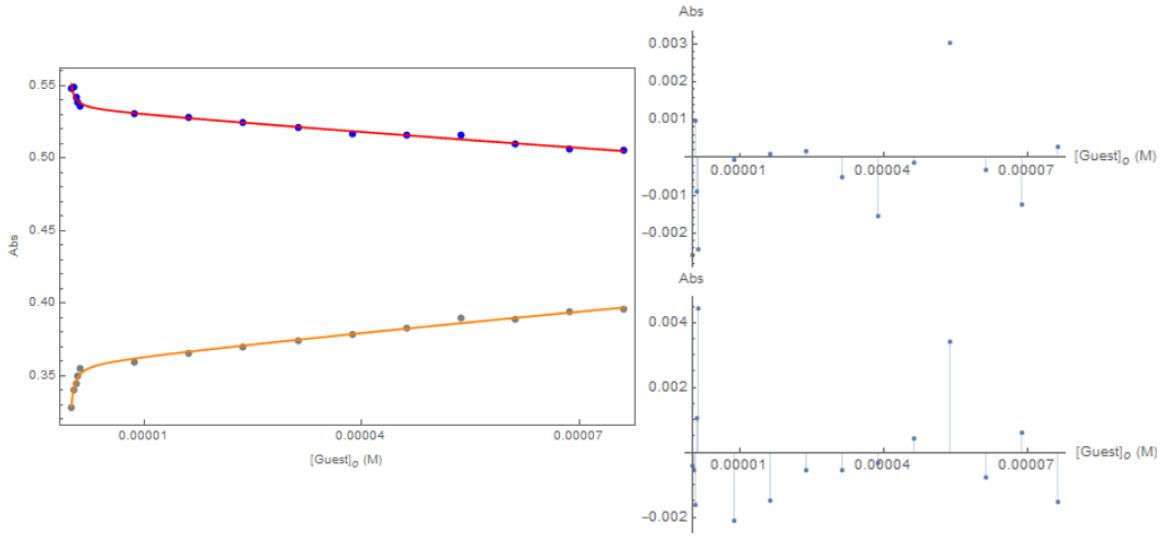

Figure 5.2: Fitting curves and plots of residuals when the UV binding data for pentane thiol with the large Fe_4L_6 cage is fit to the 1:2 binding model

The p-value of $2.07*10^{-4}$ is below 0.0001, meaning the 1:2 model is statistically favored. The fitting determined the binding constants are $K_1 = 2150 \pm 650$ ($*10^3$) M^{-1} and $K_2 = 1.2 \pm 3.0$ ($*10^3$) M^{-1}. The 1:2 model is also shown to be favored for hexane thiol and octane thiol (table 5.1).

The second example is a larger thiol, dodecane thiol.

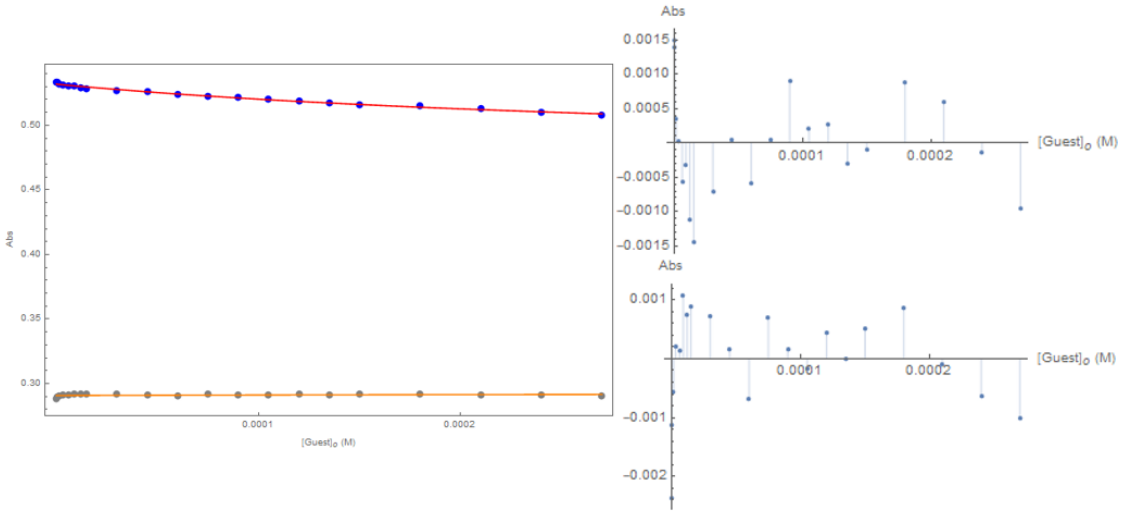

Figure 5.3: Fitting curves and plots of residuals when the UV binding data for dodecane thiol with the large Fe_4L_6 cage is fit to the 1:1 binding model

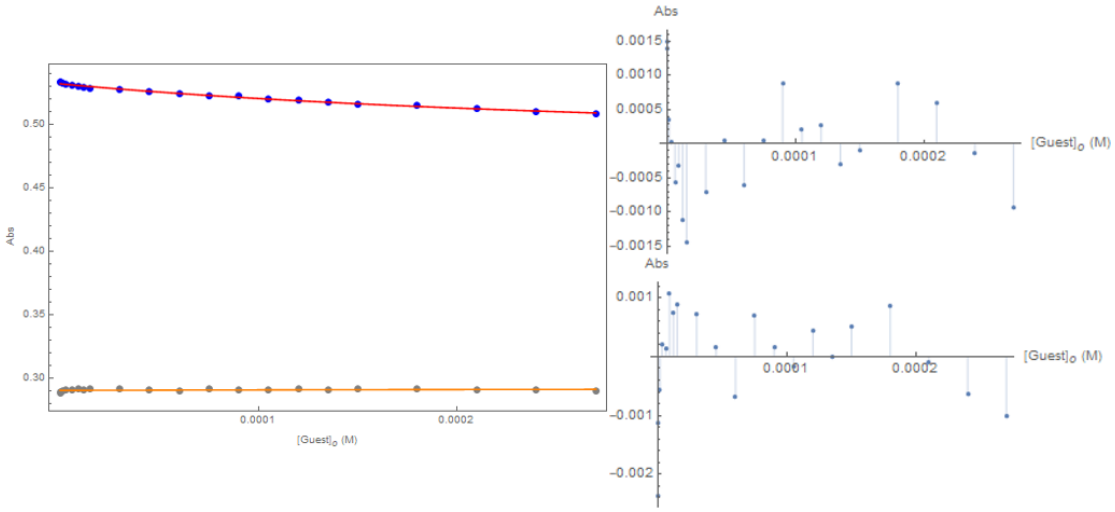

Figure 5.4: Fitting curves and plots of residuals when the UV binding data for dodecane thiol with the large Fe_4L_6 cage is fit to the 1:2 binding model

The p-value of 0.40 is above 0.0001, meaning the 1:1 model is statistically favored. The fitting determined the binding constant is $K_a = 2.74 \pm 0.60$ ($*10^3$) M^{-1}. The 1:1 model is also shown to be favored for decane thiol and undecane thiol.

Substrate	**K_a ($*10^3$ M^{-1})**	**K_1 ($*10^3$ M^{-1})**	**K_2 ($*10^3$ M^{-1})**	**A (4 K_2/K_1)**	**p-value**
Pentane Thiol		2150 ± 650	1.2 ± 3.0	$8.7*10^{-4}$	10^{-4}
Hexane Thiol		540 ± 130	2.4 ± 1.5	0.018	10^{-6}
Octane Thiol		174 ± 43	0.78 ± 0.53	0.018	10^{-7}
Decane Thiol	19.7 ± 6.4				0.02
Undecane Thiol	40 ± 19				0.004
Dodecane Thiol	2.74 ± 0.60				0.40
Propyl Disulfide	16.6 ± 2.4				0.019
Pentyl Disulfide	38.8 ± 7.1				0.43
Hexyl Disulfide	71 ± 14				0.46
Octyl Disulfide	76.1 ± 3.8				0.006
Decyl Disulfide	27.9 ± 9.4				0.01
Undecyl Disulfide	5.53 ± 0.48				0.19
Dodecyl Disulfide	8.39 ± 0.85				0.36

Table 5.1: Binding affinities for guest alkanethiols and product disulfides with the large Fe_4L_6 cage along with only the results from the favored model based on the p-value

Based on table 5.1, the smallest thiols studied fit best to the 1:2 model. As the thiols increase in size, the 1:1 binding model becomes more favored. The product disulfides also only fit to a 1:1 as they would make for larger substrates.

Hexane thiol guest was also looked at with a smaller caged host, an Fe_4L_6 with an Fe-Fe distance of only 17.3 Å. The binding for the small alkanethiol and the smaller cage favored the 1:1 model.

5.1.4 Conclusions and Future Work

The large self-assembled Fe_4L_6 iminopryidine cage with an Fe-Fe distance of 20.3 Å has been shown to discriminate between alkanethiol substrates based on size in the oxidative dimerization reaction it catalyzes. The cage favors either a two-step binding for smaller alkanethiols, or a one-step binding for larger alkanethiols. This was demonstrated by predicting binding affinities for differently sized alkanethiols with the cage using UV-Vis absorbance spectroscopy. This size selective property is unusual and requires further study to indicate potential applications.

5.2 Non-Uniform Sampling of NMR Data: Tracking Burst Sampling vs Repeating Timepoints by Fitting Data

5.2.1 Introduction

An emerging technique in the field of NMR is non-uniform sampling (NUS), a method used to increase the sensitivity of an NMR experiment. As mentioned in Chapter 1, NMR signal is digitized as the Free Induction Decay (FID) in the time domain, before being Fourier Transformed (FT) into the frequency domain. However, not every point of the FID is necessarily equally important for the signal of an NMR spectrum. A variety of different NUS methods have been developed that allow us to get greater sensitivity with a smaller number of points than traditional uniformly sampled data.[7-10] Current spectral reconstruction techniques may not able to properly reproduce the signal and noise level in the frequency domain, making it difficult to accurately measure the signal-to-noise ratio (SNR) of post-FT processed NUS data.[11,12] A method to measure the quality of time-domain NMR data in terms of spectral knowledge has been developed in our group which allows us to compare different NUS processing methods against each other.[13-15]

The Nyquist theorem is used to ensure that an FID has enough points to produce an accurate representation of a signal. The Nyquist Theorem states that the sample should be sampled at a rate twice the highest frequency. If a high frequency FID is undersampled, the spectrum in the frequency domain will feature the signal at a lower frequency than what

is measured in the FID. These inaccurate signals are called aliases and result in a decrease in the spectral knowledge we could obtain from a signal.[16]

Explored in this chapter is a NUS method called burst sampling, first described for use in NMR data processing by Hoch.[17] Hoch and Butts both found that bursty sampling schemes helped to minimize aliasing artifacts caused by under sampling that can result from NUS.[17,18] An attempt will be made to quantify these bursts and relate the burstiness of points in a non-uniformly sampled FID to the spectral knowledge. In addition, the knowledge of burst sampling schemes can be compared to other NUS methods.

5.2.2 Experimental Methods

Monte Carlo simulations are used to calculate spectral knowledge as previously described.[15] Briefly, using Mathematica[5], a model FID signal is generated as a decaying exponential where frequency of the signal, amplitude, length of data acquisition, and dwell time can be set. The model signal is then combined with a set noise level to mimic real NMR signal. Best estimates of the spectral parameters position, area, and linewidth are obtained through nonlinear least-squares fitting of the raw data. Monte Carlo simulations[19] are done to determine standard error used in the calculation of spectral knowledge and the coefficient of variation (Equation 5.15):

$$k = \frac{1}{c_v} = \frac{\langle \mu \rangle}{\sigma(\mu)} \qquad \text{(Equation 5.15)}$$

where *k* is spectral knowledge and c_v is the coefficient of variation, defined as the standard error, σ(μ), of the parameter relative to its expectation value <μ>. Standard error can also be determined using the Cramer-Rao lower bounds (CRLB).[19]

The burstiness calculation of an FID was done as described by Mobli.[20] Explained on a grid of 5 points, the maximum density is measured for a timepoint within the mask (where a mask of 3 is the recommended value). In the example presented in figure 5.5, the point at timepoint 1 has a maximum density of 2. Timepoint 2 has a maximum density of 2 as well. Timepoint 5 has a maximum density with of 1. The maximum densities of each timepoint are added together and put over the total number of measurements (size of the mask times the number of points) so the burstiness of this example is 5/9 or 0.556.

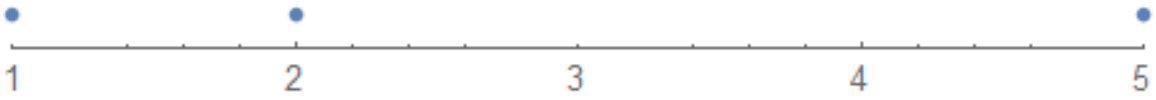

Figure 5.5: Sample of timepoints on a 5 point grid with a burstiness of 5/9.

This can be expanded to larger grids and more timepoints as expressed by equation 5.16:

$$B_M = \sum_{j=1}^{J} \frac{B_{\gamma_1 \cdot \gamma_2 \cdot \ldots \gamma L}}{J} = \overline{B_M(J)} \qquad \text{(Equation 5.16)}$$

where M is the size of the mask, J is the number of measurements, and L is the dimensionality of the sampling schedule.

An attempt will be made to calculate the difference in spectral knowledge between burst sampled data, scarce NUS data, and uniformly sampled data on a 256 point grid. The

burst sampled data will have 32 bursts of 8 timepoints while the scarce data will take 32 evenly spaced timepoints on the grid of 256 but repeat each timepoint 8 times. For all spectra, the frequency is set to 130 Hz, the first timepoint is at 0, and the final time point is at 3 times the T_2 relaxation time, where T_2 is the inverse of πw for w = 5 Hz. It was found that at this frequency, undersampled data can return a best estimate of the position parameter of -35 Hz. To show which method of sampling will most accurately estimate the correct position, fits can be given a starting guess of either 130 or -35 Hz.

For both the repeating timepoints and burst sampling data, 100,000 FIDs with the parameters described above and different generations of noise can be produced and each given a position guess of 130 Hz and -35 Hz. The residuals of each best fit are taken and the standard deviation of the set of residuals from the -35 Hz starting fit are subtracted from the standard deviation of the set of residuals from the 135 Hz starting fit. A negative difference of the standard deviation of the residuals means that starting the fit at -35 Hz has more error than starting the fit at 130 Hz for that sampling method. A difference close to 0 means that neither has greater error than the other. This workflow is shown in figure 5.6 for 32 timepoints repeated 8 times each and figure 5.7 for 32 bursts of 8 timepoints.

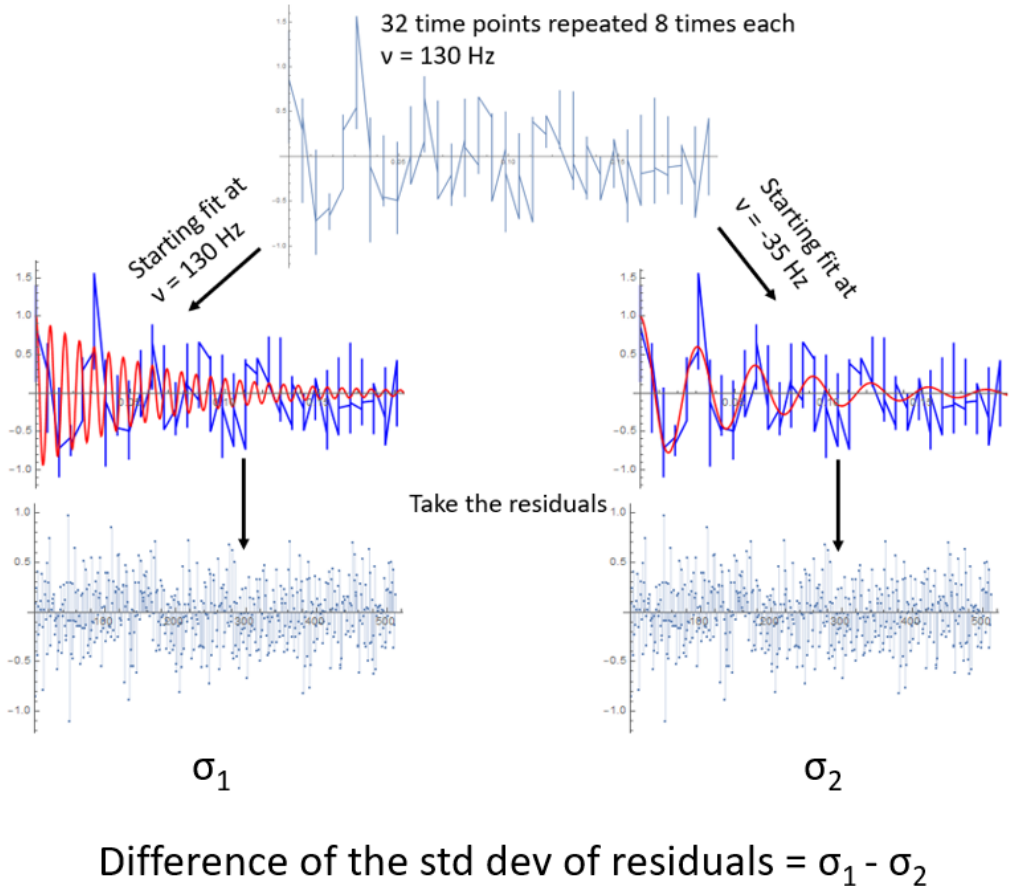

Figure 5.6: Workflow for finding the difference of the standard deviation of residuals for 32 timepoints repeated 8 times on a 256 point grid of a frequency of 130 Hz when the best estimate fits are started at 130 Hz and -35 Hz

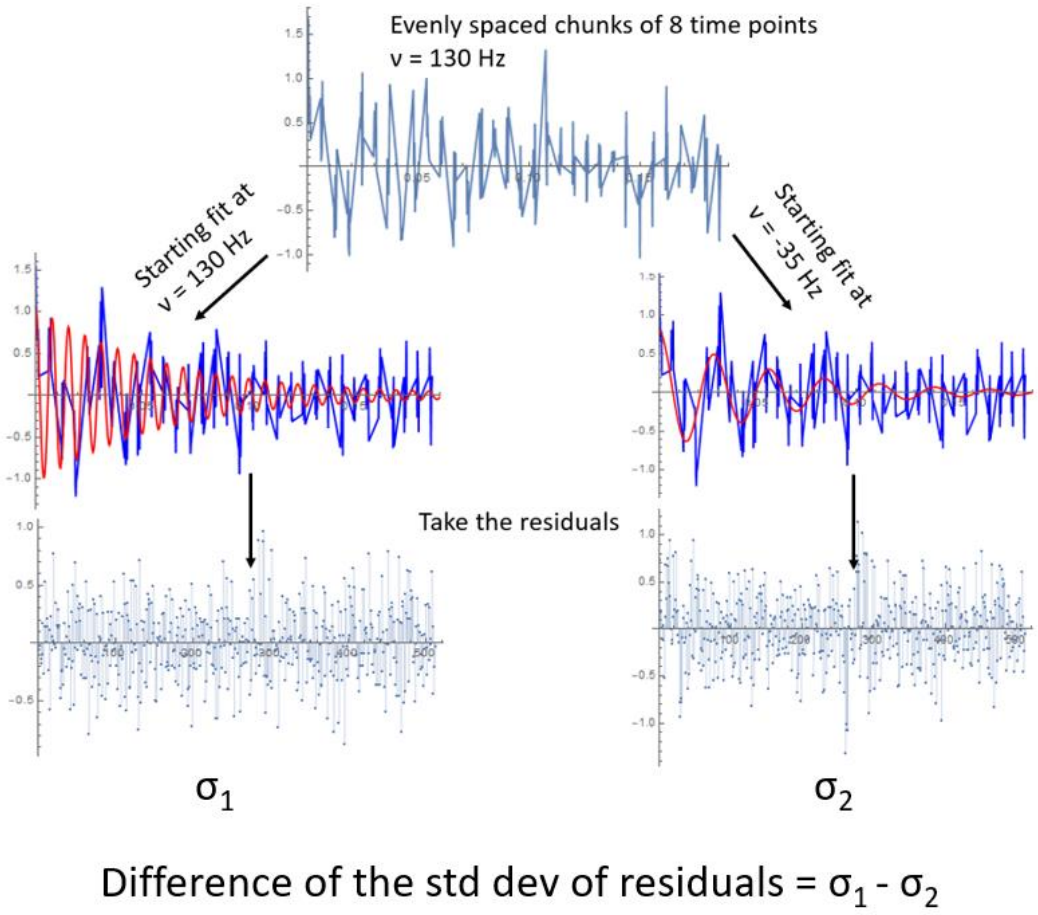

Figure 5.7: Workflow for finding the difference of the standard deviation of residuals for 32 bursts of 8 timepoints times on a 256 point grid of a frequency of 130 Hz when the best estimate fits are started at 130 Hz and -35 Hz

5.2.3 Results and Discussion

For 32 timepoints repeated 8 times each the difference of the standard deviation of the residuals are nearly evenly split between positive and negative, with 50,454 positive values and 49,424 negative values. This means that for an FID at a frequency of 130 Hz, the resulting peak position is equally likely to be the correct signal at 130 Hz as it is to be at -35 Hz, which would be an aliased peak, for this non-uniformly sampled scheme. Knowledge for the position, area, and width of the signal is presented in figure 5.8 normalized to a uniformly sampled spectrum. This shows that this non-uniformly sampled scheme results in a greater amount of knowledge compared to uniformly-sampled data, except for the position, which will result in low knowledge about half the time.

For evenly spaced bursts of 8 timepoints, the difference of the standard deviation of the residuals results in 90,791 negative values and 9,209 positive values. This means that for an FID at a frequency of 130 Hz, the resulting peak position is much more likely to be the correct signal at 130 Hz. While this sampling scheme could still result in an aliased peak, it would be much smaller than in the repeated time points sampling scheme. The knowledge of position, area, and width in figure 5.9 again show the benefits of this NUS scheme and, unlike the repeating timepoints data, we should be able to distinguish between the actual frequency and the undersampled frequency in a spectrum in the frequency domain.

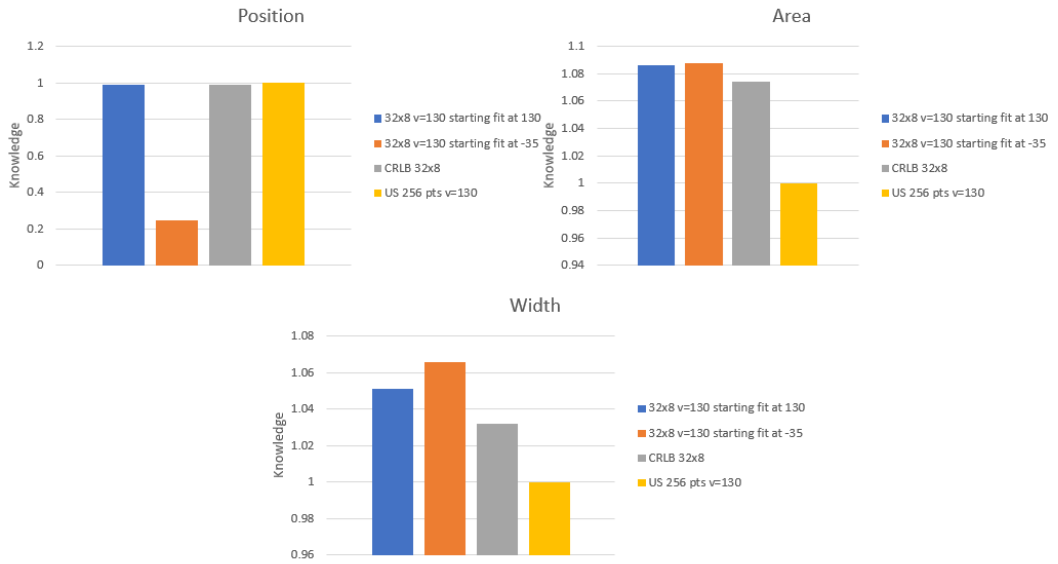

Figure 5.8: The knowledge of position, area, and width of a spectrum for 32 timepoints repeated 8 times each normalized against US data and the knowledge determined by CRLB.

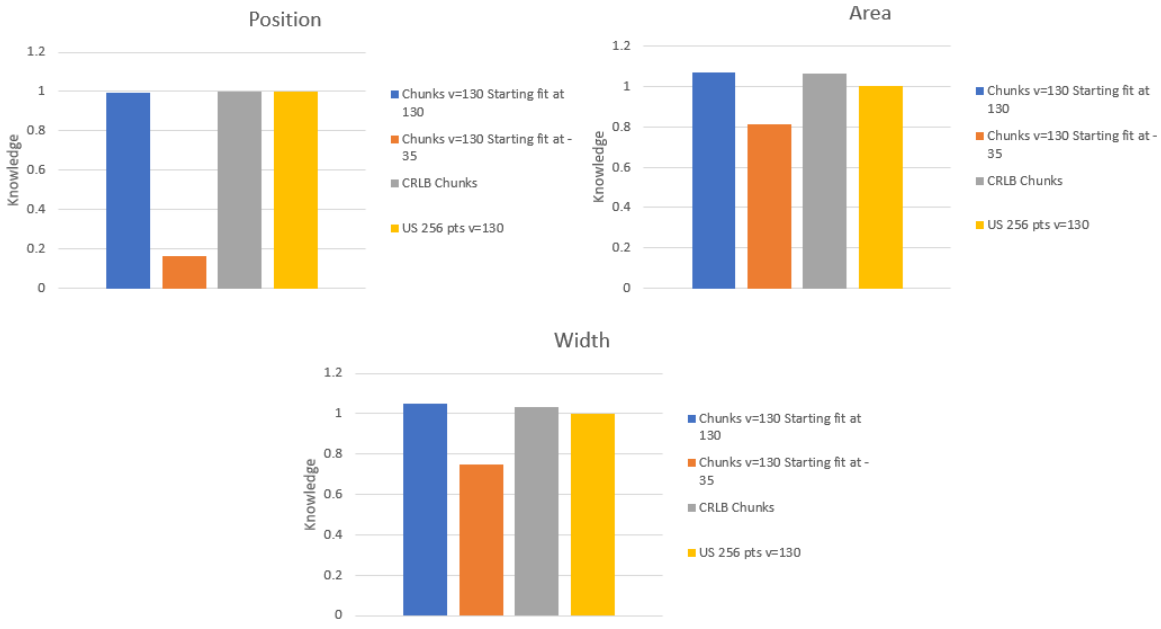

Figure 5.9: The knowledge of position, area, and width of a spectrum for 32 bursts of 8 timepoints times each normalized against US data and the knowledge determined by CRLB.

The burstiness of 8 bursts of 32 timepoints was calculated using the method described above developed by Mobli.[20] This very bursty sampling scheme has a B_3 (burstiness with a mask of 3) of 1, the maximum burstiness a sample can have. The more sparce sampling scheme was found to have a B_3 of 0.33333. These two set the limit for what we are expecting when we apply this method for different sampling schemes. The Mathematica code has been shown to effectively calculate B_3 for up to a 1024 point grid.

5.2.4 Conclusions and Future Work

We showed that sampling schemes that have bursty qualities decrease the size of an aliased peak in non-uniformly sampled data. This knowledge combined with burstiness quantification methods can be used to determine what the optimal amount of burstiness is in different NUS schemes to maximize knowledge. We can correlate burstiness with knowledge in a quantifiable way. Some NUS and non-uniform weighted sampling (NUWS) schemes that are currently being explored include burst sampling, as described above, triangular distribution, exponentially biased sampling, Poisson-gap sampling, and cosine and sinusoid weighted schemes. We will also attempt to look at multidimensional data, where knowledge and burstiness of the sampling data can be calculated in a similar way to 1-dimensional data.[7-9,15,17,20-24] Additionally, the data presented in this chapter has all been computationally generated in Mathmematica. Real NMR experiments with different sampling schemes must be performed to show their applications and to calculate and compare true SNR.

5.3 References

(1) Holloway, L. R.; Bogie, P. M.; Lyon, Y.; Ngai, C.; Miller, T. F.; Julian, R. R.; Hooley, R. J. Tandem Reactivity of a Self-Assembled Cage Catalyst with Endohedral Acid Groups. *Journal of the American Chemical Society* **2018**, *140*, 8078-8081.

(2) Ngai, C.; Bogie, P. M.; Holloway, L. R.; Dietz, P. C.; Mueller, L. J.; Hooley, R. J. Cofactor-Mediated Nucleophilic Substitution Catalyzed by a Self-Assembled Holoenzyme Mimic. *The Journal of Organic Chemistry* **2019**, *84*, 12000-12008.

(3) Thordarson, P. Determining association constants from titration experiments in supramolecular chemistry. *Chemical Society Reviews* **2011**, *40*, 1305-1323.

(4) Brynn Hibbert, D.; Thordarson, P. The death of the Job plot, transparency, open science and online tools, uncertainty estimation methods and other developments in supramolecular chemistry data analysis. *Chemical Communications* **2016**, *52*, 12792-12805.

(5) Mathematica, Version 12.2. https://www.wolfram.com/mathematica.

(6) Garland, C. W.; Nibler, J. W.; Shoemaker, D. P.: *Experiments in physical chemistry*; McGraw-Hill Higher Education: Boston, 2009.

(7) Barna, J. C. J.; Laue, E. D.; Mayger, M. R.; Skilling, J.; Worrall, S. J. P. Exponential sampling, an alternative method for sampling in two-dimensional NMR experiments. *Journal of Magnetic Resonance (1969)* **1987**, *73*, 69-77.

(8) Kumar, A.; Brown, S. C.; Donlan, M. E.; Meier, B. U.; Jeffs, P. W. Optimization of two-dimensional NMR by matched accumulation. *Journal of Magnetic Resonance (1969)* **1991**, *95*, 1-9.

(9) Mobli, M.; Hoch, J. C. Nonuniform sampling and non-Fourier signal processing methods in multidimensional NMR. *Progress in Nuclear Magnetic Resonance Spectroscopy* **2014**, *83*, 21-41.

(10) Hoch, J. C.; Maciejewski, M. W.; Mobli, M.; Schuyler, A. D.; Stern, A. S. Nonuniform Sampling and Maximum Entropy Reconstruction in Multidimensional NMR. *Accounts of Chemical Research* **2014**, *47*, 708-717.

(11) Yoon, J. W.; Godsill, S.; Kupče, E.; Freeman, R. Deterministic and statistical methods for reconstructing multidimensional NMR spectra. *Magnetic Resonance in Chemistry* **2006**, *44*, 197-209.

(12) Suiter, C. L.; Paramasivam, S.; Hou, G.; Sun, S.; Rice, D.; Hoch, J. C.; Rovnyak, D.; Polenova, T. Sensitivity gains, linearity, and spectral reproducibility in nonuniformly sampled multidimensional MAS NMR spectra of high dynamic range. *Journal of Biomolecular NMR* **2014**, *59*, 57-73.

(13) Marshall, A. G.; Verdun, F. R.: CHAPTER 10 - Epilog: Fourier transforms in other types of spectroscopy. In *Fourier Transforms in NMR, Optical, and Mass Spectrometry*; Marshall, A. G., Verdun, F. R., Eds.; Elsevier: Amsterdam, 1990; pp 369-371.

(14) Palmer, M. R.; Suiter, C. L.; Henry, G. E.; Rovnyak, J.; Hoch, J. C.; Polenova, T.; Rovnyak, D. Sensitivity of Nonuniform Sampling NMR. *The Journal of Physical Chemistry B* **2015**, *119*, 6502-6515.

(15) Kaur, M.; Lewis, C. M.; Chronister, A.; Phun, G. S.; Mueller, L. J. Non-Uniform Sampling in NMR Spectroscopy and the Preservation of Spectral Knowledge in the Time and Frequency Domains. *The Journal of Physical Chemistry A* **2020**, *124*, 5474-5486.

(16) Brigham, E. O.: *The fast Fourier transform and its applications*; Prentice-Hall, Inc., 1988.

(17) Maciejewski, M. W.; Qui, H. Z.; Rujan, I.; Mobli, M.; Hoch, J. C. Nonuniform sampling and spectral aliasing. *Journal of magnetic resonance (San Diego, Calif. : 1997)* **2009**, *199*, 88-93.

(18) Ndukwe, I. E.; Shchukina, A.; Kazimierczuk, K.; Cobas, C.; Butts, C. P. EXtended ACquisition Time (EXACT) NMR—A Case for ′Burst′ Non-Uniform Sampling. *ChemPhysChem* **2016**, *17*, 2799-2803.

(19) Press, W. H.; William, H.; Teukolsky, S. A.; Saul, A.; Vetterling, W. T.; Flannery, B. P.: *Numerical recipes 3rd edition: The art of scientific computing*; Cambridge university press, 2007.

(20) Mobli, M.; Miljenović, T. M. Framework for and evaluation of bursts in random sampling of multidimensional NMR experiments. *Journal of Magnetic Resonance* **2019**, *300*, 103-113.

(21) Hyberts, S. G.; Takeuchi, K.; Wagner, G. Poisson-Gap Sampling and Forward Maximum Entropy Reconstruction for Enhancing the Resolution and Sensitivity of Protein NMR Data. *Journal of the American Chemical Society* **2010**, *132*, 2145-2147.

(22) Kazimierczuk, K.; Zawadzka, A.; Koźmiński, W. Optimization of random time domain sampling in multidimensional NMR. *Journal of Magnetic Resonance* **2008**, *192*, 123-130.

(23) Delaglio, F.; Walker, G. S.; Farley, K. A.; Sharma, R.; Hoch, J. C.; Arbogast, L. W.; Brinson, R. G.; Marino, J. P. Non-uniform sampling for all: more NMR spectral quality, less measurement time. *American pharmaceutical review* **2017**, *20*.

(24) Maciejewski, M. W.; Schuyler, A. D.; Hoch, J. C.: Practical Nonuniform Sampling and Non-Fourier Spectral Reconstruction for Multidimensional NMR. In *Protein NMR: Methods and Protocols*; Ghose, R., Ed.; Springer New York: New York, NY, 2018; pp 341-352.